Doctoral Thesis (博士論文)

Synthesis, Tuning, and Photovoltaic Applications of

Plasmonic Compound Nanomaterials

(プラズモン共鳴化合物ナノ材料の合成と制御および光

電変換への応用)

Seung Hyuk Lee (李 昇爀)

Table of contents

Chapter 1

Introduction

1.1 Outline of this work

Extensive research effort on the interplay between light and matter has been conducted over the decades. One of them, plasmons are light trapping mechanisms by free electron oscillation in nanoscale materials. To use those localized surface plasmon resonance (LSPR) in various applications, a variety of metal nanoparticles (NPs) were synthesized and applied. In 2005, It was proved that the energy trapped by LSPR can be converted into a carrier flow at the interface between plasmonic Au NPs and a TiO_2 thin film.[1] This phenomenon, plasmon-induced charge separation (PICS), has opened up new application fields.[2]

The most of LSPR and PICS related studies were conducted by using noble metal NPs such as Au,[1,3-6] Ag,[3,6-8] and Cu[6,9] in the visible wavelength region. This is due to well-established methods of NP synthesis,[10] high stability of the NPs themselves, and the absorption of visible light, which has a relatively high energy.[11] On the other hand, even though the compound NPs have a much wider range of candidate materials and their combinations, only a few plasmonic compound NPs such as WO_{3-x},[12,13] MoO_{3-x},[14-17] MoO_2,[18] CuS,[19] ITO^{20}, and TiN[21] have been known to show LSPR, mostly in the near infrared (NIR) region. Furthermore, in the case of PICS, no report has been published for plasmonic compound NPs, likely due to their low energy of LSPR.

In this work, plasmonic MoO_x NPs were synthesized with controlled oxygen vacancy and MoO_{3-x} nanostructures were developed using an ensemble of small NPs as a template. Plasmonic characteristics of those NPs and nanostructures were also investigated. In addition, plasmonic ITO NPs were synthesized with controlled doping ratio and distribution in single NPs and their optical properties and electrical properties were investigated. Using those synthesized nanomaterials, solid-state photovoltaic cells were developed for achieving PICS with plasmonic compound nanomaterials. Their photoelectrical responses were studied, and mechanisms of PICS were discussed.

In this chapter, basics and applications of LSPR for metal NPs are briefly explained. Then, LSPR characteristics of compound NPs and their synthesis methods are summarized.

Next, principle and mechanisms of PICS with metal NPs are introduced. Finally, the objective of this study is described briefly.

1.2 Localized surface plasmon resonance (LSPR)[22-24]

Small NPs and nanostructures can interact with incident light by collective oscillations of their free electrons, resulting in light absorption and scattering. This phenomenon is called localized surface plasmon resonance (LSPR) (Figure 1.1). Their LSPR characteristics are directly connected to the properties of the NPs and nanostructures such as free carrier density and mobility, size, shape, and so on. The dipole polarizability in the NPs is given by

$$\alpha = 3\varepsilon_0 V \frac{(\varepsilon - \varepsilon_m)}{(\varepsilon + 2\varepsilon_m)} \tag{1.1}$$

where ε_0 is free space permittivity, V is the volume of NPs, ε is a dielectric function of NPs and ε_m is a dielectric constant of the surrounding medium. The maximum polarizability is given when the denominator is the minimum.

$$\varepsilon_r = -2\varepsilon_m \tag{1.2}$$

where ε_r is the real part of ε. The resonance frequency of LSPR, ω_{LSPR}, is expressed by

$$\omega_{LSPR} = \sqrt{\frac{\omega_p^2}{1 + 2\varepsilon_m} - \gamma^2} \tag{1.3}$$

where ω_p is the bulk plasma frequency and γ is bulk collision frequency, by the Drude model

$$\varepsilon_r = 1 - \frac{\omega_p^2}{\omega^2 + \gamma^2} \tag{1.4}$$

$$\omega_p = \sqrt{\frac{Ne^2}{m\varepsilon_0}} \tag{1.5}$$

where N is the free charge carrier concentration, e is the elementary charge, m is the effective mass of carrier. According to Eq. 1.3, ω_{LSPR} and γ related to the LSPR energy and

linewidth of LSPR spectra.
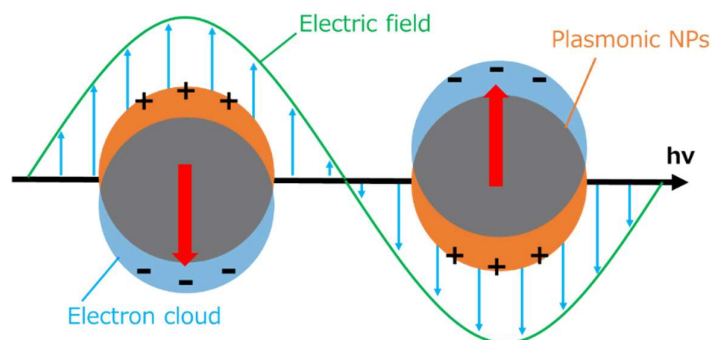
Figure 1.1 Illustration of localized surface plasmon resonance of plasmonic NPs.

1.3 LSPR of metal NPs

The most investigations of LSPR have been conducted by noble metal NPs such as Au, Ag, and Cu, since noble metal NPs are relatively stable under various conditions and have LSPR energy that is high enough to absorb visible light. In this section, characteristics of LSPR of noble metal NPs are described. As introduced in section 1.2, the LSPR energy is dependent on the concentration and the effective mass of free charge carrier (*i.e.*, carrier density and mobility, and thereby species and composition of NPs) and the dielectric constant of the surrounding medium. In the case of larger metal NPs, the LSPR characteristics are also dependent on the NP size and shape.

(a) Metal species

Difference in the carrier density and mobilities gives rise to different LSPR characteristics for NPs of different noble metal species.[25] As shown in Figure 1.2, the LSPR peak wavelength and the absorption intensity are totally different for each noble metal NP.
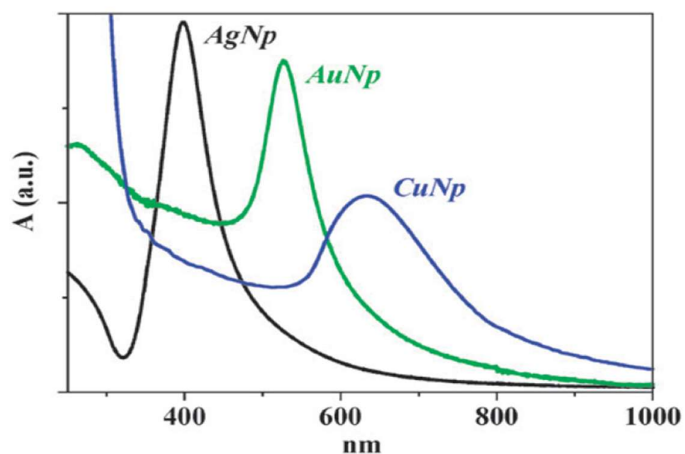
Figure 1.2 Absorbance spectra of 20-40 nm size and spherical shape of Ag, Au, and Cu NPs obtained by laser ablation synthesis in water. Reprinted with permission from ref. 25. Copyright the Owner Societies 2009.

(b) Dielectric environment

      The LSPR peak wavelength highly depends on the dielectric environment of plasmonic NPs.[26] Figure 1.3 shows examples of absorption spectra of Au NPs measured in various liquids with different refractive indices. As the refractive index increases, the LSPR peak wavelength of the Au NPs shifts to the longer wavelength (Figure 1.3b). The shift of the wavelength is dependent linearly on the refractive index increase in general. This is a unique characteristic of LSPR, which can be used for chemical sensing and for checking whether or not an unknown absorption peak is due to LSPR.
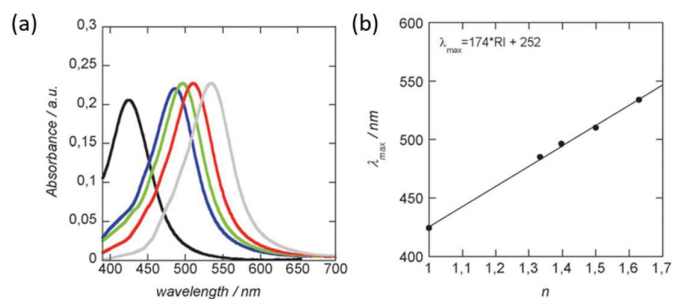
Figure 1.3 (a) Measured absorbance spectra of 12 nm silver nanoparticle monolayer immersed in liquid samples of various refractive indices and (b) Relationship between the refractive index of solvent and peak wavelength of absorbance. Reprinted with permission from ref. 26. Copyright the Royal Society of Chemistry 2012.

(c) Size of metal NPs

The size of metal NPs greatly affects the LSPR characteristics.[27] As NP size increases, the dipole polarization increases and the resonance frequency of the collective oscillation is lowered, namely the peak position is moved to a lower energy (longer wavelength) region. Extensive increase in the NP size (*e.g.*, >50 nm) can generate multipolar LSPR modes. This often increases the peak width (full width at half maximum, FWHM) (Figure 1.4).
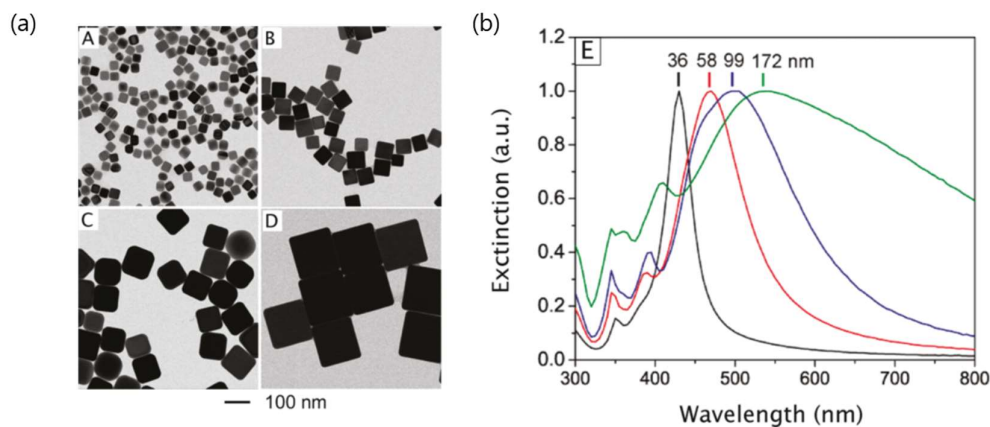
Figure 1.4 (a) TEM images and (b) LSPR spectra of Ag nanocubes with controlled-size (36, 58, 99, 172 nm of edge length). Reprinted with permission from ref. 27. Copyright 2010 American Chemical Society.

(d) Shape of metal NPs

The shape of plasmonic NPs also highly affects the LSPR characteristics. As the corner sharpness of Ag triangular nanoplates is decreased, the LSPR peak is clearly blue-shifted[28] (Figure 1.5a, c). This is because the sharp edge increases the dipole polarization and the resonance frequency of the collective oscillation is lowered. In the case of NPs grown mainly in one direction (*e.g.*, Au nanorods in Figure 1.5b), the LSPR mode is split into two modes (longitudinal and transversal modes, in the case of nanorods), and the LSPR peak in the longer wavelength region (longitudinal mode) is red-shifted almost proportionally to the aspect ratio[29] (Figure 1.5d).
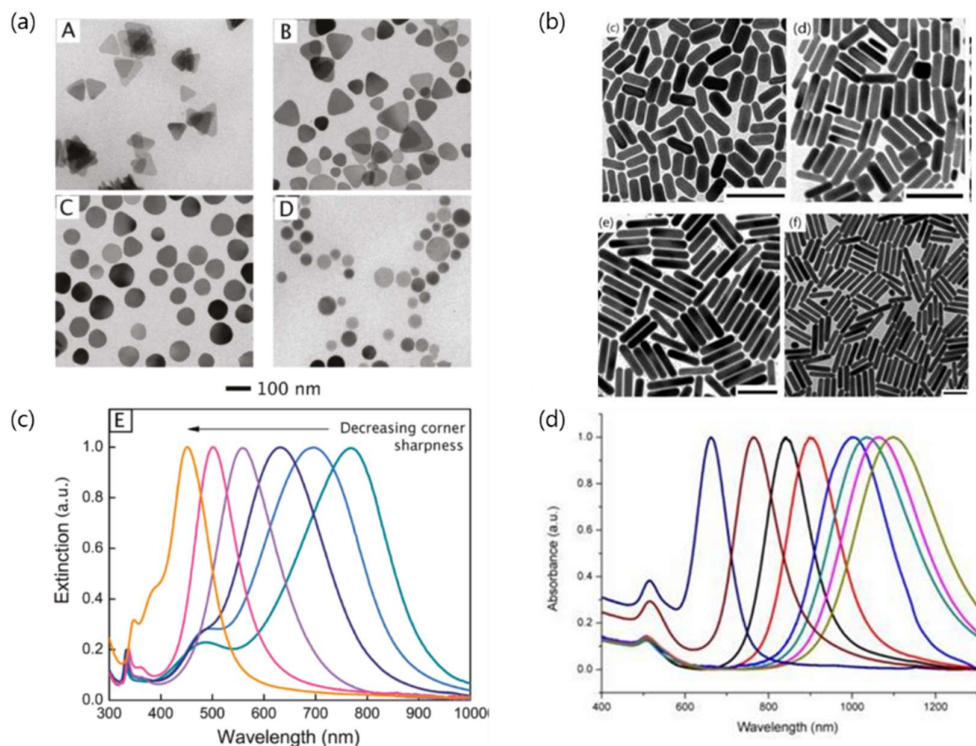
Figure 1.5 (a)(c) TEM images and extinction spectrum of Ag triangular nanoplates with decreasing corner sharpness. Reprinted with permission from ref. 28. Copyright 2010 Wiley-VCH Verlag GmbH & Co. KGaA, Weinheim. (b)(d) SEM images and extinction spectrum of Au nanorods with increasing aspect ratios. Reprinted with permission from ref. 29. Copyright the Royal Society of Chemistry 2017.

(e) Composition of alloy NPs

As discussed earlier in this section, NPs of different metal species exhibit different LSPR characteristics. Likewise, metal alloy NPs also show LSPR characteristics dependent on the metal composition[30] as Figure 1.6 shows.
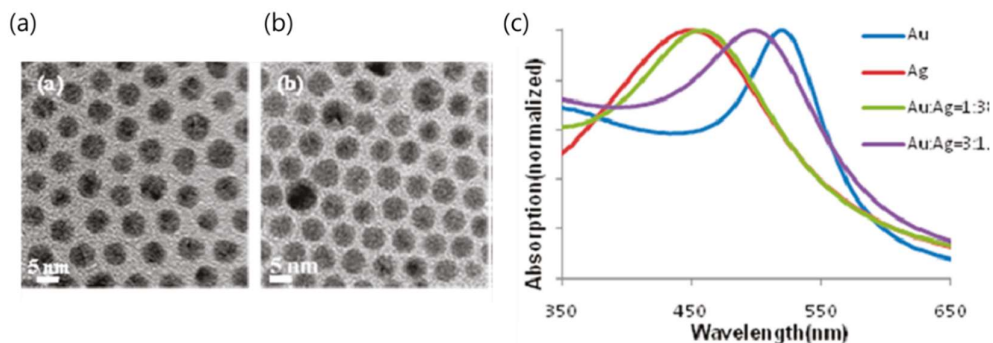
Figure 1.6 TEM images of Au-Ag alloy NPs with controlled size for (a) Au:Ag = 1:3 and (b) Au:Ag = 3:1 and (c) their absorption spectra together with those for Au and Ag NPs. Reprinted with permission from ref. 30. Copyright 2011 American Chemical Society.

1.4 LSPR of compound NPs

1.4.1 Overview of compound LSPR

It is known that compound nanomaterials which have a sufficient amount of free charge carriers can also have LSPR (Figure 1.7). In this section, notable differences in LSPR characteristics between compound NPs and noble metal NPs are explained. Especially, the origin of free charge carriers and unique characteristics of compound NPs are described. Finally, representative plasmonic compound NPs are introduced.
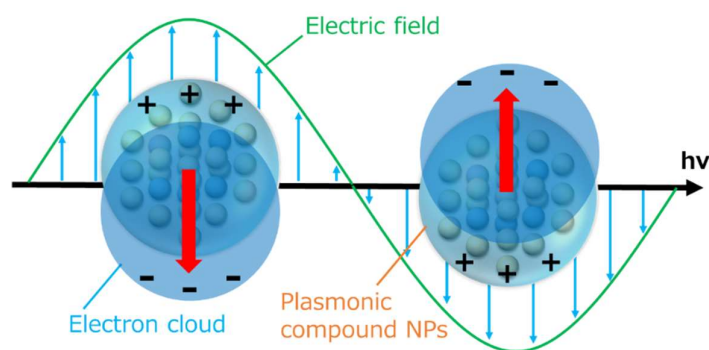
Figure 1.7 Illustration of LSPR of compound NPs.

Like noble metal NPs, compound NPs that have sufficient career density and mobility also exhibit LSPR[24] (Figure 1.8). However, unlike noble metal NPs, which show LSPR mainly in the visible region, most compound NPs exhibit LSPR in lower energy regions such as NIR and IR. This is chiefly because compound NPs have relatively low free charge carrier density in comparison with noble metal NPs.
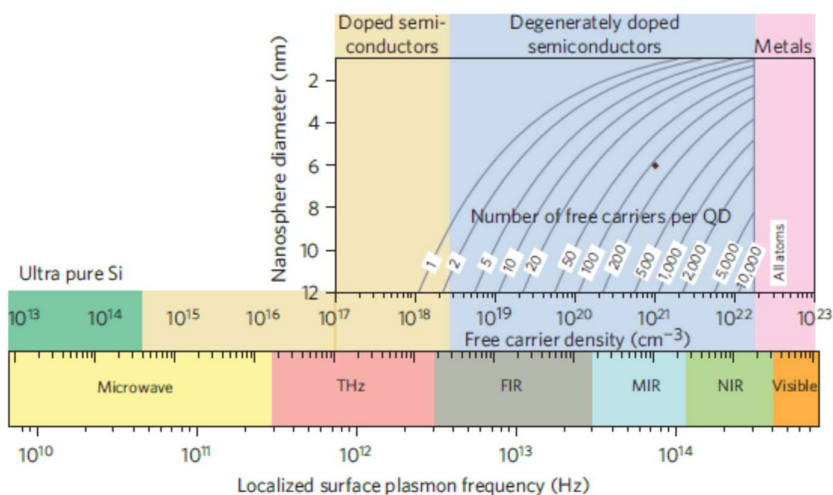
Figure 1.8 Dependence of the LSPR frequency of conducting and semiconducting nanoparticles on the free charge carrier density. Reprinted with permission from ref. 24. Copyright 2011 Macmillan Publishers Limited.

In the case of an n-type semiconducting compound, the charge carriers are electrons, and in the case of a p-type semiconducting compound, the charge carriers are holes (Figure 1.9). The carrier density of a compound could be controlled by changing chemical composition including doping[31] (dopant species and doping ratio) and defect formation,[31] as well as changing chemical structure including phase transformation.[32] Therefore, compound NPs usually have higher opportunity to be tuned in terms of LSPR properties.

Electronic property of compound NPs
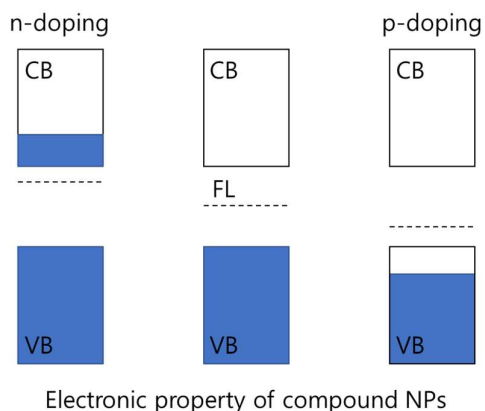
Figure 1.9 Schematic illustration of the band structures of n-type and p-type semiconducting compound materials. CB, VB, and FL are the conduction band, valence band, and Fermi level, respectively.

1.4.2 Origin of free charge carriers

As introduced in the above section, the nature of plasmonic compound NPs is strongly dependent on free charge carrier density in compound NPs. To activate LSPR in compound NPs, introducing dopant and/or vacancy is generally used (Figure 1.10a).
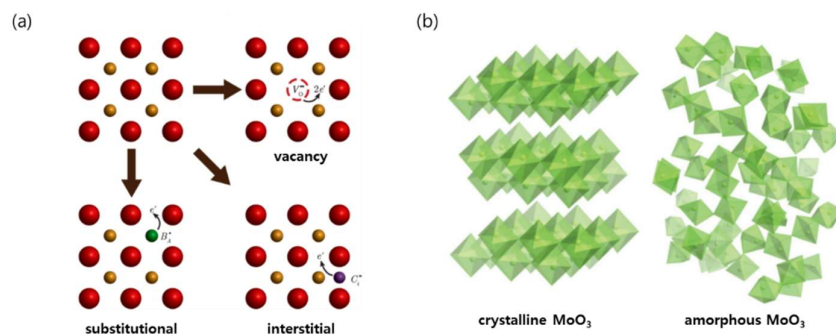
Figure 1.10 (a) Schematic illustration of doping mechanisms in compound NPs with vacancy, interstitial, and substitutional doping. Reprinted with permission from ref. 31. Copyright 2014 American Chemical Society. (b) Illustration of the crystalline and amorphous states of MoO_3. Reprinted with permission from ref. 32. Copyright 2014 American Chemical Society.

The doping methods can be classified into substitutional and interstitial doping (Figure 1.10a). Those methods give free electrons or holes by selection of dopant species. Also, those methods can be used at the same time. Although the doping is the most widely used to generate carriers because it is a very simple and reliable method, lattice strain by the dopant also occurs.[32] This lattice strain interferes with the motion of free charge carriers. Thus, there is an upper limit of doping ratio for each system.

Formation of vacancy also gives free charge carriers in compound NPs (Figure 1.10a). This is often achieved easily by oxidation or reduction of the material.[14] However, the vacancy is hard to stabilize usually, and the population of vacancy changes easily. In certain cases, the concentration of defects becomes so high that a defect band is formed in between the conduction and valence bands.[33]

In very rare cases, phase transformation could also activate LSPR in compound NPs.[34] Especially, it is observed in the amorphous phase of MoO_3 (Figure 1.10b). As a result of amorphous phase transformation, the twisted unit cell changes the binding distance of each element, and the electrons whose binding force is loosened become the source of free charge carriers.

1.4.3 Characteristics of compound LSPR

As introduced in section 1.3, the LSPR energy can be controlled by changing size, shape, and compositions of compound NPs as well as the dielectric constant of the surrounding medium. Conventional plasmonic compound NPs may be classified into four types; (a) metal oxides such as MoO_3 and WO_3, (b) doped metal oxides such as tin-doped indium oxide (or indium-tin oxide, ITO) and indium-doped cadmium oxide (ICO),[35] (c) metal chalcogenides except for oxides, such as CuS, and (d) metal nitrides such as TiN. As illustrated in Figure 1.11, LSPR of compound NPs are located mainly in the NIR and IR regions.
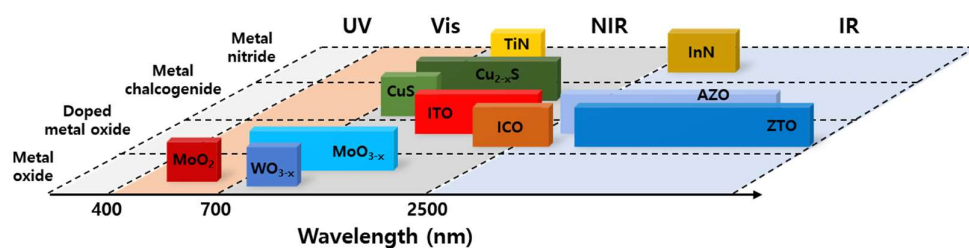
Figure 1.11 Schematic for LSPR locations of representative plasmonic compound NPs.

(a) Size and shape of NPs

The size and shape of compound NPs are expected to greatly affect the characteristics of the LSPR. However, except for the case of CuS series[34,36] in Figure 1.12, there are a few reports discussing the correlation between the shape or size of compound NPs and their optical properties. This might be because of difficulties in distinguishing single particles from aggregated ones for small compound NPs.
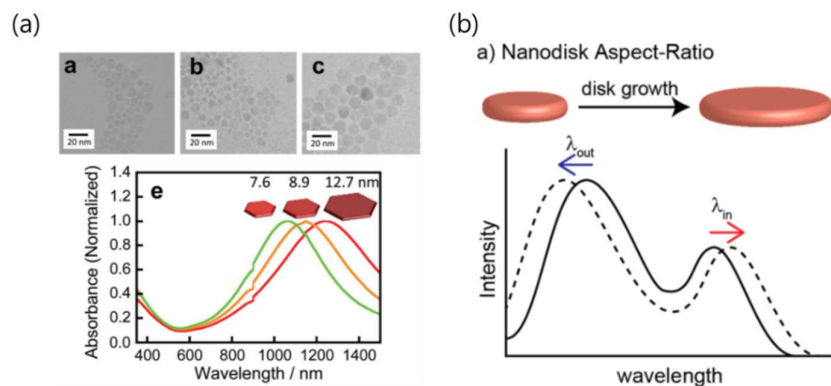
Figure 1.12 (a) TEM images and absorption spectra of CuS NPs with different size (average width 7.6, 8.9, and 12.7 nm). Reprinted with permission from ref. 34. Copyright the Royal Society of Chemistry 2015. (b) Illustration of how LSPR is expected to change with aspect ratio. Reprinted with permission from ref. 36. Copyright 2012 American Chemical Society.

(b) Doping ratio of NPs

The doping concertation is one of the main factors in changing LSPR characteristics of doped metal oxides.[20,35,37] As shown in Figure 1.13, the most compound NPs exhibit a blue shift of LSPR absorption and an increase in extinction coefficient as the doping concentration is increased. However, as described in the previous section, since the doping causes lattice strain, the optimum doping concentration should exist.[20] In the case of ITO, the optimum doping ratio is 10 mol% Sn, which gives the highest free electron density.
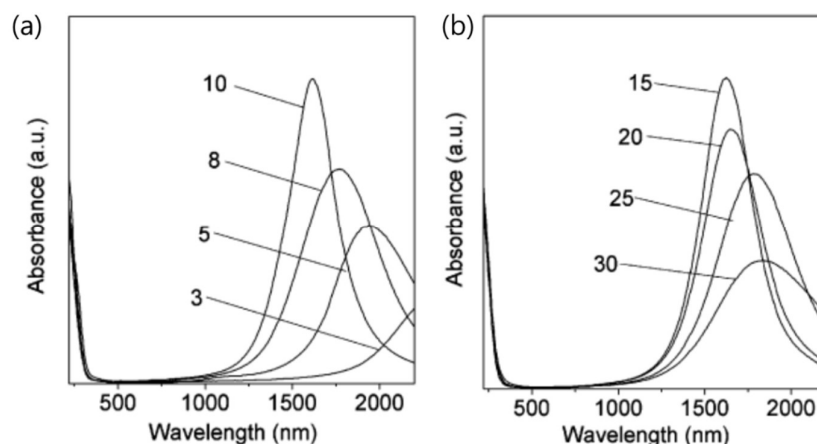
Figure 1.13 LSPR spectra of ITO NPs with different doping concentrations (3, 5, 8, 10, 15, 20, 25, and 30 mol% Sn). Reprinted with permission from ref. 20. Copyright 2009 American Chemical Society.

(c) Doping distribution in NPs

The dopant distribution inside the particle also affects the characteristics of LSPR.[31,38] Figure 1.14 shows that the shape of the LSPR spectra of ITO NPs is influenced by the dopant distributions, because the doping distribution affects the damping of the oscillation of the free charge carriers.[38] For this reason, the dopant distribution affects the width (or FWHM) of LSPR.
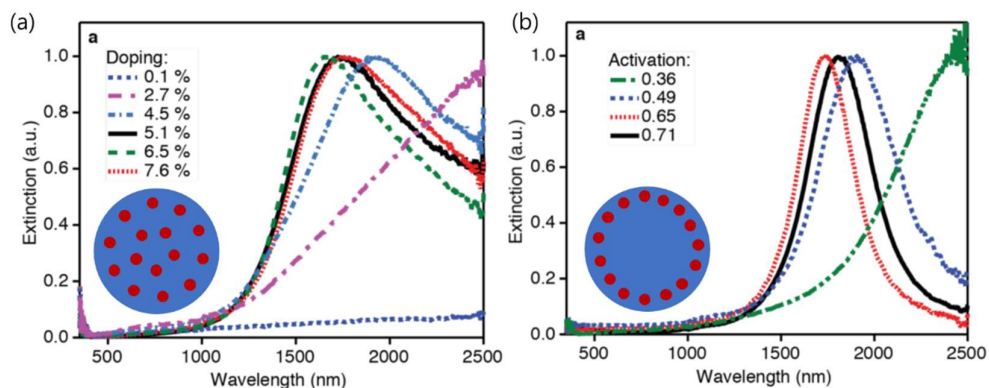
Figure 1.14 Extinction spectra of synthesized ITO NPs with different dopant distributions in NP. Dopant is concentrated in (a) the core region or (b) the surface region. Reprinted with permission from ref. 38. Copyright 2014 American Chemical Society.

(d) Vacancy concentration of NPs

The concentration of oxygen vacancy also affects the free charge carrier density. During the synthesis of MoO_{3-x} NPs, a blue-shift of an LSPR peak is observed, when a strong reducing agent is used (Figure 1.15).[14,39] This blue-shift is explained in terms of an increasing number of oxygen vacancy in the MoO_{3-x} NPs.
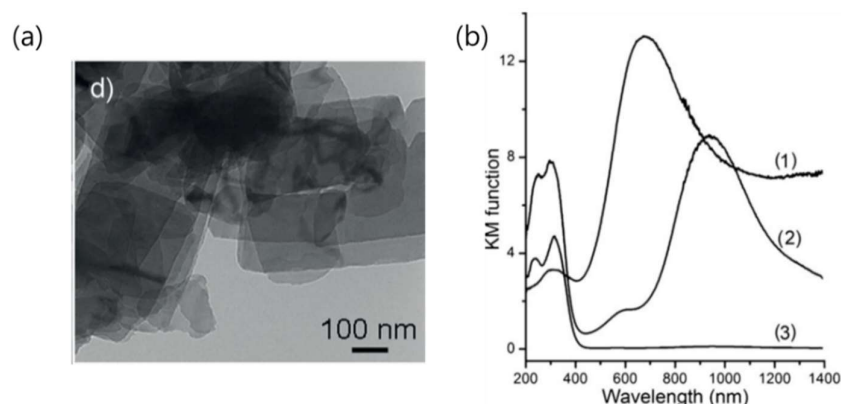
Figure 1.15 TEM image of MoO_{3-x} nanosheets and their optical properties with different reduction rate. Reprinted with permission from ref. 14. Copyright 2014 Wiley-VCH Verlag GmbH & Co. KGaA, Weinheim.

1.5 Synthesis of plasmonic compound NPs

Compound NPs are usually synthesized as colloids suspended in a liquid phase, and such a method is called colloidal synthesis.[40] The colloidal synthesis includes some different or closely related methods like hot injection method,[41] aminolysis method,[20] and pyrolysis method.[42] This method has the following advantages: (1) It gives very small compound NPs (~10 nm scale), which can be dispersed in a solution; (2) It allows control of the composition or the doping ratio on the basis of combinations of precursors; (3) It gives various types of NPs through control of reaction conditions including temperature; (4) It allows scale-up easily for mass-production and economic competitiveness. On the other hand, fine control of the NP size has been difficult.

1.5.1 Growth process of NPs

As shown in Figure 1.16,[40] the general colloidal synthesis process for metal oxide NPs can be divided into three stages: (1) monomer generation, (2) nucleation, and (3) growth. In stage 1, metal precursors such as metal carboxylate in solution start to transform to -M-OH form, for instance by pyrolysis. As can be seen from the LaMer-Dinegar growth curve (solid line in the figure), most of the metal precursors rapidly change to the -M-OH form in this stage. The generation speed highly depends on the temperature, that is, controlling the reaction temperature and heating rate are important at this stage for the high quality product.
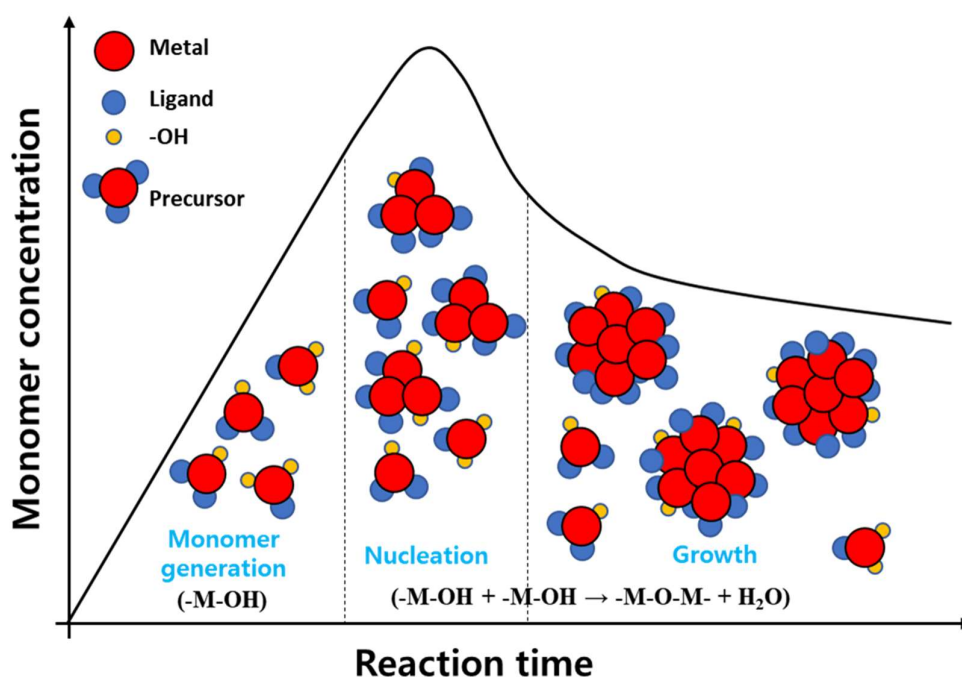
Figure 1.16 LaMer-Dinegar model of colloidal metal oxide NP synthesis, which involves the stage 1. Monomer generation; 2. Nucleation; 3. Growth.

In the nucleation stage, -M-OH turns into nuclei (*i.e.*, seeds) by self-condensation reaction of -M-OH.

$$\text{-M-OH + -M-OH} \rightarrow \text{-M-O-M- + H}_2\text{O} \tag{1.6}$$

16
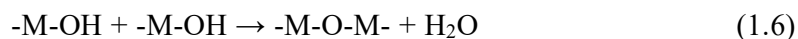
In the growth stage, the formed reaction nuclei are allowed to grow by further reaction between two or more nuclei or that between a nucleus and monomers. This growth process is however limited by solubility of the grown particles in the reaction medium. It is also important that the -M-O-M- bonding is very easily returned to -M-OH again by hydrolysis. Therefore, reaction parameters such as the temperature, the monomer concentration, the amount of water, and the rate of vapor emission have a great influence on the growth process.

1.5.2 Control of free charge carriers

To activate LSPR of compound NPs, there is a need for a method that can provide a sufficient level of the free charge carrier density. As mentioned in section 1.4.2, doping or vacancy formation can give a sufficient amount of free charge carriers to compound NPs. In this section, control methods for doping and vacancy are briefly discussed.

(a) Doping control

In the case of doping a metal oxide with another metal ion, two (or more) different metal complex precursors are used for the reaction. The doping ratio can be controlled by changing the concentration ratio of those precursors. However, quality of the resulting NPs depends on the balance in the reaction rate between those precursors (Figure 1.17). The NPs with homogeneous dopant distribution can be obtained when the reaction rates are the same. If the reaction rate of the dopant precursor is faster (or slower) than that of the host precursor, the doping ratio in the core region is higher (or lower) than that in the shell region of each NP. If the overall reaction rate is too fast or too slow, the quality of the resultant NPs, including NP size distribution, will be low. The balance in the reaction rates may be controlled by using different ligands for the host and dopant metal complexes.

Reaction rate difference between host and dopant
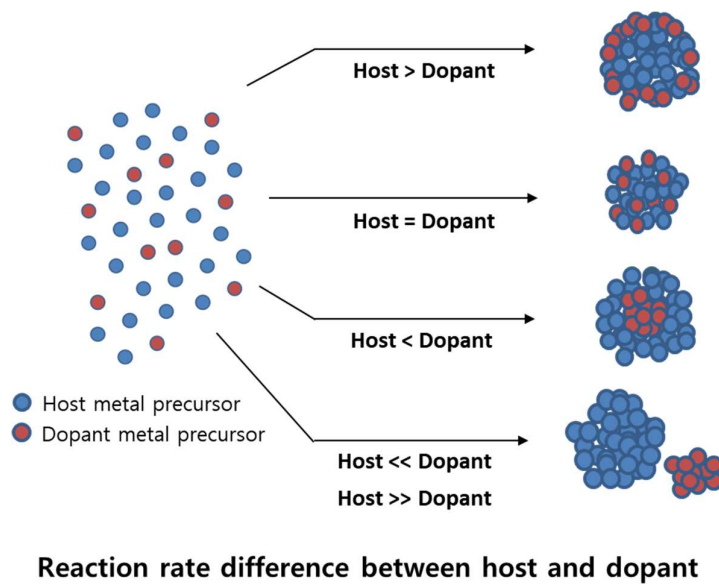
Figure 1.17 Illustration of host and dopant metal complex reactivity in the system

(b) Vacancy control

In the case of metal oxides such as MoO_3 and WO_3, oxygen vacancies are often introduced to them to increase their carrier density. In order to achieve this, reducing agents may be used.[39] Otherwise, an organic reaction system and a thick capping agent are required to remove oxygen from the reaction system to some extent.

1.5.3 Control of morphology

(a) Shape control

The methods of shape control have been known poorly in the case of plasmonic compound NPs. This is probably because the synthetic temperature is so high that the reactions are fast, and the fast reactions are difficult to control. Actually, for some cases with relatively low reaction temperature, shape-control of NPs has been reported.[35,43] In the control of NP shape, selecting kinetically or thermodynamically controled process could be important. An example for the synthesis of $Cu_{2-x}S$ NPs is shown in Figure 1.18. In this case, Sn-thiolate complexes increase the nucleation barrier of the synthesis system. As a result,

the growth of NPs slows down and thermodynamically controlled processes dominate the growth of NPs. Thus, a thermodynamically stable polyhedral form is selected. In the absence of Sn, nanoplate shape of NPs are formed that are kinetically favorable. This method is used for non-doped NPs, such as CuS, MoO_{3-x}, and WoO_{3-x}. In the case of doped compound NPs, it is very difficult to control the relative reaction rates of dopant and host precursors simultaneously.
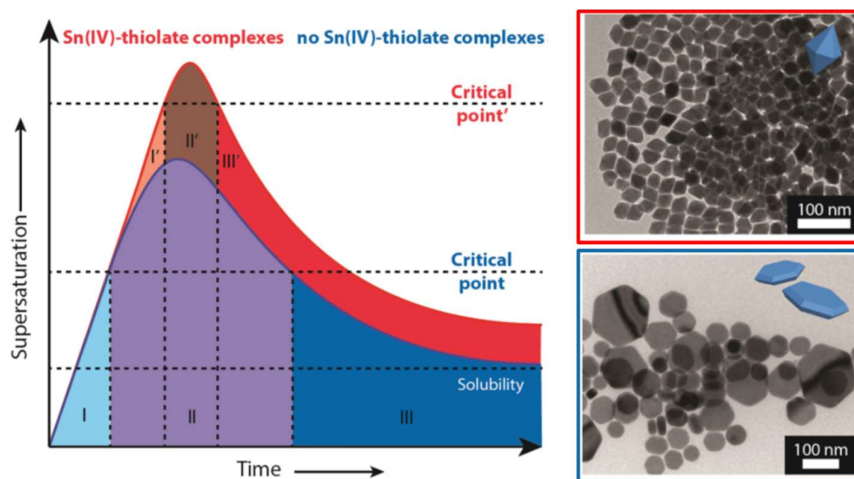
Figure 1.18 Illustration of La Mer plots of nucleation barrier difference between a system with and that without Sn-thiolate complex. In the presence of Sn-complex (red), thermodynamic growth results in polyhedral shape and in the absence (blue), nanoplates are formed through kinetic growth. Reprinted with permission from ref. 40. Copyright 2016 American Chemical Society.

(b) Size control

The size-controlled synthesis of plasmonic compound NPs is a very challenging subject, especially for synthesis of doped metal oxides, because in general synthetic methods, reactions are too fast to control. In the case of ITO NPs, however, size control of the NPs has been achieved by thoroughly controlling the reaction temperature and other synthesis conditions and cycling the synthesis process by using the synthesized ITO NPs as seeds in the next synthesis step,[44] as shown in (Figure 1.19). However, each synthesized

NP is not necessarily characterized by homogeneous dopant distribution, suggesting that control of the reactivity difference between the dopant and host precursors has not yet been achieved completely.
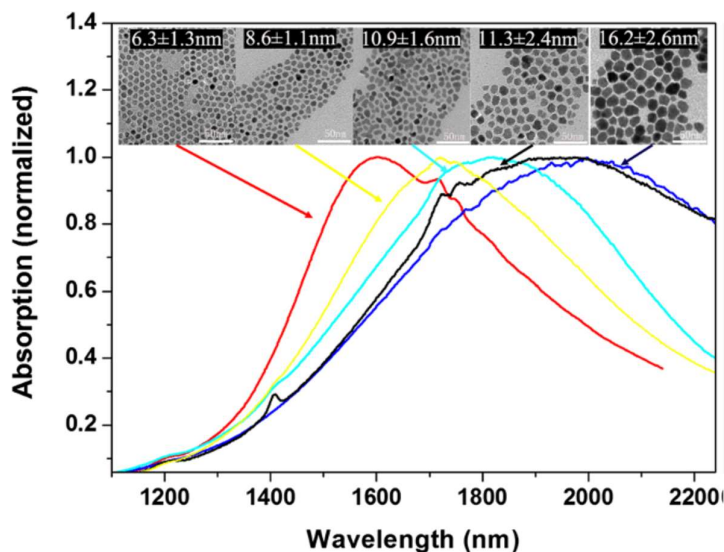
Figure 1.19 Size control of ITO NPs by a seed-mediated growth method. Reprinted with permission from ref. 44. Copyright 2014 Ma et al.; licensee Springer.

1.5.4 Issues in synthesis of plasmonic compound NPs

As described in the previous sections, LSPR of compound NPs has distinctive features that are different from metal NPs. Even so, there are several issues in synthesis of plasmonic compound NPs as follows.

1. Limited kinds of plasmonic compound NPs exhibit LSPR in the visible region. There is a need for methods of synthesizing plasmonic compound NPs for visible LSPR.

2. It is still difficult to control the size and shape of most plasmonic compound NPs. Development of synthesis methods for size- and shape-controlled NPs is important for understanding of plasmonic compound NPs.

3. Most of plasmonic compound NPs are covered by thick capping agents, which could limit their applications that are based on electron or ion exchange.

4. It is also difficult to control the doping. Better control methods of distribution of dopant and an analysis method to locate dopant species in each NP is needed.

Among those issues, the points 3 and 4 will be addressed in Chapter 2.

1.6 Plasmon-induced charge separation (PICS)

1.6.1 Overview of PICS

Light energy absorbed by LSPR of NPs and other nanomaterials has been used in various fields.[2,11,45] As explained above, the absorption based on LSPR is due to oscillation of free carriers at the surface of the nanomaterial. The energy absorbed by the LSPR of conventional nanomaterials is not high enough to extract an electron from the nanomaterials to vacuum. However, in recent studies it was found that electrons excited by LSPR can be extracted from the nanoparticles to a semiconductor.[46]

In 2005, at the interface between plasmonic Au NPs and TiO_2, it was confirmed that a photocurrent flows and its action spectrum perfectly matched the absorption spectrum of the NPs (Figure 1.20a).[1] These results were explained in terms of electron injection from Au NPs to the TiO_2 conduction band by overcoming the Schottky barrier at the interface, on the basis of an external photoelectric effect (Figure 1.20b).
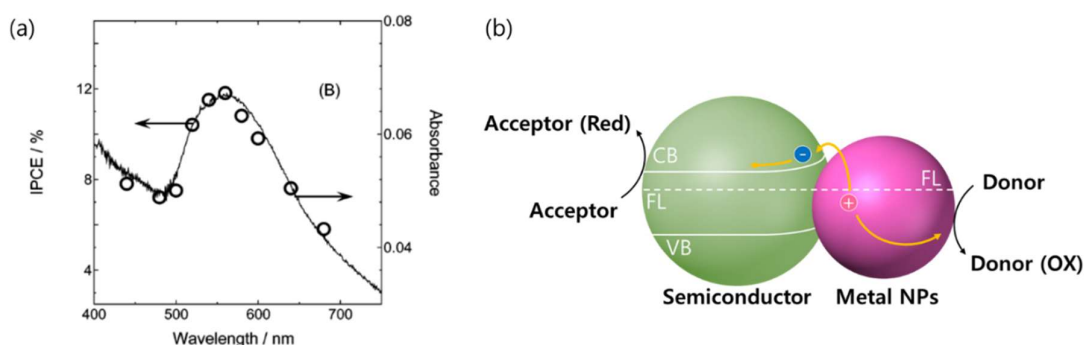
Figure 1.20 (a) Photocurrent action spectrum and the absorption spectrum of a TiO_2-Au system. Reprinted with permission from ref. 1. Copyright 2005 American Chemical Society. (b) Illustration of the mechanism of PICS.

In 2014, changes of the potential of Au nanoprisms on TiO$_2$ by PICS were observed by in situ nanoimaging using Kelvin probe force microscopy (KFM).[47] As shown in Figure 1.21, the potential at the Au surface was more negative than that at the TiO$_2$ surface under UV irradiation. Conversely, the potential at the Au nanoprism surface was more positive than that at the TiO$_2$ surface under NIR irradiation. That is, under the light corresponding to the LSPR of Au nanoprism, it is confirmed that the electron is injected into the TiO$_2$ conduction band from the Au nanoprism, giving rise to the potential difference.
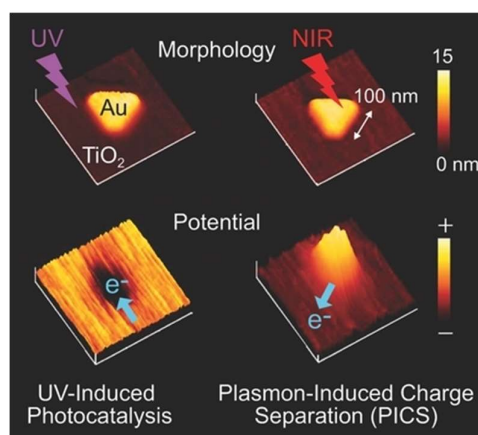
Figure 1.21 Potential changes evaluated by Kelvin probe force microscopy (KFM) for a Au nanoprism on TiO$_2$ under UV and NIR irradiation. Reprinted with permission from ref. 47. Copyright 2014 WILEY-VCH Verlag GmbH & Co. KGaA, Weinheim.

1.6.2 Mechanism of PICS

When a metal contact with an n-type semiconductor, and if the intrinsic Fermi level of the metal is lower (*i.e.*, more positive in potential) than the Fermi level of the semiconductor, a Schottky junction is formed at the metal-semiconductor interface (Figure 1.22).
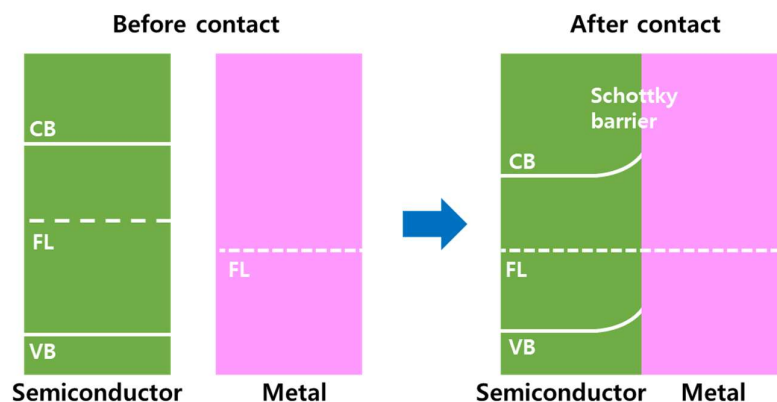
Figure 1.22 Illustration for Schottky junction formation; energy band diagrams of metal and n-type semiconductor before and after the contact.

Since some of the electrons of n-type semiconductors with a relatively high Fermi level move to the metal to achieve an equilibrium. As a result, band banding occurs in the semiconductor, and a Schottky barrier forms. The junction of a metal nanomaterial with a semiconductor should not be different significantly. It is well-known that combination of TiO_2 and Au or Ag gives Schottky junction. If Au or Ag is small enough that it can absorb light by LSPR, electrons excited by this absorbed light can be injected into TiO_2 to cause PICS (Figure 1.23).
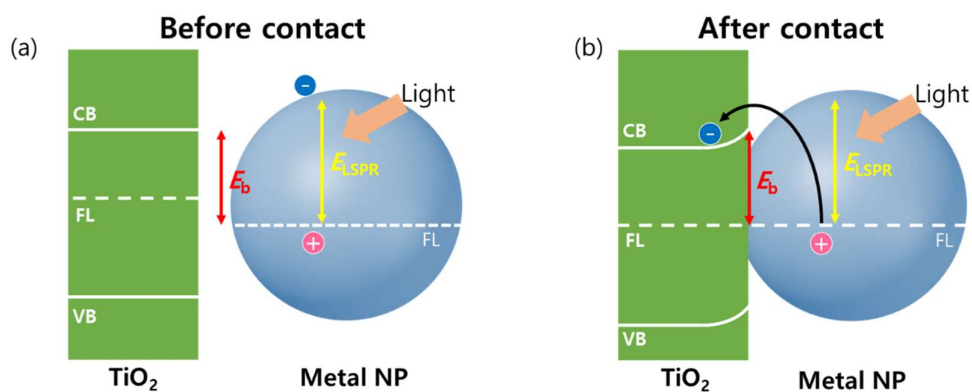
Figure 1.23 Illustration of Schottky junction at the interface between TiO_2 and a plasmonic metal NP under irradiation of light (a) before and (b) after contact.

In this case, the Schottky barrier at the interface between plasmonic Au or Ag and TiO$_2$ has a dominant influence on the characteristics of PICS. For PICS to occur, the energy of photon for LSPR, E_{LSPR}, must be larger than the energy corresponding to the Schottky barrier height, E_b. Furthermore, if the space charge layer (*i.e.*, the region in which the band bending occurs) is too thin, electrons injected into the semiconductor could be transferred back to metal by electron tunneling, resulting in charge recombination. The efficiency of the PICS is determined by those factors.

1.6.3 Applications of PICS

In what follows, some applications of PICS are described briefly.

(a) Photovoltaics

PICS can be applied to photovoltaic devices[1,6] since PICS mechanism includes an uphill electron transfer process. As shown in Figure 1.24, photovoltaic cells were designed for higher photoconversion efficiency (PCE) using a half-shell array with different metals. The cell with Ag half-shell array shows the highest PCE of ~0.1%. This value is higher than that of the previously developed cells based on PICS, but is lower than that of a typical practical solar cell (~20%). However, despite low PCE of PICS, there is a great advantage that the operating wavelength range of the photovoltaic cell can be easily adjusted by changing the absorption wavelength of the loaded NPs and nanostructures.
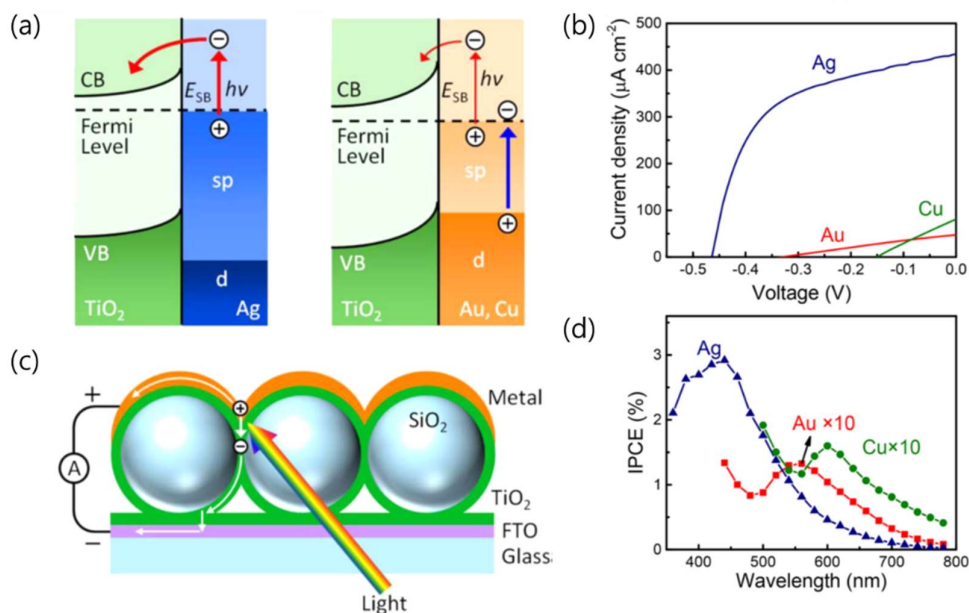
Figure 1.24 (a) PICS mechanism and (c) illustration of solid-state photovoltaic cells. (b) J-V curves and (d) photocurrent action spectra of the cells. Reprinted with permission from ref. 6. Copyright 2017 American Chemical Society.

(b) Photocatalysis

When PICS occurs, electrons and holes (or decayed positive charges) are separated from each other, allowing separate redox reactions. The efficiency of those photocatalytic reactions based on PICS could be improved by a p-type semiconductor with Pt co-catalyst coated on the TiO_2-Au system.[48] Actually, TiO_2/AuNP/NiO/Pt photoanode connected to a Pt counter electrode exhibited higher photoelectrochemical hydrogen evolution rate than the TiO_2/AuNP photoanode (Figure 1.25).
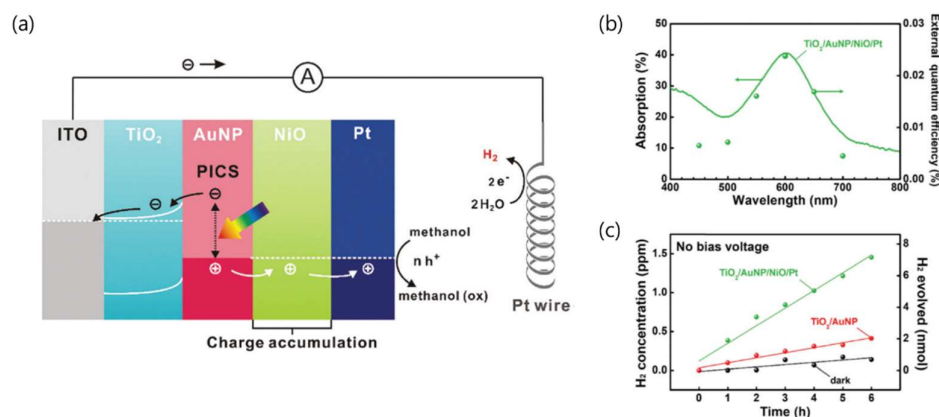
Figure 1.25 (a) Illustration of overall PICS reaction process with a $TiO_2/AuNP/NiO/Pt$ photoanode and a Pt wire counter electrode. (b) Corresponding action spectrum of prepared cell and (c) hydrogen evolution under short-circuit conditions. Reprinted with permission from ref. 48. Copyright the Owner Societies 2017.

(c) Sensors

　　As described in the previous section, LSPR can be applied to affinity-based chemical sensing and biosensing[49] on the basis of difference in peak position due to refractive index of the surrounding medium. Therefore, PICS responses can be used as signals of LSPR sensors.[5] In the case of an example shown in Figure 1.26, conductivity of a TiO_2 film on which Au NPs are deposited is measured as an LSPR sensor signal.
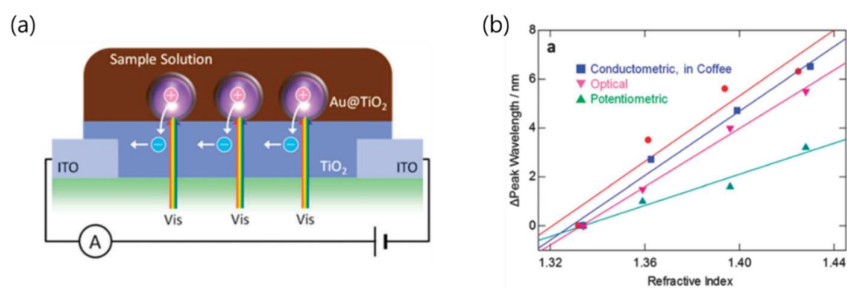
Figure 1.26 Mechanisms of the (a) conductometric LSPR sensor based on PICS and (b) refractive index sensitivity of the sensor with those of optical and potentiometric sensors. Reprinted with permission from ref. 5. Copyright the Royal Society of Chemistry 2015.

PICS is also used for photoinduced fabrication of nanomaterials beyond the diffraction limit. For example, selective etching of the top face or the bottom face of a Ag nanocube on TiO_2 is possible[50] (Figure 1.27a). Furthermore, the site-selective PICS can also be achieved under circularly polarized light for fabrication of chiral nanostructures[51] (Figure 1.27b).
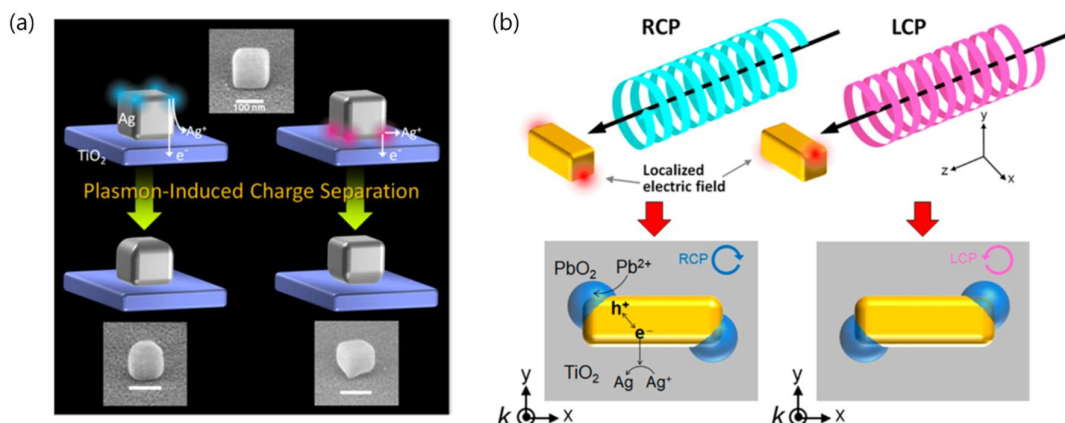
Figure 1.27 (a) Site-selective etching based on PICS for a Ag nanocube on TiO_2, Reprinted with permission from ref. 50. Copyright 2016 American Chemical Society. (b) Site-selective deposition of PbO_2 based on PICS on a Au nanocuboid on TiO_2 under the circularly polarized light for preparing chiral plasmonic nanostructures. Reprinted with permission from ref. 51. Copyright 2018 American Chemical Society.

1.6.4 Toward PICS of compound NPs

(a) Potentials

PICS has been studied widely since it can convert absorbed light energy through LSPR to a current flow. However, PICS has been achieved only by using noble metals. If the PICS can be extended to compound NPs, the range of its application will be broadened further. As shown in Figure 1.28a, solar energy contains a very large amount of NIR light. On the other hand, the noble metal NPs absorb only a part of the visible light. If PICS is achieved with compound NPs, it would allow the use of a wider range of solar energy.
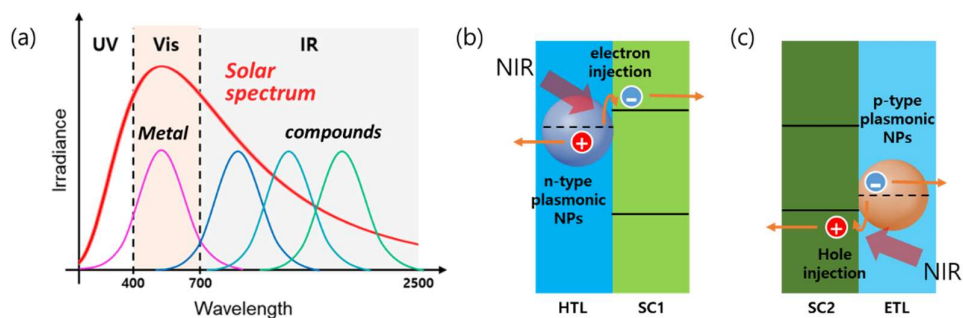
Figure 1.28 (a) Schematic illustration of solar spectra and typical LSPR spectra of some plasmonic NPs. Illustration of expected PICS mechanisms of (b) electron and (c) hole injection from compound NPs to a semiconductor. Solar energy contains a very large amount of NIR light, where HTL is hole transporting layer, ETL is electron transporting layer, and SC is semiconductor.

In addition, as described above, free charge carriers of plasmonic compound NPs are not limited to electrons.[52] This means that, with PICS of compound NPs, both electron injection to a semiconductor conduction band and hole injection to a semiconductor valence band would be possible as shown in Figure 1.28b and c, respectively. This phenomenon can be actively exploited in energy devices such as photon up-conversion.

(b) Difficulties

Despite its many advantages, attempts to observe PICS with plasmonic compound NPs have been failed. To achieve PICS, the electrons or holes excited by LSPR must have enough energy to jump over the Schottky barrier (Figure 1.29) Also, matching with a semiconductor with a Fermi level of modest difference is absolutely necessary to form Schottky barrier of appropriate height. In addition, the semiconductor used must have adequate levels of carrier mobility, stability, and suitable optical properties which do not interfere with the LSPR.
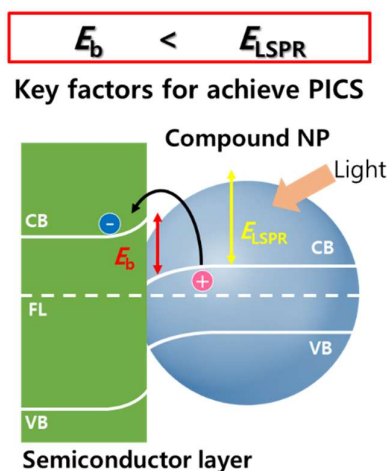
Figure 1.29 Key factors for achieving PICS of compound NPs.

There are the following difficulties in achieving PICS using plasmonic compound NPs. First, the LSPR energy is absolutely low compared to that of noble metal NPs. Most of commonly known plasmonic compound NPs have LSPR in the NIR or IR region, which means that the energy of electrons or holes that should be injected into semiconductor is relatively low. Thus, semiconductor materials with very precisely controlled band structures are required to obtain a Schottky barrier of appropriate height. Also, a capping agent that covers the plasmonic compound NPs could block the injection of electrons or holes from the NPs. Therefore, there is a need for minimizing the capping layer thickness. However, attention should be paid not to deteriorate the particle stability, since the surface modification of small particles will eventually lead to particle stability problems.

1.7 Purpose of this work

In spite of advantages of plasmonic compound NPs such as resonance with NIR and IR light, tunability, cost-effectiveness, and infinite combinations of materials, several drawbacks including thick capping agents covering the NPs and difficulty in control of doping still exist. In the present work, those drawbacks will be addressed by developing new synthetic methods for plasmonic compound nanomaterials. In addition, by using those

plasmonic nanomaterials, PICS will be achieved, on the basis of both electron injection and hole injection.

In Chapter 2, plasmonic ITO NPs protected by a short ligand were synthesized by a new synthetic method. Doping ratio and dopant distribution in each NP were controlled by the method. In addition, plasmonic MoO_2 and MoO_{3-x} NPs were synthesized. The degree of oxidation and plasmonic properties of NPs were controlled by changing the synthetic conditions or oxidizing and reducing the NPs. Also, nanostructured MoO_{3-x} was fabricated by using metal oxide or metal NP ensemble as a template. Their LSPR characteristics were controlled by the concentration of the template NPs.

In Chapter 3, PICS was achieved on the basis of hole injection from the nanostructured MoO_{3-x} to TiO_2. Solid-state photovoltaic cells with $ITO|TiO_2|NPs|MoO_{3-x}|Ag$ structure were developed and examined. The cells exhibited photoresponses in the 700-1400 nm range.

In Chapter 4, PICS was achieved on the basis of electron injection from the synthesized ITO NP to TiO_2. Solid-state photovoltaic cells with $ITO|TiO_2|ITO NPs|Ag$ structure and a cell with $ITO|TiO_2|ITO NPs|MoO_3|Ag$ structure were developed and characterized. The cells exhibited photoresponses in the 1400-2200 nm range. The cell performance was optimized by tuning the doping ratio of the ITO NPs and the thickness of the ITO NP layer.

Thus, PICS of plasmonic compound NPs was achieved for the first time on the basis of both electron injection and hole injection. Also, the longer wavelength limit of PICS was extended from 1700 nm to 2200 nm.

1.8 References

1   Y. Tian and T. Tatsuma, *J. Am. Chem. Soc.*, 2005, **127**, 7632–7637.

2   T. Tatsuma, H. Nishi, and T. Ishida, *Chem. Sci.*, 2017, **8**, 3325–3337.

3   Y. Takahashi and T. Tatsuma, *Appl. Phys. Lett.*, 2011, **99**, 1–4.

4   E. Kowalska, R. Abe, and B. Ohtani, *Chem. Commun.*, 2009, 241–243.

5   T. Tatsuma, Y. Katagi, S. Watanabe, K. Akiyoshi, T. Kawawaki, H. Nishi, and E. Kazuma, *Chem. Commun.*, 2015, **51**, 6100–6103.

6   L. Wu, G. M. Kim, H. Nishi, and T. Tatsuma, *Langmuir*, 2017, **33**, 8976–8981.

7   K. Kawahara, Y. Ohko, T. Tatsuma, and A. Fujishima, *Phys. Chem. Chem. Phys.*, 2003, **5**, 4764.

8   T. Tatsuma, K. Takada, and T. Miyazaki, *Adv. Mater.*, 2007, **19**, 1249–1251.

9   T. Yamaguchi, E. Kazuma, N. Sakai, and T. Tatsuma, *Chem. Lett.*, 2012, **41**, 1340–1342.

10   Y. Xia, Y. Xiong, B. Lim, and S. E. Skrabalak, *Angew. Chem. Int. Ed.*, 2009, **48**, 60–103.

11   M. Rycenga, C. M. Cobley, J. Zeng, W. Li, C. H. Moran, Q. Zhang, D. Qin, and Y. Xia, *Chem. Rev.*, 2011, **111**, 3669–3712.

12   K. Manthiram and A. P. Alivisatos, *J. Am. Chem. Soc.*, 2012, **134**, 3995–3998.

13   H. Takeda and K. Adachi, *J. Am. Ceram. Soc.*, 2007, **90**, 4059–4061.

14   H. Cheng, T. Kamegawa, K. Mori, and H. Yamashita, *Angew. Chem. Int. Ed.*, 2014, **53**, 2910–2914.

15   W. Liu, Q. Xu, W. Cui, C. Zhu, and Y. Qi, *Angew. Chem. Int. Ed.*, 2017, **56**, 1600–1604.

16   C. Zhu, Q. Xu, L. Ji, Y. Ren, and M. Fang, *Chem. Asian J.*, 2017, **12**, 2980–2984.

17   J. Shi, Y. Kuwahara, M. Wen, M. Navlani-García, K. Mori, T. An, and H. Yamashita, *Chem. Asian J.*, 2016, **11**, 2377–2381.

18   Q. Q. Zhang, X. Li, Q. Ma, Q. Q. Zhang, H. Bai, W. Yi, J. Liu, J. Han, and G. Xi, *Nat. Commun.*, 2017, **8**, 14903.

19   Y. Zhao, H. Pan, Y. Lou, X. Qiu, J. Zhu, and C. Burda, *J. Am. Chem. Soc.*, 2009, **131**, 4253–4261.

20   M. Kanehara, H. Koike, T. Yoshinaga, and T. Teranishi, *J. Am. Chem. Soc.*, 2009, **131**, 17736–17737.

21   W. He, K. Ai, C. Jiang, Y. Li, X. Song, and L. Lu, *Biomaterials*, 2017, **132**, 37–47.

22   S. H. Lee, H. Nishi, and T. Tatsuma, *Nanoscale*, 2018, **10**, 2841–2847.

23   P. K. Jain, X. Huang, I. H. El-Sayed, and M. A. El-Sayed, *Acc. Chem. Res.*, 2008, **41**, 1578–1586.

24   J. M. Luther, P. K. Jain, T. Ewers, and A. P. Alivisatos, *Nat. Mater.*, 2011, **10**, 361–366.

25   V. Amendola and M. Meneghetti, *Phys. Chem. Chem. Phys.*, 2009, **11**, 3805–3821.

26   S. Szunerits and R. Broukherroub, *Chem. Commun.*, 2012, **48**, 8999–9010.

27   Q. Zhang, W. Li, C. Moran, J. Zeng, J. Chen, and V. Re, *J. Am. Chem. Soc.*, 2010, **132**, 11372–11378.

28 J. Zeng, S. Roberts, and Y. Xia, *Chem. Eur. J.*, 2010, **16**, 12559–12563.

29 J. Reguera, J. Langer, D. Jiménez De Aberasturi, and L. M. Liz-Marzán, *Chem. Soc. Rev.*, 2017, **46**, 3866–3885.

30 S. Liu, G. Chen, P. N. Prasad, and M. T. Swihart, *Chem. Mater.*, 2011, **23**, 4098–4101.

31 S. D. Lounis, E. L. Runnerstrom, A. Llordés, and D. J. Milliron, *J. Phys. Chem. Lett.*, 2014, **5**, 1564–1574.

32 C. Battaglia, X. Yin, M. Zheng, I. D. Sharp, T. Chen, S. Mcdonnell, A. Azcatl, C. Carraro, B. Ma, R. Maboudian, R. M. Wallace, and A. Javey, *Nano Lett.*, 2014, **14**, 967–971.

33 M. T. Greiner, L. Chai, M. G. Helander, W. M. Tang, and Z. H. Lu, *Adv. Funct. Mater.*, 2012, **22**, 4557–4568.

34 K. Asami, H. Nishi, and T. Tatsuma, *Nanoscale*, 2016, **8**, 14092–14096.

35 T. R. Gordon, T. Paik, D. R. Klein, G. V Naik, H. Caglayan, A. Boltasseva, and C. B. Murray, *Nano Lett.*, 2013, **13**, 2857–2863.

36 S. W. Hsu, W. Bryks, and A. R. Tao, *Chem. Mater.*, 2012, **24**, 3765–3771.

37 X. Ye, J. Fei, B. T. Diroll, T. Paik, and C. B. Murray, *J. Am. Chem. Soc.*, 2014, **136**, 11680–11686.

38 S. D. Lounis, E. L. Runnerstrom, A. Bergerud, D. Nordlund, and D. J. Milliron, *J. Am. Chem. Soc.*, 2014, **136**, 7110–7116.

39 Y. Li, J. Cheng, Y. Liu, P. Liu, W. Cao, T. He, R. Chen, and Z. Tang, *J. Phys. Chem. C*, 2017, **121**, 5208–5214.

40 A. Agrawal, S. H. Cho, O. Zandi, S. Ghosh, R. W. Johns, and D. J. Milliron, *Chem. Rev.*, 2018, **118**, 3121–3207.

41 A. W. Jansons and J. E. Hutchison, *ACS Nano*, 2016, **10**, 6942–6951.

42 S. Luo, J. Feng, and K. M. Ng, *CrystEngComm*, 2015, **17**, 1168–1172.

43 W. Van Der Stam, S. Gradmann, T. Altantzis, X. Ke, M. Baldus, S. Bals, and C. D. M. Donega, *Chem. Mater.*, 2016, **28**, 6705–6715.

44 K. Ma, N. Zhou, M. Yuan, D. Li, and D. Yang, *Nanoscale Res. Lett.*, 2014, **9**, 547.

45 K. A. Willets and R. P. Van Duyne, *Annu. Rev. Phys. Chem.*, 2007, **58**, 267–297.

46 Y. Tian and T. Tatsuma, *Chem. Commun.*, 2004, **10**, 1810–1811.

47 E. Kazuma and T. Tatsuma, *Adv. Mater. Interfaces*, 2014, **1**, 2–5.

48 K. C. Kao, Y. Kuroiwa, H. Nishi, and T. Tatsuma, *Phys. Chem. Chem. Phys.*, 2017, **19**, 31429–31435.

49 A. Csáki, O. Stranik, and W. Fritzsche, *Expert Rev. Mol. Diagn.*, 2018, **18**, 279–296.

50 K. Saito, I. Tanabe, and T. Tatsuma, *J. Phys. Chem. Lett.*, 2016, **7**, 4363–4368.

51 K. Saito and T. Tatsuma, *Nano Lett.*, 2018, **18**, 3209–3212.

52 H. Nishi, K. Asami, and T. Tatsuma, *Opt. Mater. Express*, 2016, **6**, 1043.

Chapter 2

Synthesis and tuning of plasmonic compound nanomaterials

2.1 Introduction

As described in 1.5.4, there are several issues in synthesis of plasmonic compound NPs. One of the most important things that should be considered is thick capping agents around the NPs since contact of plasmonic NPs with a semiconductor has a critical effect on PICS.[1,2] Limited kinds of compound NPs which exhibit LSPR in the visible region are also a problem. Because plasmonic compound NPs show LSPR basically in NIR region[3] in which photon energy is relatively low, it is difficult for carriers excited by LSPR to overcome an energy barrier at the NP-semiconductor interface. For the above reasons, preparation methods of compound NPs which are suitable for PICS applications have to be considered.

In this chapter, three kinds of plasmonic compound NPs, *i.e.*, ITO, MoO_2, and MoO_{3-x} NPs, are chosen as target materials and their synthetic methods are developed because the NPs show LSPR peak ranging from visible to NIR region (Figure 2.1).[4-6] For synthesis of ITO NPs, a reverse hot injection method is developed not only to shorten the capping agent but also to control particle size, doping ratio, and doping distribution. A new non-aqueous synthetic method for visible light-responsive MoO_2 and MoO_{3-x} NPs is also developed. Finally, plasmonic nanostructures of MoO_{3-x} are fabricated by thermal vapor deposition of MoO_3 onto NP ensembles as templates without using capping agent.
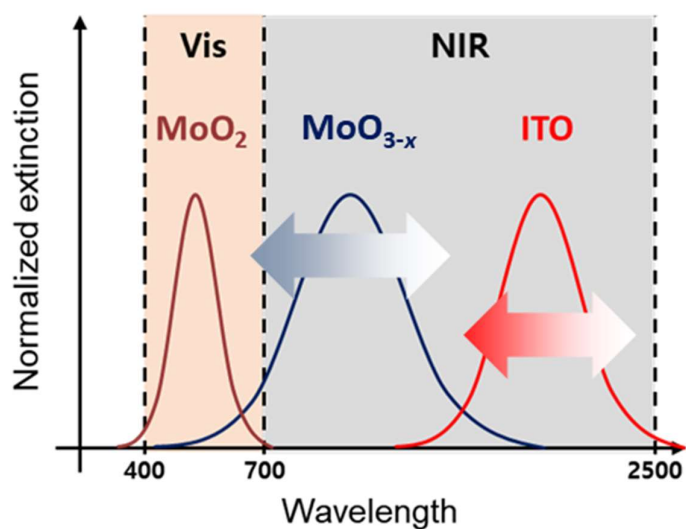
Figure 2.1, LSPR absorption range of MoO$_2$, MoO$_3$, and ITO NPs.

2.2 Experimental

2.2.1 Materials

Indium(III) acetate (In(ac)$_3$), tin(IV) acetate (Sn(ac)$_4$), molybdenum dioxide bis(acetylacetonate) (MoO$_2$(acac)$_2$, MDBA), oleic acid (C$_{18}$A: 90%), titanium diisopropoxide bis(acetylacetonate), and chloroplatinic acid hexahydrate (H$_2$PtCl$_6$) were commercially available from Sigma-Aldrich. 1-octadecene (ODE: 90%), octanoic acid (C$_8$A: 98%), decanoic acid (C$_{10}$A: 99%), myristic acid (C$_{14}$A: 90%), methanol (99.8%), ethanol (99.8%), toluene (99%), hexane (96%), chloroform (99%), tetrahydrofuran (99.5%), formic acid (98%), o-xylene (98%), oleylamine (90%), MoO$_3$ (99.9%), and cyclohexane (99.7%) were purchased from Wako Pure Chemical Industries. Gold(III) chloride tetrahydrate (HAuCl$_4$·4H$_2$O: 99%) was purchased from Tokuriki Honten. Polystyrene-*b*-poly(2-vinyl pyridine) (M_n = 175000 (PS), 70000 (P2VP), M_w/M_n = 1.08) was obtained from Polymer Source. All reagents were used without further purification.

2.2.2 Characterization

X-ray diffraction (XRD) patterns were collected using a Rigaku D/MAX 2500V. Scanning electron microscopy (SEM) images were obtained on a JSM-7500FA. Transmission electron microscope (TEM) images were taken by a JEOL JEM-2010F with an acceleration voltage of 200 kV. Inductively coupled plasma mass spectrometry (ICP-MS) was carried out using a Seiko Instrument Inc SPQ-9000. Optical spectra were measured using a Jasco V-670 UV-vis spectrophotometer. X-ray photoelectron spectroscopy (XPS) measurements were performed using a Phi Quantera SXM.

2.2.3 Synthesis of ITO NPs

ITO NPs with different doping ratio of Sn% (10, 9, 5, and 2.5 mol% Sn) were synthesized by a reverse hot injection method as follows. A mixture of an ODE (2.5 mL) suspension of In(ac)$_3$ (0.16$-x$ mmol), Sn(ac)$_4$ (x mmol, x = 0.016, 0.014, 0.009, and 0.004 for 10, 9, 5, and 2.5 mol% Sn, respectively), and fatty acid (FA, C$_8$A, C$_{10}$A, C$_{14}$A, and C$_{18}$A, 0.57 mmol) were stirred at 150 °C under a nitrogen atmosphere for 1 h to form indium(III) and tin(IV) precursors. The mixture was degassed at 110 °C for 30 min. Before increasing the reaction temperature to 150 °C, gas phase in the sealed reactor was replaced with nitrogen using the Schlenk technique. After heating at 150 °C for 10 min, the reaction temperature was rapidly raised up to 300 °C and the mixture was further heated for 10 min before injection of oleylamine (0.8 mmol) using a syringe. After the injection, the mixture was stirred further for 1 h at 280 °C for the growth of ITO NPs. A mixture of toluene and ethanol (1:12 by volume) was used for purification by repeated centrifugation at 5500g for 2 min. The product thus obtained was dried at 80 °C for 10 min and re-dispersed in toluene (1 mL).

2.2.4 Synthesis of molybdenum oxide NPs

MDBA (0.03 mmol) was added to a FA (C$_8$A, C$_{10}$A, and C$_{18}$A) or its mixture with ODE (the compositions are listed in Figure 2.15) in a test tube. The total amount of mixture

was fixed as 2 mL. The gas phase in the sealed test tube was replaced with nitrogen using the Schlenk technique. Then, the sealed test tube was heated to 50 °C for 5 min and stirred for 1 h at 200 °C to grow molybdenum oxide NPs. For the optical spectrum measurements, the resulting solution was moved to a centrifuge tube and 6 mL of toluene was added for centrifugation at 5500 g for 1 min. Precipitates were removed by filtration and the solution was diluted with toluene by 84-fold. For the characterization of the NPs, the as-prepared solution was transferred to a centrifugal tube and 6 mL of methanol and 100 μL of toluene were added for centrifugation at 8500 g for 10 min. The obtained NPs in the precipitate were further purified by the same centrifugation procedure at least twice. The obtained product was vacuum dried for 1 h before re-dispersion in the desired solvent (typically toluene, 2 mL)

2.2.5 Fabrication of MoO_{3-x} nanostructures

NP ensembles of different kinds of materials (ITO, In_2O_3, Au, and Pt) were prepared on a glass substrate. ITO (10, 5, and 3 mol% Sn) NPs were prepared by the method described in 2.2.3. In_2O_3 NPs were synthesized without using $Sn(ac)_4$. The NP suspension (0.04–0.20 wt%) was spin-coated on the glass substrate, followed by exchanging the capping agents with formic acid[7] and vacuum drying.

Au NPs were prepared by a block copolymer micelle nanolithography.[8,9] Polystyrene-b-poly(2-vinyl pyridine) was dissolved in o-xylene (2 mg mL^{-1}) and kept stirring for 24 h. $HAuCl_4 \cdot 3H_2O$ was mixed with the copolymer micelle solution in which the molar ratio of Au to pyridine unit was 0.5. The Au-loaded micelles were spin-coated onto the substrate (2000 rpm, 30 s). Then, the substrate was treated with oxygen plasma (100 W for 5 min) and calcined at 350 °C for 4 h to remove organic residues.

Pt NP ensembles were fabricated on a TiO_2 layer deposited on a glass substrate through photocatalytic reduction of H_2PtCl_6 under UV irradiation[10] as follows. The TiO_2 layer was deposited by a spray pyrolysis method[11] at 550 °C from an isopropanol solution

containing titanium diisopropoxide bis(acetylacetonate) (0.37 M) (annealing time: 1 h). H_2PtCl_6 dissolved in a mixture of ultrapure water and ethanol (1:1 by volume) (0.1 mM, 0.55 mL) was drop cast onto the TiO_2 substrate and UV light (50 mW cm^{-2}) was irradiated for 10 min.

The desired thickness of MoO_3 was deposited onto the prepared NP ensembles by thermal vapor deposition (0.03–0.04 nm s^{-1}, $<4 \times 10^{-3}$ Pa).

2.3 Results & discussion

2.3.1 Synthesis of ITO NPs

One of the most studied compound plasmonic materials is ITO NPs.[6,7,12,13] This is because ITO has a relatively high free charge carrier density and has been used as a conductive material for a long time. ITO NPs have been prepared typically by a hot injection method, in which an In and Sn precursor solution is added quickly to a hot coordinating solvent such as oleyl alcohol heated at around 290 °C (Figure 2.2a)[13] so as to drive the reaction of In and Sn precursors at the same rate. However, capping agents with long alkyl chain are used typically to control size, colloidal stability, and dispersibility. Although, the capping agents can be exchanged with shorter ones,[14] the process could make the NPs unstable.
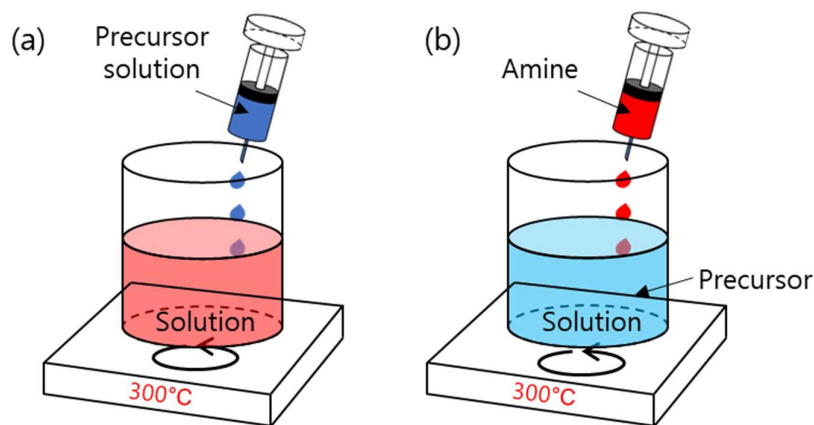
Figure 2.2 Schematic illustrations of (a) conventional hot injection method and (b) reverse hot injection method.

In order to deal with the issue, a reverse hot injection method was developed. Oleylamine, which induces ITO formation, is added to a hot In and Sn precursor (In and Sn carboxylates with C_8A, $C_{10}A$, and $C_{14}A$) solution heated at 300 °C (Figure 2.2b). The advantage of this method is that doping ratio and doping distribution can be controlled more precisely by alkyl chain length of the precursors as discussed later.

First, C_8A was used to synthesize ITO NPs with shorter capping agents. Ratio of Sn precursor to In one in the reaction solution was changed to control Sn doping ratio (0, 5.3, 8.7, 10, 12.5, and 16.7 mol% Sn). Figure 2.3 shows extinction spectra and photographs of the synthesized ITO NPs in toluene. The chemical composition in the NP was determined by ICP-MS. In_2O_3 NPs (0 mol% Sn) did not show any peak in the measured range (500-2300 nm). Extinction peaks derived from LSPR were observed in the spectra of ITO NPs (5.3, 8.7, 10, 12.5, and 16.7 mol% Sn). The peak was blueshifted and its intensity increased with increasing the doping ratio from 0 to 10% due an increase of the free electron density in the NPs. Meanwhile, the peak was redshifted and its intensity was decreased when Sn ratio was more than 10% because surplus Sn acts as a defect site and reduces free charge carrier density. These results are quite well matched with ITO NPs prepared by the conventional pyrolysis method.[6]
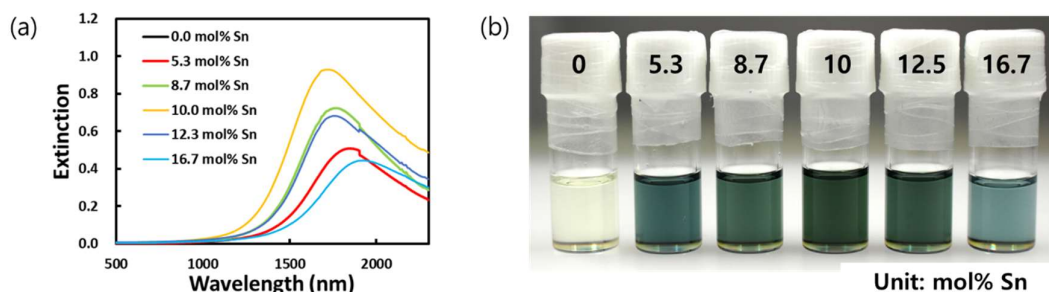
Figure 2.3 (a) Extinction spectra and (b) photographs of toluene solutions of ITO NPs with different doping ratio (0−16.7 mol% Sn) covered with C_8A.

Colloidal stability of the ITO NPs capped with C_8A was relatively low in toluene (around 1-2 months at room temperature and more than 6 months at 4 °C) compared to ITO NPs capped with $C_{18}A$ (more than a year at room temperature). Furthermore, the ITO NPs covered with $C_{18}A$ were soluble both in toluene and hexane whereas those with C_8A were soluble in toluene but insoluble in hexane, indicating that the C_8A-capped NPs were in less hydrophobic nature and ITO NPs capped with short capping agents were successfully prepared.

SEM images of C_8A-capped (5.3, 10, and 16.7 mol% Sn) and $C_{18}A$-capped ITO NPs (5.3 mol% Sn) are shown in Figure 2.4. Each sample has spherical shape and relatively narrow size distribution. Diameter of the C_8A-capped ITO NPs (Figure 2.4a-c) was 7-10 nm with similar size distribution. Thus, it was found that ITO NPs with shorter capping agents, different doping ratio, and a similar size distribution were successfully obtained by the reverse hot injection method. Diameter of $C_{18}A$-capped ITO NPs (Figure 2.4d) was, however, 12-14 nm, suggesting that alkyl chain length of the precursor affects particle size. The effect of alkyl chain length is discussed later.
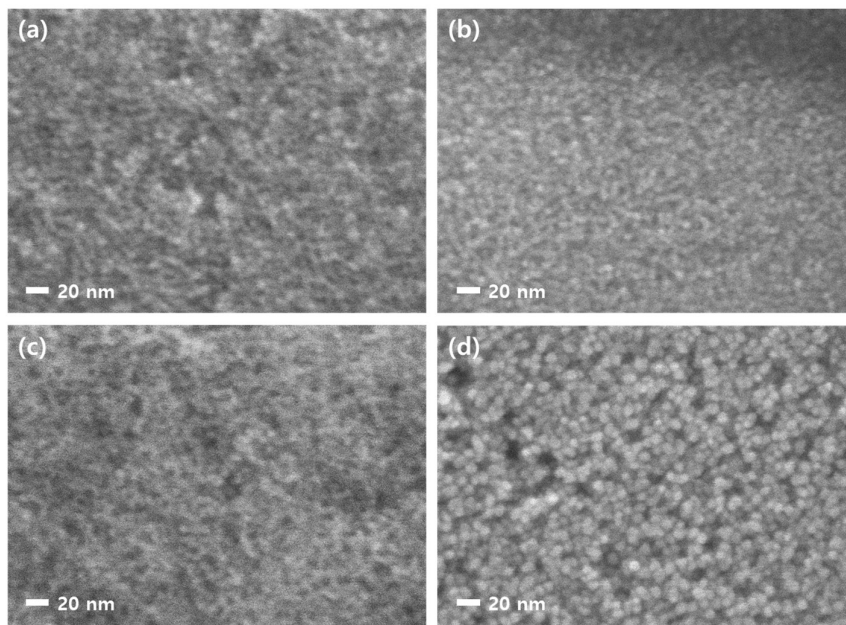
Figure 2.4 SEM images of (a-c) C_8A-capped ITO NPs with (a) 5.3 mol%, (b) 10 mol %, and 16.7 mol% Sn and (d) $C_{18}A$-capped ITO NPs with 5.3 mol% Sn.

ICP-MS was carried out to determine actual doping ratio in the ITO NPs. A relationship between Sn ratio in the reaction solution and that in the NP is shown in Figure 2.5. There is a linear relationship for C_8A-capped ITO NPs, indicating that chemical composition of the NPs can be controlled precisely by that in the feed solution. On the other hand, only ~2 mol% Sn was induced from the reaction solution containing 10 mol% Sn in the case of $C_{18}A$-capped ITO NPs, which means that alkyl chain length of the precursor affects not only particle size (Figure 2.4) but also doping ratio (Figure 2.5).
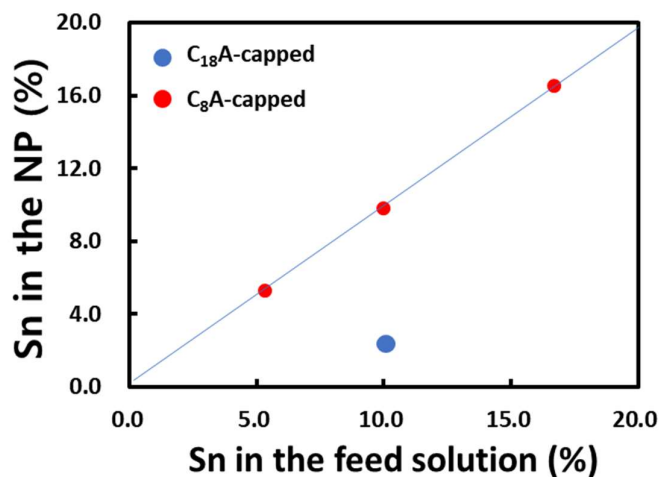
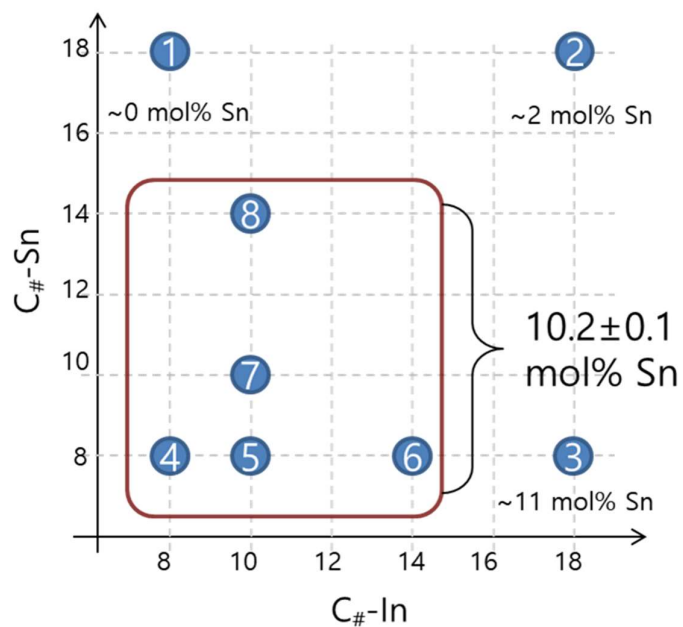**Figure 2.5** Relationship between Sn ratio in the reaction solution and that in the resulting ITO NP.

For further characterization of the C_8A-capped NPs, their XRD pattern was measured and shown in Figure 2.6. Although the NPs are too small to obtain clear XRD pattern, the diffraction peaks are matched relatively with those of bixbyite-type (cubic) In_2O_3.
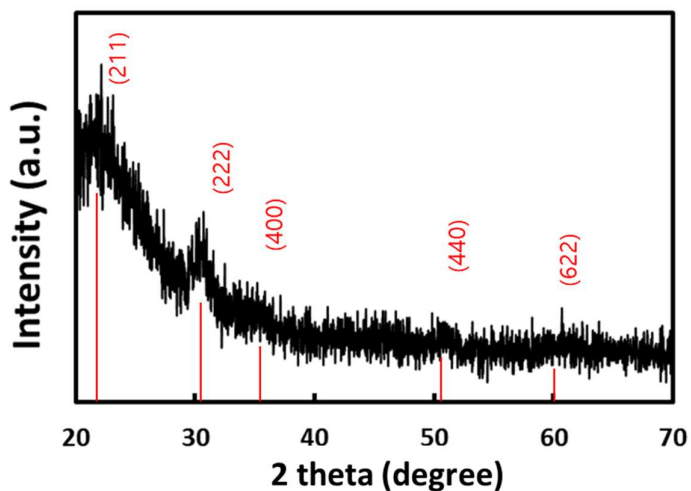

Figure 2.6 XRD pattern of C_8A-capped ITO NPs (10 mol% Sn). Reference XRD pattern of bixbyite-type In_2O_3 is also shown in the figure.

As described above, alkyl chain length of FA affects size and Sn doping ratio of ITO NPs (Figure 2.4 and 2.5). Thus, effects of the chain length were investigated and discussed using $C_{10}A$ and $C_{14}A$ in addition to C_8A and $C_{18}A$. ITO NPs were prepared by using In and Sn precursors with different alkyl chain lengths. For instance, In octanoate (complex of C_8A and In(III)) and Sn oleate (complex of $C_{18}A$ and Sn (IV)) were prepared separately and used for ITO NPs synthesis. Sn ratio in the reaction solution was fixed to 10 mol%. The combination of the precursor and doping ratio in the resulting NPs are summarized in Figure 2.7. Numbers in the blue solid circle represent sample numbers. Sample 2 and Sample 4 correspond to those in Figure 2.4. As can be seen in the figure, doping ratio in the prepared ITO NPs corresponds well to that in the feed solution for Sample 4-8 capped with C_8A, $C_{10}A$, and/or $C_{14}A$. Meanwhile, chemical composition in Sample 1-3 prepared in the presence of $C_{18}A$ did not match with that in the reaction solution. These results strongly suggest that reaction rate of the In and Sn precursors with $C_{8-14}A$ is very similar to each other while the precursors with $C_{18}A$ have lower reactivity because of large steric hindrance of the alkyl chain (Figure 2.8). Actually, size distribution of Sample 4-8 is very similar to each other (Figure 2.9).
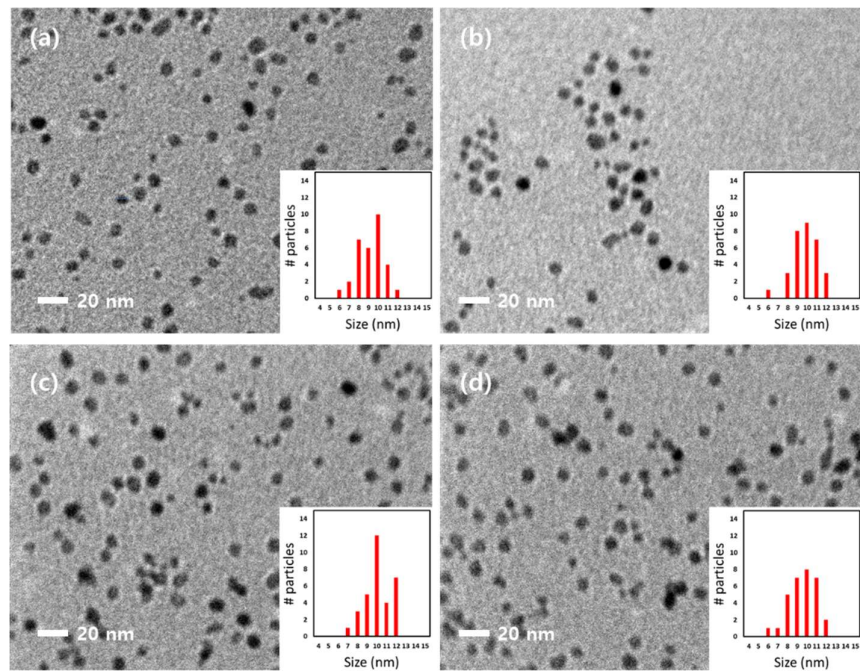
Figure 2.7 Relationship between reaction condition (combination of precursors) and doping ratio of the resulting NPs. Sn ratio in the feed solution is set to 10 mol%.
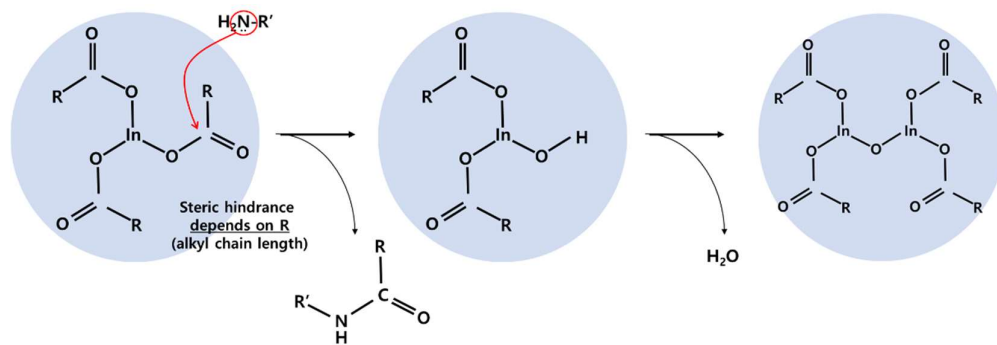

Figure 2.8 Reaction mechanism to form ITO NPs and effect of alkyl chain length of the precursors.

Figure 2.9 TEM images of Sample (a) 4, (b) 5, (c) 7, and (d) 8 prepared with various combinations of the precursors. Particles size distributions are shown in insets.

It should be noted that spectral width and symmetry of the extinction spectra of Sample 4-8 are different from each other (Figure 2.10) even though size distribution is almost the same as shown in Figure 2.9. This phenomenon could be explained in terms of doping distribution in the NPs. Lounis *et al.* demonstrated theoretically that surface segregation of Sn has a strong effect on spectral shape of a plasmonic ITO NP (Figure 2.11).[12,15] According to the calculation results, peak width of the absorption spectrum becomes narrower and the peak wavelength is redshifted as the dopant (Sn) concentration on the surface increases. At the same time, spectral shape becomes more symmetric. Spectra in Figure 2.10 showed the same tendency in the calculation results: the extinction peak was red-shifted, the peak width became narrower, and the spectral shape became more symmetric when In precursor with shorter alkyl chain or Sn precursor with longer alkyl chain was used. This trend can be also explained in terms of reactivity of the precursors depending on alkyl chain length (Figure 2.8). If the reaction rate of Sn precursor becomes slower than In one due to longer alkyl chain, Sn should be induced into the NPs after

formation of In_2O_3 NPs, resulting in surface segregation of Sn. Thus, it was concluded that the present method can control not only doping ratio and particle size but also doping distribution.
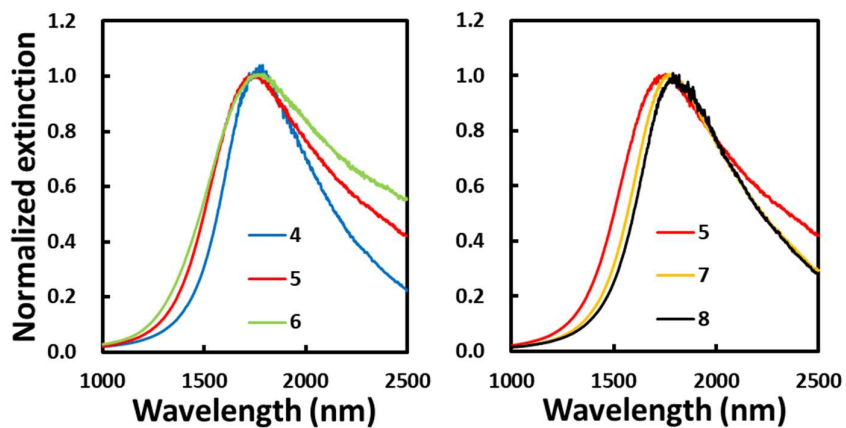
Figure 2.10 Extinction spectra of Sample 4-8 dispersed in toluene.
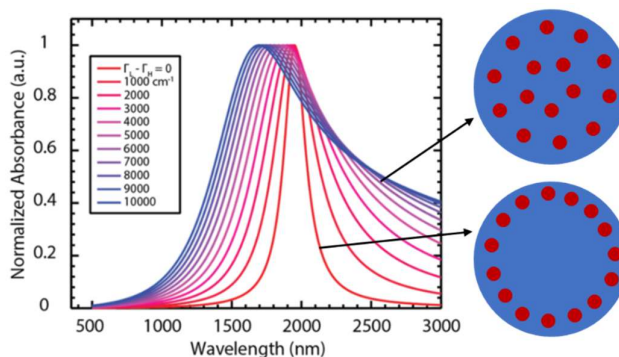
Figure 2.11 Calculated absorption spectra of ITO NPs with different Sn distributions. Red and blue curves indicate spectra for ITO NPs with surface segregated Sn and uniformly doped Sn, respectively. Blue sphere and red spheres represent In_2O_3 and Sn atoms, respectively. Reprinted with permission from ref. 12. Copyright 2014 American Chemical Society.

According to above discussion, doping distribution in C_8A-capped ITO NPs shown

46

in Figure 2.3a can be estimated from the spectral shape (Figure 2.10). LSPR peak became wider and more asymmetric with increasing the doping ratio, indicating that Sn atoms are induced from the surface of the NPs first and then distributed over the entire particles when only C_8A is used as the capping agent.

2.3.4 Synthesis of MoO_2 and MoO_{3-x} NPs

As described in 1.4.3, MoO_{3-x} NPs exhibit LSPR at 620–950 nm.[5,16,17-20] Recently, it was reported that MoO_2 NPs show LSPR in the visible region (Figure 2.12).[4] As summarized in the table in Figure 2.13, plasmonic MoO_2 and MoO_{3-x} NPs have been synthesized by high pressure hydrothermal methods.[4,5,16,17-20] Here, a new non-aqueous synthetic method for MoO_2 and MoO_{3-x} NPs under ambient pressure was developed and oxygen composition in molybdenum oxide NPs was regulated.
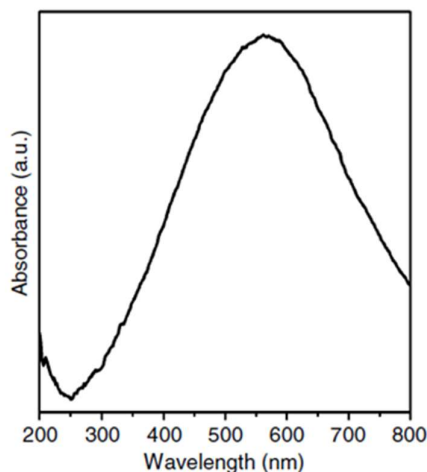

Figure 2.12 Absorption spectrum of MoO_2 NPs. Reprinted with permission from ref. 4. Copyright the Author(s) 2017.

Material	Shape (size)	Method	Peak wavelength	Group (year)
MoO_{3-x}	Crumpled (50 nm)	Hydrothermal (Water + EtOH)	550, 900 nm	Yamashita (2017)
MoO_{3-x}	Nano sheets (200 nm)	Hydrothermal (Water + EtOH/MeOH)	900 nm	Zhang (2016)
MoO_{3-x}	Nano sheets (200 nm)	Hydrothermal (Water + Alcohol)	550, 900 nm	Yamashita (2014)
MoO_{3-x}	Hallow sphere (300 nm)	Hydrothermal (EtOH) + Polyethylene glycol	< 800 nm (NO Peak)	Hu (2014)
MoO_{3-x}	Sheets (2 um)	Hydrothermal (Water + EtOH) + Oleylamine	850 nm	Wang (2012)
MoO_2	Dumbbells (200nm)	Hydrothermal (EtOH)	550nm	Xi (2017)

Figure 2.13 Synthetic methods of various plasmonic molybdenum oxides and their LSPR properties.[4,5,17-20]

MoO_2 and MoO_{3-x} NPs were synthesized by a simple pyrolysis of Mo precursor (MDBA) in a mixture of ODE and FA under a nitrogen atmosphere (Figure 2.14). Because MDBA has a decomposition temperature of 184 °C (which described in website of Sigma-Aldrich), molybdenum oxide is formed at 200 °C. FA ($C_{18}A$, $C_{10}A$, or C_8A) was used as a capping agent and reaction media. Table in Figure 2.15 summarizes sample numbers and the corresponding composition of FA and ODE in the reaction solution.
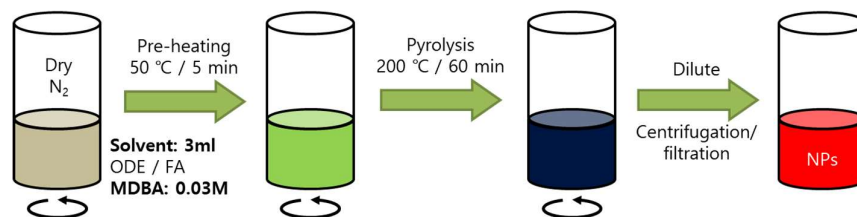

Figure 2.14 Schematic illustration of the synthetic process of MoO_2 and MoO_{3-x} NPs.

NP #	ODE (vol%)	C_nA (vol%)
#1	70	$C_{18}A$ (30%)
#2	70	$C_{10}A$ (30%)
#3	70	C_8A (30%)
#4	0	$C_{18}A$ (100%)
#5	50	C_8A (50%)
#6	30	C_8A (70%)
#7	0	C_8A (100%)

Figure 2.15 Summary of the composition of ODE and FA used in synthesis.

Figure 2.16a shows a photograph of toluene solutions of NPs #1−#7 left for ~24 h after the synthesis. As can be seen from the photograph, NP solutions showed various colors depending on the composition of reaction medium. Extinction spectra of the solutions are shown in Figure 2.16b and c. The color of the solution was derived from absorption peak in the visible region. Main extinction peaks of NPs #1−#5 are located at ~500 nm. Although smaller peaks also appeared at longer wavelengths in the spectra for NPs #1−#3 and #5, those were not observed in the spectrum of NP #4. Thus, NP #4, which was synthesized in $C_{18}A$, showed a vivid red color. NP #6 and #7 exhibited main extinction peaks at ~680 nm and 780 nm, respectively. The red color and the peak wavelength of NP #4 are clearly different from those of $MoO_{3−x}$ NPs, which are commonly known to show a blue color and an LSPR peak at 620−950 nm.[4,5,17-20] The peak wavelength at ~500 nm is rather close to that of MoO_2 NPs at 563 nm reported by Zhang *et al.*.[4]
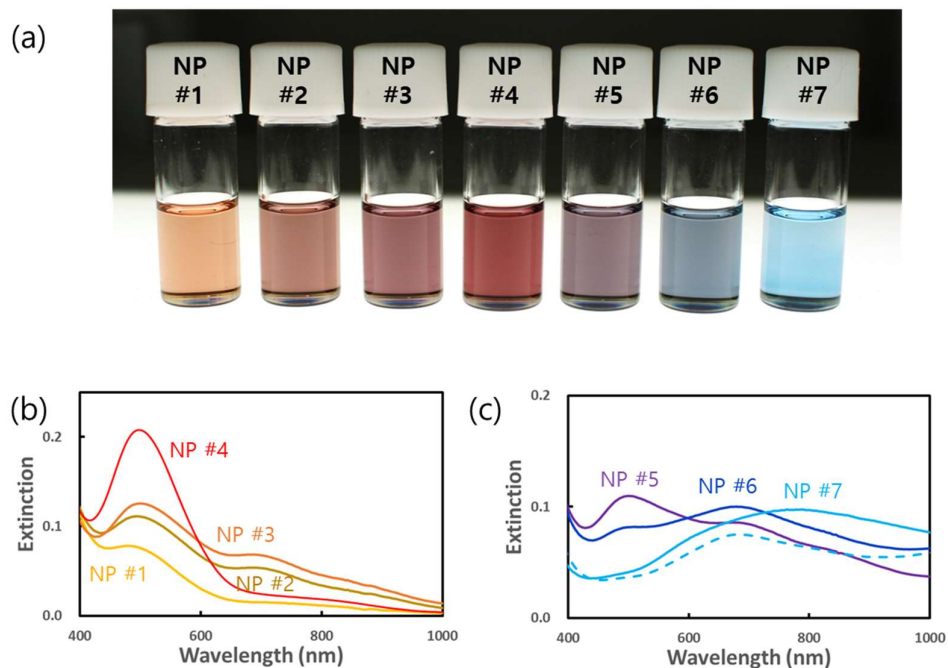
Figure 2.16 (a) Photograph of toluene solutions of MoO_2 and MoO_{3-x} NPs synthesized in non-aqueous media. Extinction spectra of (b) NP #1−#4 and (c) NP #5−#7 solutions diluted with toluene. Dashed and solid curves represent spectra for NP #7 right after purification and that left for ~24 h, respectively.

From the extinction spectra, NP #4 was assumed to be MoO_2 NPs. In order to confirm this, NP #4 was synthesized with a more careful purification process. After the preparation, the resulting solution (3 mL) was mixed with methanol (6 mL) and collected by centrifugation at $8500g$ for 10–15 min 2–4 times. The products were dried under reduced pressure for ~1 h and re-dispersed in a desired solvent (typically 2 mL toluene). Then the solution was filtered and diluted by 6-fold with toluene. The NP solution thus obtained (Figure. 2.17) was stable in toluene at room temperature for at least 2 weeks without any change in the optical spectrum and at 10 °C for at least several months. The NP #4 was drop cast on a commercially available ITO-coated glass substrate, and subjected to an XPS measurement. Commercially available MoO_3 was vapor-deposited onto another ITO-glass substrate and used for comparison. Figure 2.18a shows Mo 3d XPS spectra of the NPs (red line) and the vapor-deposited MoO_3 (black line). Only two characteristic

peaks were observed for MoO$_3$ at 232.7 eV and 235.8 eV, which were indexed to Mo^{6+}.[5,21] For NP #4, two characteristic peaks were observed exclusively at 230.8 eV and 234.1 eV, which were assigned to Mo^{4+} of MoO$_2$.[4,22] The XRD measurement was also conducted on a Si wafer for further characterization. As shown in Figure 2.18b (red line), small peaks corresponding to monoclinic MoO$_2$ crystal were observed, indicating that MoO$_2$ NPs were successfully synthesized by the present method. Mo^{6+} ions in MDBA are reduced to Mo^{4+} during the heating at 200 °C while acetylacetonates are oxidized.[23]
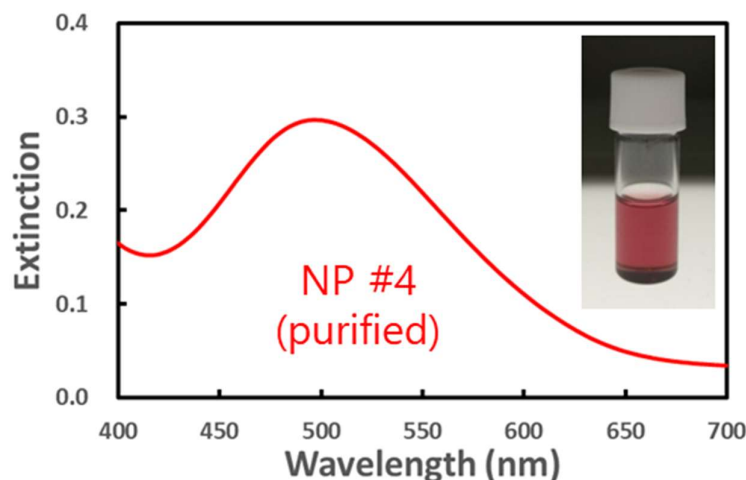

Figure 2.17 Extinction spectrum and photograph (inset) of a toluene solution of NP #4 after further purification.
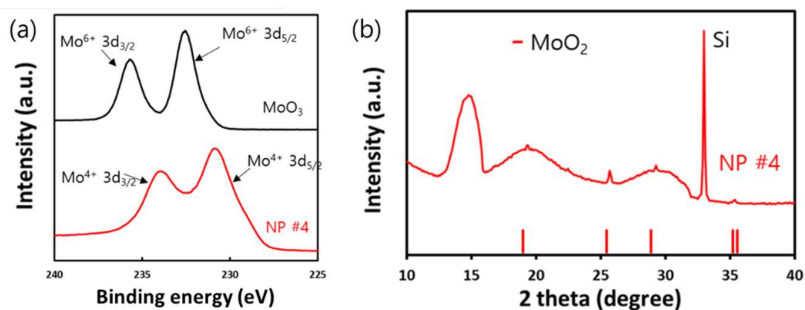
Figure 2.18 (a) Mo 3d XPS spectra of NP #4 and vapor-deposited MoO$_3$ on an ITO-coated glass substrate. (b) XRD pattern of NP #4 on a Si wafer.

A TEM image in Figure 2.19 indicates that NP #4 is very small (less than 5 nm) and featureless particle. In comparison with the previously reported dumbbell-shaped MoO_2 NPs,[4] the synthesized MoO_2 NPs exhibit the extinction peak at a shorter wavelength by ~70 nm and the full width at half maximum (FWHM) is narrower by more than twofold. This may be explained in terms of less anisotropic morphology and smaller size of NP #4. Generally, a LSPR peak redshifts and broadens as a plasmonic NP becomes more anisotropic.[24] On the basis of the extinction spectra, XPS, XRD, and TEM analysis, it was concluded that visible light-responsive plasmonic MoO_2 NPs were successfully synthesized by the present method.
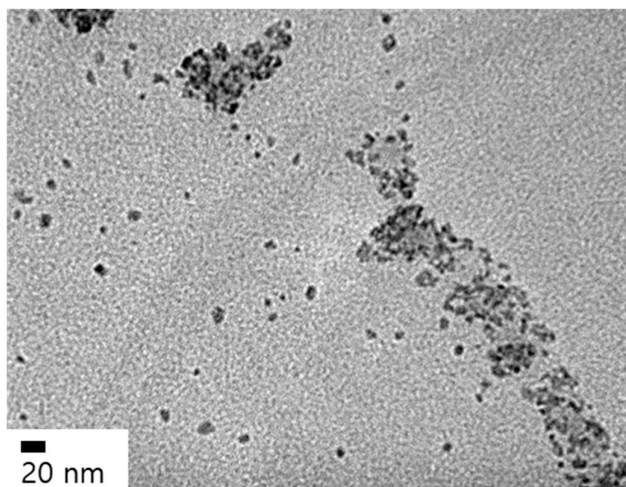

Figure 2.19 TEM image of further purified MoO_2 NPs (NP #4).

From the extinction spectra (Figure 2.16c), NP #7 was assumed to be MoO_{3-x} NPs.[4,5,17-20] In a similar manner to NP #4, NP #7 was prepared with a more careful purification process, followed by drop casting NP #7 on an ITO-coated glass substrate for XPS measurements. Figure 2.20a shows Mo 3d XPS spectra of the synthesized NP #7 (blue line) and the vapor deposited MoO_3 (black line). Mo 3d spectra of NP #7 (blue line) can be divided into four separated peaks which correspond to Mo^{6+} (232.7 eV and 235.8 eV)[5,21] and Mo^{5+} (231.7 eV and 234.9 eV).[5,21] The peak area of Mo^{6+} and Mo^{5+} is 91% and 9%,

respectively, indicating that the average oxidation state of NP #7 is 5.91, and it has mixed valance states caused by oxygen deficiency in NPs. XRD and TEM measurements were conducted for further characterization. As shown in Figure 2.20b (blue line), small peaks corresponding to typical orthorhombic MoO_3 crystal were observed. The TEM image indicates that the synthesized MoO_{3-x} NPs are also very small (~10 nm) and featureless particles (Figure 2.20c).

As-synthesized NP #7 showed a blue color and exhibited two peaks at ~700 and ~1000 nm (Figure 2.16c, dashed blue curve). However, the two extinction peaks were merged into a broad single peak at ~780 nm as the solution was left for ~24 h (Figure 2.16c, solid blue curve). It has been documented that MoO_{3-x} nanoplates exhibit a blue color and out-of-plane and in-plane LSPR modes at 600–700 and 900–1000 nm, respectively.[24] In addition, it has also been reported that these two peaks easily merge with each other to show a single broad peak.[25] Therefore, it was concluded that NP #7 is a MoO_{3-x} NP. The redshift and blueshift of the out-of-plane and in-plane mode peaks, which are responsible for the merging, suggest that the width/thickness aspect ratio of the plasmonic nanoplate decreases.[26] The decrease in the aspect ratio can be explained in terms of stacking of the MoO_{3-x} nanoplates.
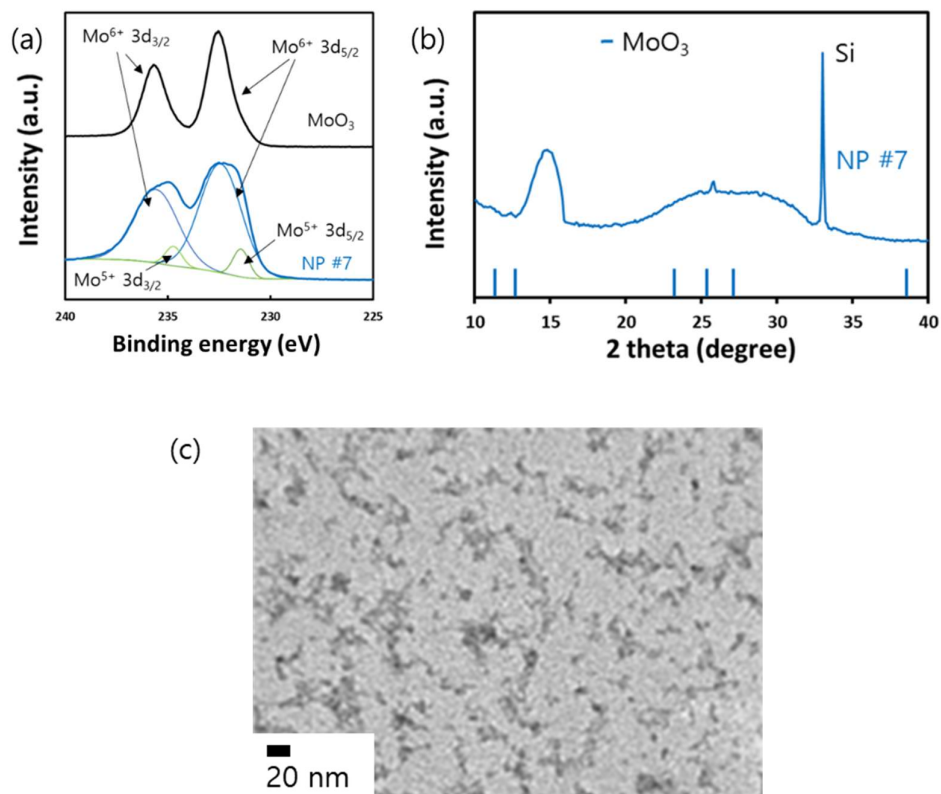
Figure 2.20 (a) Mo 3d XPS spectra of NP #7 and vapor-deposited MoO_3 on an ITO-coated glass substrate. (b) XRD pattern of NP #7 on a Si. (c) TEM image of NP #7.

As explained in 1.3, LSPR peak redshifts as the local refractive index increases and the shift of the wavelength is dependent linearly on the refractive index increase in the surrounding medium. Therefore, refractive index sensitivities of NP #4 (MoO_2), NP #3 (MoO_2 with shorter capping agents), and NP #7 (MoO_{3-x}) were evaluated. NPs were dispersed in solvents with different refractive index n, toluene ($n = 1.49$), chloroform ($n = 1.44$), cyclohexane ($n = 1.42$), tetrahydrofuran ($n = 1.40$), hexane ($n = 1.37$), and acetone ($n = 1.35$), and the peak wavelength was plotted against n. As can be seen from Figure 2.21, NP #3, #4, and #7 show linear relationships between the peak wavelength and n. The slopes of the plots are 260 nm RIU^{-1} (RIU: refractive index unit), 115 nm RIU^{-1}, and 17 nm RIU^{-1} for NP #7, #3, and #4, respectively. Higher sensitivity of NP #3 than that of #4 can be explained in terms of a thinner protecting layer (capping agent) around NP #3 (C_8A) in

comparison with that around NP #4 ($C_{18}A$). It is reasonable that free carrier oscillation of NPs with a thinner capping layer is more sensitive to the outer environment. MoO_{3-x} NPs, NP #7, show much higher refractive index sensitivity than that of MoO_2, indicating that the MoO_{3-x} NPs are more suitable for LSPR sensing such as affinity-based chemical sensing and biosensing described in 1.6.3.
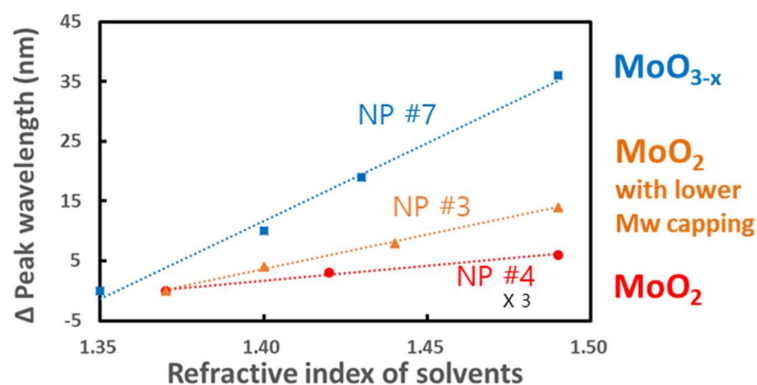
Figure 2.21 Responses of the extinction peak wavelength of NP #3, #4, and #7 to the refractive index of solvents.

The LSPR characteristics of MoO_2 NPs can be tuned by thermal treatments in an oxidizing or an inert atmosphere. MoO_2 NPs (NP #4) were drop cast on a glass substrate (Figure 2.22b, left figure) and the substrate was annealed at 300 °C for 3 h in air. The sample lost its plasmonic extinction peak (Figure 2.22a, red and black curves) and the corresponding red color. From the XPS spectrum (Figure 2.22c) and the SEM image (Figure 2.22d), it was found that small MoO_2 NPs transformed into larger MoO_3 nanoplates. In order to reduce the MoO_3 nanoplates, the substrate was annealed at 175 °C in vacuum for ~24 h. The extinction spectrum of the resultant sample (Figure 2.22a, blue curve) and the color (Figure 2.22b, right figure) were similar to those of NP #7 (Figure 2.16). Therefore, the MoO_3 nanoplates were most probably reduced to plasmonic MoO_{3-x} nanoplates.
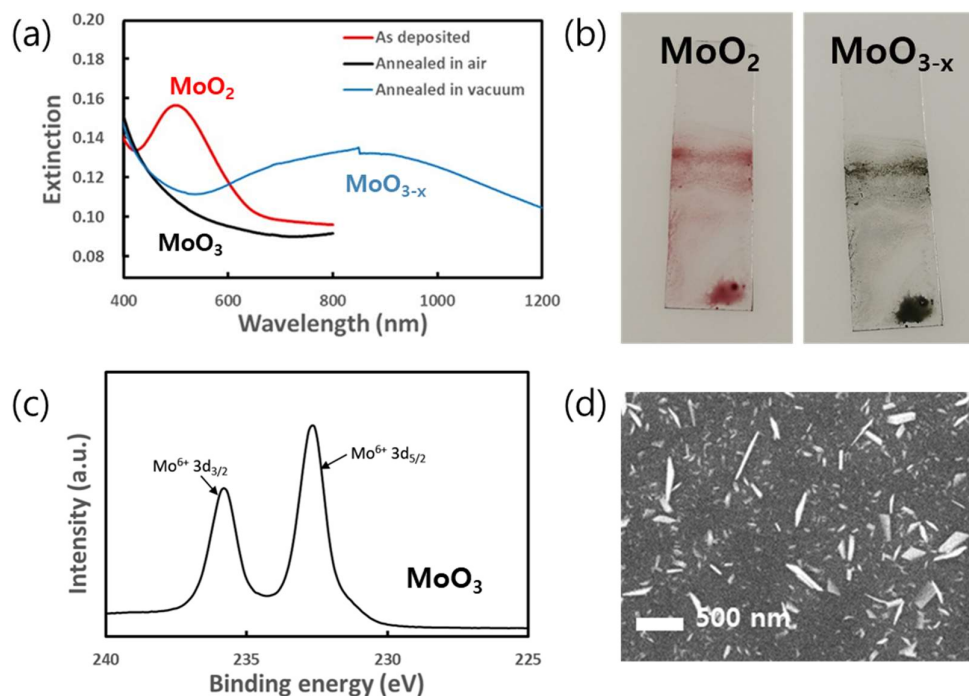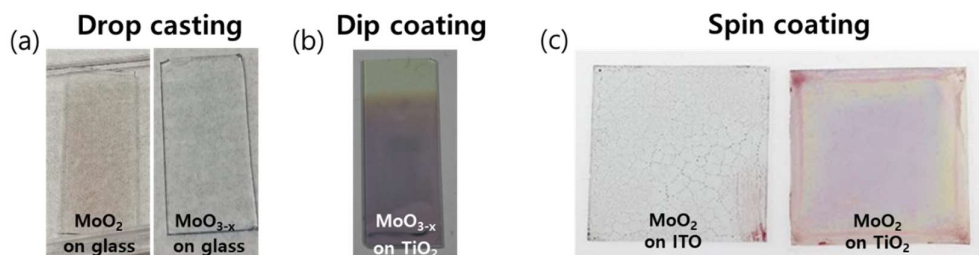
Figure 2.22 (a) Extinction spectra of MoO_2 NPs (NP #4) as-deposited on a glass substrate (red curve), after annealing at 300 °C in air for 3 h (black curve), and after annealing at 175 °C in vacuum for 24 h (blue curve). (b) Photographs of MoO_2 NPs and MoO_{3-x} on a glass substrate. (c) XPS spectrum and (d) SEM image of MoO_3 nanoplates formed after annealing of MoO_2 NPs.
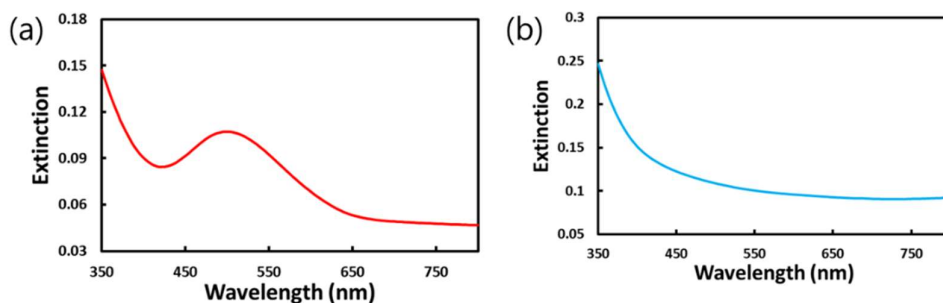
2.3.5 Fabrication of plasmonic MoO_{3-x} nanostructure

In the previous section, plasmonic MoO_2 and MoO_{3-x} NPs were successfully synthesized by a non-aqueous synthetic method. Although the synthesized MoO_2 and MoO_{3-x} NPs are suitable for PICS applications because they absorb visible light, it was found that the NPs have a problem with coating processes, which is necessary to fabricate a PICS-based photoelectrochemical cell. As shown in Figure 2.23, the conventional coating methods such as drop casting, dip coating, and spin coating did not yield uniform NP layer with sufficient thickness on any substrate. Even if the NPs are successfully deposited on the substrate, removing the organic capping agents around the NPs is also difficult because plasmonic MoO_2 and MoO_{3-x} NPs are oxidized easily into non-plasmonic MoO_3 by a

ligand exchange, a O_2 plasma treatment (Figure 2.24), or a heat treatment. Therefore, a plasmonic MoO_{3-x} nanostructure was fabricated by vapor deposition of MoO_3 onto NP ensembles as templates without using capping agent.


Figure 2.23 Photographs of MoO_2 and MoO_{3-x} NP layers coated on glass, ITO, and TiO_2 substrates by (a) drop casting, (b) dip coating, and (c) spin coating.

Figure 2.24 Extinction spectra of MoO_2 NPs deposited on glass (a) before and (b) after removing capping agents by a O_2 plasma treatment (100 W for 15 min).

The fabrication process of plasmonic MoO_{3-x} nanostructures is shown in Figure 2.25. ITO NPs (10 mol% Sn, ~10 nm in size) were spin-coated on a glass substrate and used as the template (Figure 2.26b, left). Surface coverage of the ITO NP ensemble was ~57% when a 0.20 wt% NP suspension was used (Figure 2.26a). After deposition of a 30-nm-thick MoO_3 layer onto the substrate, the substrate shows a clear blue color (Figure 2.26b, right), whereas the layer deposited directly on a glass substrate (without ITO NP

ensemble) exhibits a hazy ochre color (Figure 2.26b, center). These results suggest that a plasmonic MoO_{3-x} nanostructure was formed in the NP template.
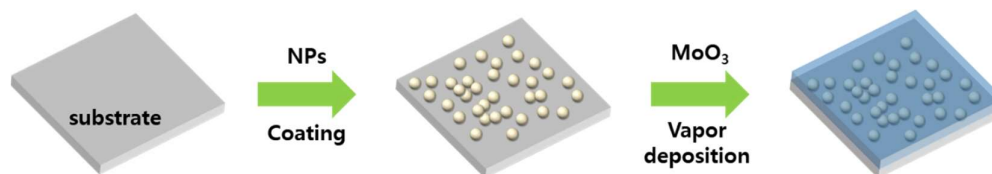
Figure 2.25 Schematic illustration of the fabrication process MoO_{3-x} nanostructures.
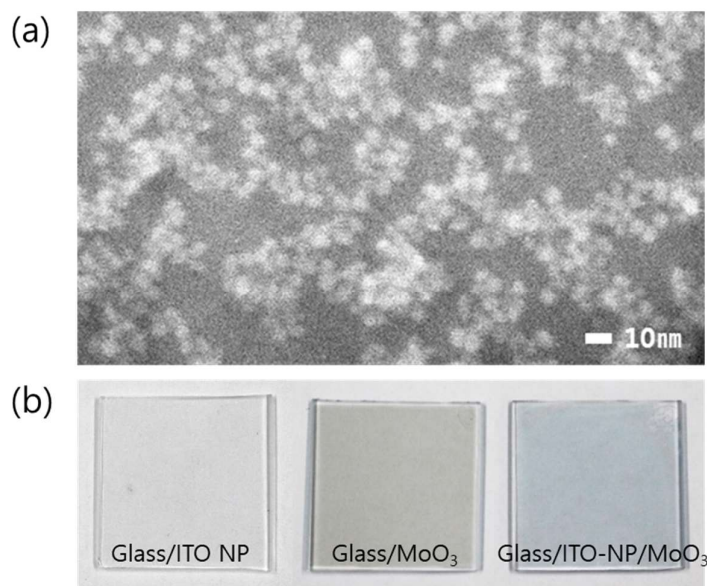
Figure 2.26 (a) SEM image of an ITO NP ensemble. The NPs were deposited on a conductive ITO electrode for SEM observation. (b) Photograph of glass/ITO-NP, glass/MoO_3, and glass/ITO-NP/MoO_3 samples.

In order to investigate the reason for the blue color, ITO NP templates with different surface coverage were fabricated from 0.04-0.20 wt% suspensions and MoO_3 layer (30 nm) was deposited on to the substrates. As shown in Figure 2.27a, absorption spectrum of each substrate exhibits two absorption peaks at ~850 nm and ~2000 nm. The

former peak tails to ~400 nm and is responsible for the blue color of the samples. The latter absorption peak at ~2000 nm is ascribed to the intrinsic LSPR of the ITO NPs because ITO NPs of this size and composition are known to show LSPR at 1600−2000 nm (Figure 2.3). Actually, ITO NPs on a glass without MoO_3 layers exhibited an LSPR peak at ~2000 nm (Figure 2.27b, blue curve). As the NP concentration in the suspension was increased, the surface coverage of the NPs became higher, and the peak intensity at ~2000 nm increased monotonically. The absorption intensity of the former peak at ~850 nm is, however, almost saturated when the suspension concentration is ≥0.14 wt%. This suggests that the peak is not simply ascribed to the ITO NPs. The wavelength is actually too short to assign to ITO LSPR. The peak at ~850 nm was not observed for ITO NP template without MoO_3 layer (Figure 2.27b, blue curve) and very small for a MoO_3 layer without ITO NPs (Figure 2.27b, ochre curve). Therefore, both the NP template and the MoO_3 coating are necessary for the peak at ~850 nm to occur.
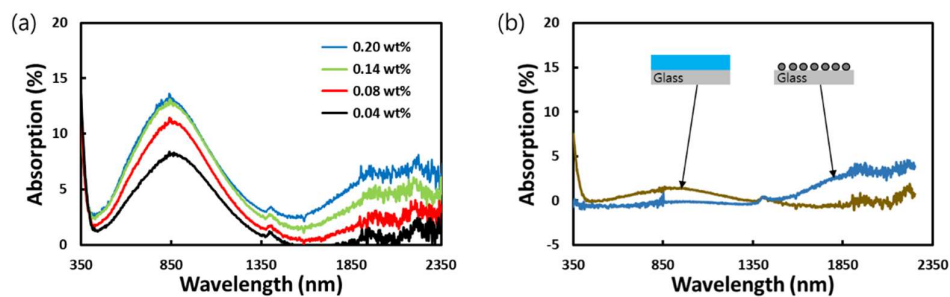
Figure 2.27 Absorption spectra of (a) glass/ITO-NP/MoO_3 samples with different coverage of ITO NPs prepared form 0.04-0.20 wt% ITO NPs suspensions and (b) glass/ITO-NP sample prepared form a 0.02 wt% ITO NPs suspension and glass/MoO_3 sample.

For that reason, the opposite structure was examined, which was prepared by deposition of a 30-nm-thick MoO_3 layer directly onto a glass plate without ITO NPs, followed by spin-coating of the ITO NPs (0.20 wt%) onto the MoO_3 layer. Enhancement of absorption was observed at ~850 nm with this structure (Figure 2.28) and its spectrum was close to the sum of the spectrum of the ITO NPs (Figure 2.27b, blue curve) and that of the

MoO$_3$ layer (Figure 2.27b, ochre curve). This indicates that the absorption at ~850 nm is not due to ITO NPs in simple contact with MoO$_3$, but due to the MoO$_3$ layer with embedded ITO NP ensemble. It is, therefore, assumed that the ITO NP ensemble serves as a nanotemplate that gives a nanostructured interface. Actually, the absorption peak at ~850 nm is very close to the LSPR peak of plasmonic MoO$_{3-x}$ NPs (Figure 2.16).
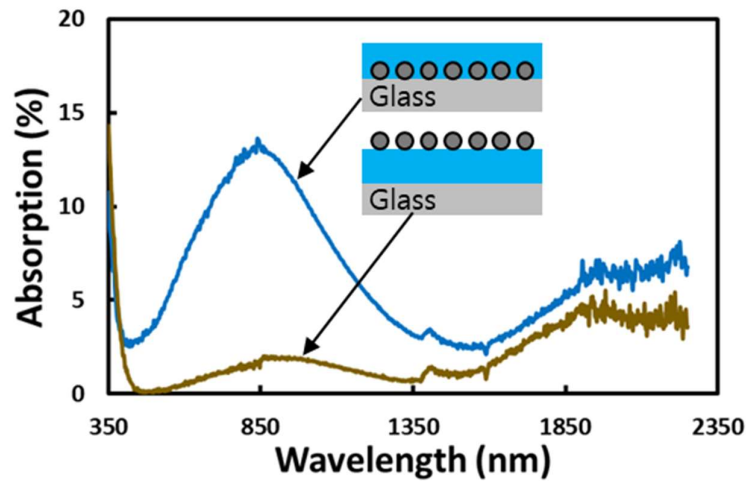
Figure 2.28 Absorption spectra of the glass/ITO-NP/MoO$_3$ and glass/MoO$_3$/ITO-NP samples.

Next, optical response of the nanostructure to refractive index change was investigated as is the case for MoO$_2$ and MoO$_3$ NPs (Figure 2.21). An ITO nanotemplate was fabricated on a TiO$_2$-coated glass plate, followed by coating with a 50-nm-thick MoO$_3$ layer. As can be seen from Figure 2.29, the absorption peak of the MoO$_3$ layer with embedded ITO NPs was redshifted (~20 nm) on TiO$_2$ ($n = 2.5$ at 850 nm) compared with that on glass ($n = 1.5$ at 850 nm). Although the refractive index change is small since the nanostructure is mostly covered with MoO$_3$ itself ($n = 2.4$) and in contact with TiO$_2$ or glass only in part, the dependence on the local refractive index indicates that the peak is most likely because of LSPR.
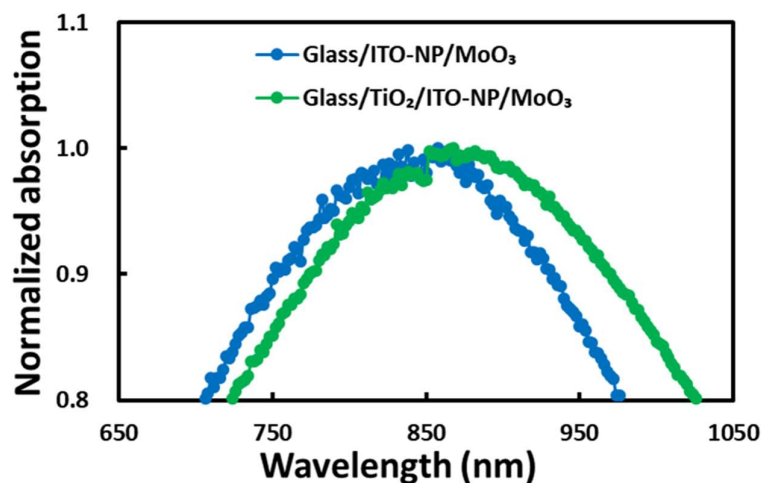
Figure 2.29 Magnified spectra of the glass/ITO-NP/MoO$_3$ and glass/TiO$_2$/ITO-NP/MoO$_3$ samples.

If the morphology of the ITO NP ensemble is the most important factor for nanostructured MoO$_3$, other NPs with similar morphologies may also serve as templates. Thus, the ITO NPs were replaced with other NPs: (1) less conductive ITO NPs (5 and 3 mol% Sn), (2) non-conductive In$_2$O$_3$ NPs, or (3) metallic Au and Pt NPs. The diameter of all those NPs was fixed to ~10 nm. Although the ITO and Au NPs exhibited their LSPR at 1900 nm and 540 nm, respectively, no appreciable absorption was observed in the 540–1400 nm range. The In$_2$O$_3$ and Pt NPs showed no significant absorption in the whole visible and NIR ranges examined. These NPs were deposited on a glass substrate and coated with 50-nm-thick MoO$_3$ by thermal vapor deposition. Remarkably, all the prepared samples showed a similar absorption peak at ~850 nm, even though there were some differences in the peak height (Figure 2.30). On the basis of the results that the NPs with different compositions and different capping agents exhibit similar effects on the MoO$_3$ film, it was concluded that the NP morphology is the most important factor for the absorption of nanostructured MoO$_3$ at ~850 nm.
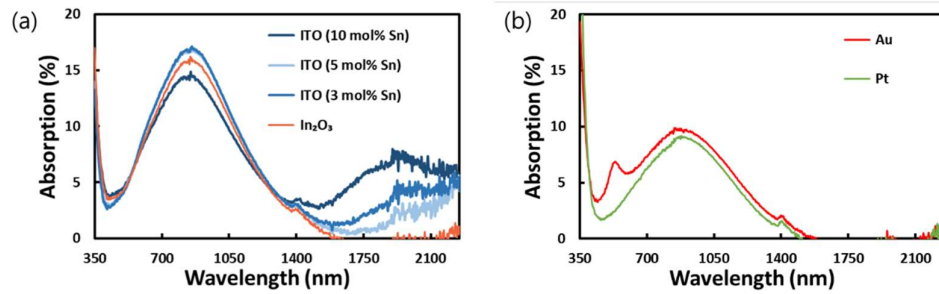
Figure 2.30 Absorption spectra of glass/NP/MoO₃ samples, where NP is (a) ITO (10, 5, or 3 mol% Sn) and In₂O₃ NP and (b) Au and Pt NP.

As described in 2.3.4, fully oxidized MoO_3 NPs are not plasmonic whereas partially reduced MoO_{3-x} NPs exhibit LSPR in the NIR range. Therefore, redox state of nanostructured MoO_3 was investigated to understand the mechanism further. XPS analysis was conducted using nanostructured and non-structured samples with and without ITO NPs (10 mol% Sn), respectively. As seen in Figure 2.31a, only two characteristics peaks corresponding to Mo^{6+} (232.7 eV and 235.8 eV)[5,21] were observed for the non-structured MoO_3 layer (ochre curve). However, in the case of the nanostructured MoO_3 layer, the presence of a small amount of Mo^{5+} (231.7 eV and 234.9 eV)[5,21] was observed at the top of the MoO_3 layer (gray curve). In order to measure the redox state of nanostructured layer at the interface between MoO_3 and the substrate, MoO_3 layer was peeled off from the substrate using a conductive copper tape and the tape with MoO_3 was used as the XPS sample. The increased proportion of Mo^{5+} (blue curve) was detected and peaks derived from ITO were also observed (Figure 2.31b). Therefore, it was concluded that the plasmonic absorption observed at ~850 nm was due to reduced nanostructured MoO_{3-x}.
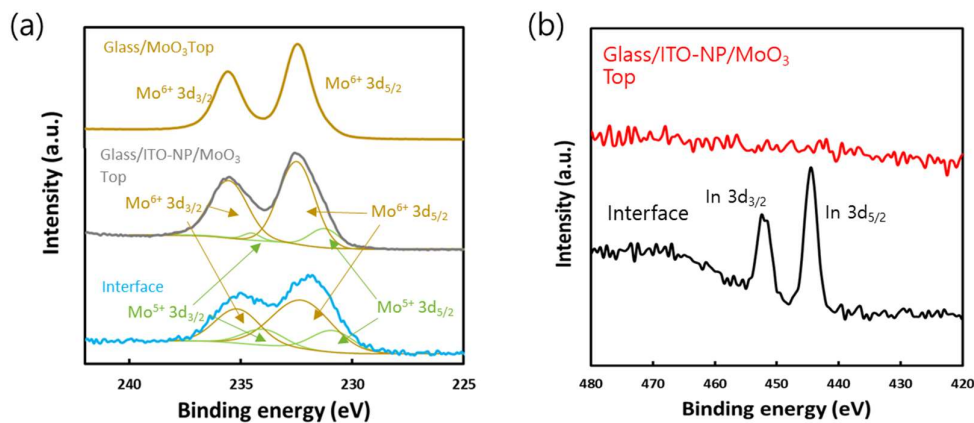
Figure 2.31 (a) Mo 3d XPS spectra of glass/MoO$_3$ (top) and glass/ITO-NP/MoO$_3$ samples (top and the interfacial region). (b) In 3d XPS spectra of a glass/ITO-NP/MoO$_3$ sample (top and the interfacial region).

The effect of nanotemplate can be explained in part by the structure zone model.[27] For vapor deposition of a material onto a solid surface a temperature less than $0.3T_m$ (K), where T_m is melting point of the deposited material, the deposited atoms are poorly mobile. Therefore, the layer deposited on the ITO NPs should keep the particulate the morphology in the initial phase of deposition. The large surface area and structural distortions of the deposited layer could lead to dissipation of some oxygen and generation of oxygen defects, most probably, which results in the formation of nanostructured MoO$_{3-x}$. The roughness of the top surface of the deposited layer gradually decreases during further MoO$_3$ deposition and the Mo^{5+} concentration decreases.

2.4 Conclusions

In this chapter, new synthetic methods of ITO, MoO$_2$, and MoO$_3$ NPs were developed and the obtained NPs were characterized in detail. Particle size, doping ratio (LSPR wavelength), length of the capping agent, and doping distribution in the ITO NPs were successfully controlled by a reverse hot injection method. Plasmonic MoO$_2$ and MoO$_{3-x}$ NPs were synthesized by a simple pyrolysis of MDBA in non-aqueous media for

the first time and it was found that their LSPR properties were tunable by the reaction condition and heat treatment in an oxidizing atmosphere or in vacuum. In addition, plasmonic MoO_{3-x} nanostructures were fabricated on NP ensembles as the templates to overcome the drawbacks of colloidal MoO_2 and MoO_{3-x} NPs for PICS applications. Nanostructured MoO_{3-x} exhibit LSPR peak at ~850 nm as is the case for MoO_{3-x} NPs. In Chapter 3 and Chapter 4, prepared nanostructured MoO_{3-x} and ITO NPs are used for PICS applications.

2.5 References

1   H. Nishi and T. Tatsuma, *J. Phys. Chem. C*, 2018, **122**, 2330–2335.

2   Y. Katagi, E. Kazuma, and T. Tatsuma, *Nanoscale*, 2014, **6**, 14543–14548.

3   A. Agrawal, S. H. Cho, O. Zandi, S. Ghosh, R. W. Johns, and D. J. Milliron, *Chem. Rev.*, 2018, **118**, 3121–3207.

4   Q. Zhang, X. Li, Q. Ma, Q. Zhang, H. Bai, W. Yi, J. Liu, J. Han, and G. Xi, *Nat. Commun.*, 2017, **8**, 14903.

5   H. Cheng, T. Kamegawa, K. Mori, and H. Yamashita, *Angew. Chem. Int. Ed.*, 2014, **53**, 2910–2914.

6   M. Kanehara, H. Koike, T. Yoshinaga, and T. Teranishi, *J. Am. Chem. Soc.*, 2009, **131**, 17736–17737.

7   G. Garcia, R. Buonsanti, E. L. Runnerstrom, R. J. Mendelsberg, A. Llordes, A. Anders, T. J. Richardson, and D. J. Milliron, *Nano Lett.*, 2011, **11**, 4415–4420.

8   R. Glass, M. M ller, and J. P. Spatz, *Nanotechnology*, 2003, **14**, 1153–1160.

9   K. C. Kao, Y. Kuroiwa, H. Nishi, and T. Tatsuma, *Phys. Chem. Chem. Phys.*, 2017, **19**, 31429–31435.

10   F. Yang, W. Kubo, N. Sakai, and T. Tatsuma, *Electrochemistry*, 2010, **78**, 161–164.

11   Y. Takahashi and T. Tatsuma, *Nanoscale*, 2010, **2**, 1494–1499.

12   S. D. Lounis, E. L. Runnerstrom, A. Llordés, and D. J. Milliron, *J. Phys. Chem. Lett.*, 2014, **5**, 1564–1574.

13   A. W. Jansons and J. E. Hutchison, *ACS Nano*, 2016, **10**, 6942–6951.

14   I. Lokteva, N. Radychev, F. Witt, H. Borchert, J. Parisi, and J. Kolny-Olesiak, *J. Phys. Chem. C*, 2010, **114**, 12784–12791.

15   S. D. Lounis, E. L. Runnerstrom, A. Bergerud, D. Nordlund, and D. J. Milliron, *J. Am. Chem. Soc.*, 2014, **136**, 7110–7116.

16   C. Zhu, Q. Xu, L. Ji, Y. Ren, and M. Fang, *Chem. Asian J.*, 2017, **12**, 2980–2984.

17   X. Tan, L. Wang, C. Cheng, X. Yan, B. Shen, and J. Zhang, *Chem. Commun.*, 2016, **52**, 2893–2896.

18   H. Yin, Y. Kuwahara, K. Mori, H. Cheng, M. Wen, and H. Yamashita, *J. Mater. Chem. A*, 2017, **5**, 8946–8953.

19   G. Song, J. Shen, F. Jiang, R. Hu, W. Li, L. An, R. Zou, Z. Chen, Z. Qin, and J. Hu, *ACS Appl. Mater. Interfaces*, 2014, **6**, 3915–3922.

20   Q. Huang, S. Hu, J. Zhuang and X. Wang, *Chem. Eur. J.*, 2012, **18**, 15283–15287.

21   T. S. Sian and G. B. Reddy, *Sol. Energy Mater. Sol. Cells*, 2004, **82**, 375–386.

22   Z. Song, T. Cai, Z. Chang, G. Liu, J. A. Rodriguez, and J. Hrbek, *J. Am. Chem. Soc.*, 2003, **125**, 8059–8066.

23   R. N. Nenashev, N. E. Mordvinova, V. P. Zlomanov, and V. L. Kuznetsov, *Inorg. Mater.*,

2015, **51**, 891–896.

24   J. Zeng, S. Roberts, and Y. Xia, *Chem. Eur. J.*, 2010, **16**, 12559–12563.

25   M. M. Y. A. Alsaif, M. R. Field, T. Daeneke, A. F. Chrimes, W. Zhang, B. J. Carey, K. J. Berean, S. Walia, J. Van Embden, B. Zhang, K. Latham, K. Kalantar-zadeh, and J. Z. Ou, *ACS Appl. Mater. Interfaces*, 2016, **8**, 3482–3493.

26   S. W. Hsu, W. Bryks, and A. R. Tao, *Chem. Mater.*, 2012, **24**, 3765–3771.

27   K. Bordo and H. G. Rubahn, *Mater. Sci. Medzg.*, 2012, **18**, 313–317.

Chapter 3

Infrared PICS based on hole injection from nanostructured MoO_{3-x}

3.1 Introduction

As discussed in Chapter 1, trapped energy by LSPR could be converted into electron movement at the interface between a semiconductor and a plasmonic nanomaterial by PICS. However, noble metal nanostructures have been employed as plasmonic nanomaterials, even though there have been many reports on plasmonic compound nanomaterials recently.

To achieve PICS with compound nanomaterials for the first time, the nanostructured MoO_{3-x} developed in Chapter 2 was selected in this chapter, because it exhibits relatively high LSPR energy (~1.4 eV, corresponding to ~850 nm) and the interface between the nanostructured MoO_{3-x} and a substrate is free from an organic matter. A solid cell system was adopted for this study. Solid cell systems have relatively low cell resistance compared to wet cell systems and therefore exhibit an excellent resolution for small response signals. Further, there is no need to select a solvent in which the operating nanostructure is stable. There have been two types of PICS-based solid-state cells. The first one involves plasmonic nanomaterials that are in contact with both n-type and p-type semiconductors (*e.g.*, ITO|n-SC|PL|p-SC|Au, where SC is semiconductor and PL is a plasmonic material).[1-3] In the second one, which has a simpler structure, the p-type semiconductor is omitted (*e.g.*, ITO|PL|n-SC|In).[4-6]

In this chapter, the nanostructured MoO_{3-x} in contact with TiO_2 is used for the development of the ITO|TiO_2|PL|MoO_3|Ag cell, in which TiO_2 and MoO_3 work as n-type semiconductor and p-type semiconductor, respectively. The compound PICS was investigated under NIR irradiation (700-1400 nm). Also, the prepared cell was improved in terms of the photocurrent density. Compound PICS was achieved for the first time and it was found to be based on hole injection from the plasmonic MoO_{3-x} nanostructure to TiO_2.

3.2 Experimental

3.2.1 Fabrication of solid-state cells

An ITO film coated on a glass plate (23 x 23 mm) was etched into an electrode (6 x 23 mm) by aqua regia (Figure 3.1a). The patterned ITO substrate was sonicated in acetone, Milli-Q water, and 2-propanol. The cleaned ITO substrate was coated with a ~60-nm-thick TiO$_2$ layer (17 x 23 mm) by a spray pyrolysis method[7] through a glass mask (Figure 3.1b). The ITO (10, 5, and 3 mol% Sn) or In$_2$O$_3$ NPs were coated on the substrate by spin-coating (2000 rpm for 30 s) from a 0.20 wt% NP suspension to form a nanotemplate layer. After that, NPs were removed by ethanol-soaked cotton buds from the edge regions of the substrate (~3 mm) (Figure 3.1c). The prepared nanotemplate was dried in a vacuum chamber for 12 h. The dried samples were subjected to ligand exchange (1 M formic acid in acetonitrile for 45 min)[8] followed by vacuum drying for 12 h. The prepared sample was moved to an evaporation chamber with a patterned mask and MoO$_3$ was evaporated (12 x 12 mm, ~50 nm thick) at the rate of 0.03 nm s^{-1} (Figure 3.1d). By using another mask for the back electrode (Figure 3.1e), Ag (~70 nm thick) was evaporated at the rate of 0.3 nm s^{-1}. Each prepared substrate has 4 photovoltaic cells with the cell size of ~2 x 2 mm.
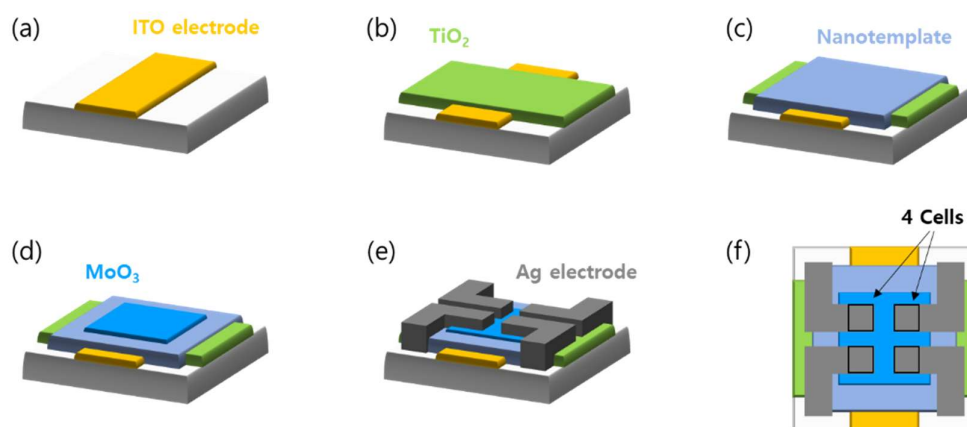
Figure 3.1 (a) Etched ITO-film coated glass. (b) TiO$_2$ layer prepared on ITO electrode. (c) NP layer spin-coated on TiO$_2$ followed by edge removal. (d) MoO$_3$ evaporated through a patterned mask. (e) Ag evaporated through a patterned mask. (f) 4 solid-state cells on one substrate.

3.2.2 Characterization

The structure of photovoltaic cells was investigated by scanning electron microscopy (SEM) using a JSM-7500FA (JEOL). Optical spectra were measured using a Jasco V-670 UV-vis-NIR spectrophotometer with an integrating sphere. Short-circuit photocurrent measurements were carried out with a potentiostat (SI 1285A, Solartron) under visible and NIR light irradiation (500–1600 nm, full width at half maximum ~50 nm (500-900 nm) and ~100 nm (1000-1600 nm), HA-150UX, Myutron, 8.6×10^{14} photons cm^{-2} s^{-1}).

3.3 Results & discussion

3.3.1 Solid-state cell characterization

The cells were prepared with ITO (10 mol% Sn) nanotemplate on a TiO_2-coated ITO electrode and further coated with MoO_3. ITO NP ensemble as a nanotemplate is shown was observed by SEM (Figure 3.2a). The surface coverage was ~57%. Some multi-stacking regions with aggregated ITO NPs were found on TiO_2.

Preventing short circuiting during photovoltaic fabrication is one of the most important parts. In the present system, MoO_3 is served not only as a light absorbing layer but also for a short circuit prevention between the TiO_2 or ITO layer and the Ag electrode. However, the series resistance of the cell increases with increasing thickness of the MoO_3 film, which has very high resistivity (10^{10} Ω cm)[9] in comparison with ITO (10^{-4} Ω cm).[10] From those viewpoints, the cell with 40-nm-thick MoO_3 layer and that with 50-nm-thick MoO_3 layer was prepared.
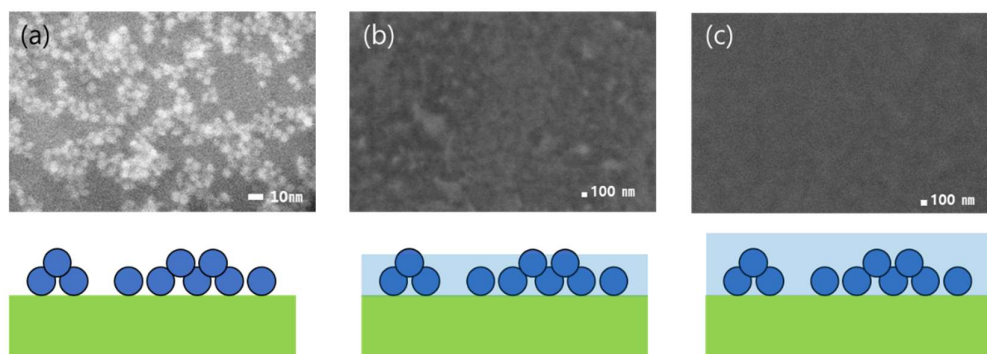
Figure 3.2 SEM images with cross-sectional illustrations of (a) ITO nanotemplate with surface coverage ~57%, (b) that after evaporation of MoO_3 with a thickness of 40 nm on ITO nanotemplate, and (c) that after evaporation of MoO_3 with a thickness of 50 nm on ITO nanotemplate.

After coating with 40-nm-thick MoO_3 layer (Figure 3.2b), it was observed that the morphology of the ITO nanotemplate remained intact. Therefore, this layer is not thick enough to prevent short-circuiting. However, after increase of the thickness to 50 nm, the ITO nanotemplate was not observed, indicating that it was well covered by MoO_3. So, the 50-nm-thick MoO_3 layer was adopted for the assemble of the cell.

On the top of the MoO_3 layer, an Ag electrode was evaporated through the mask. For confirmation of the overall structure of the cells, the cross-sectional SEM image of the cell was obtained (Figure 3.3). As can be seen in Figure 3.3a, the cells ITO|TiO_2|ITO nanotemplate|MoO_3|Ag cell (10 mol% Sn for ITO NPs) was successfully prepared on ITO electrode. In addition, it is further confirmed that ITO NPs are located at the interface between TiO_2 and MoO_3 (Figure 3.3b).
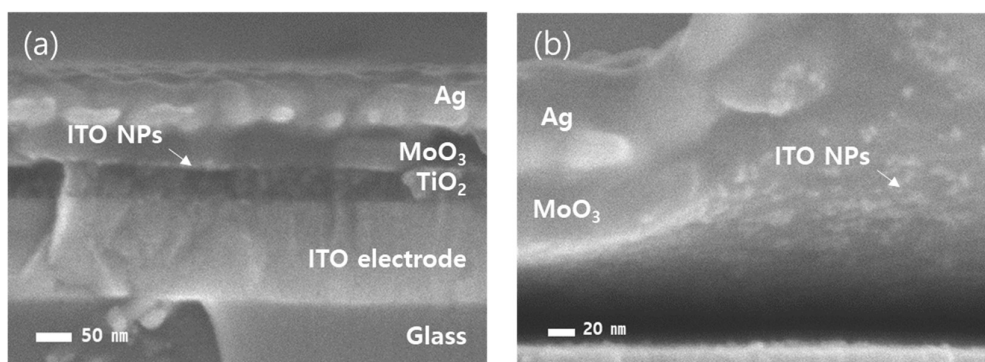
Figure 3.3 (a) Cross-sectional SEM image of the ITO|TiO$_2$|ITO nanotemplate|MoO$_3$|Ag cell (10 mol% Sn for ITO NPs) and (b) ITO NPs at the interface of TiO$_2$ and MoO$_3$.

In the same manner, a solid-state cell without the nanotemplate (ITO|TiO$_2$|MoO$_3$|Ag) was fabricated for comparison of optical characteristics of the cells. Absorption spectra were obtained for the cells before deposition of the Ag electrode. As can be seen in Figure 3.4, it was found that the nanostructured MoO$_3$ was formed well in the solid cell as well as that on a glass substrate, and it was confirmed that there was no significant absorption in the range of 500-1400 nm for the cell without the ITO nanotemplate.
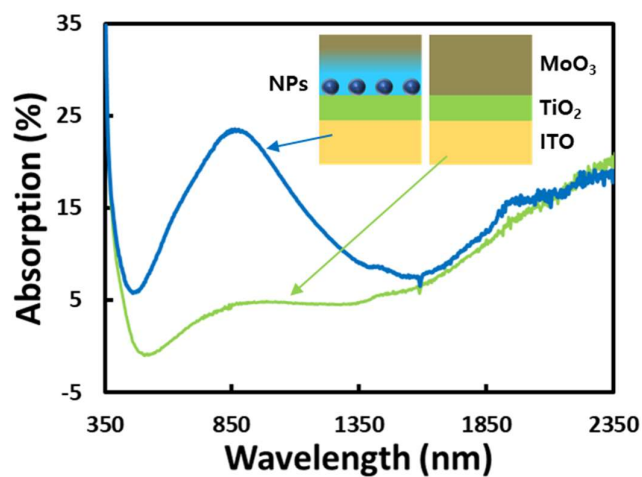
Figure 3.4 Absorption spectra of the prepared cells without the Ag electrode; ITO|TiO$_2$|ITO nanotemplate|MoO$_3$ (blue) and ITO|TiO$_2$|MoO$_3$ (green).

3.3.2 Origin of photocurrent response of photovoltaic cells

To investigate the photovoltaic properties, cells were prepared by using ITO NPs with different Sn content (0, 3, and 10 mol%. 0 mol% corresponds to In_2O_3 NPs) as illustrated in Figure 3.5a. For the detailed study about NIR responses of the cells, photocurrents were measured under NIR light of different wavelengths (700−1600 nm) through band-pass filters and plotted the incident photon-to-current conversion efficiency (IPCE) as a function of the wavelength. As can be seen in Figure 3.5b, all those cells exhibited positive photocurrents (current flow from the Ag electrode to the ITO electrode within the cell). Also, the maximum value of the IPCE increased without peak shift as the mol ratio of Sn to In in the NPs decreased. This indicates that if the NPs in the nanotemplate is conducting (*e.g.*, ITO NPs), those may act as recombination centers and suppress the photocurrent flow.
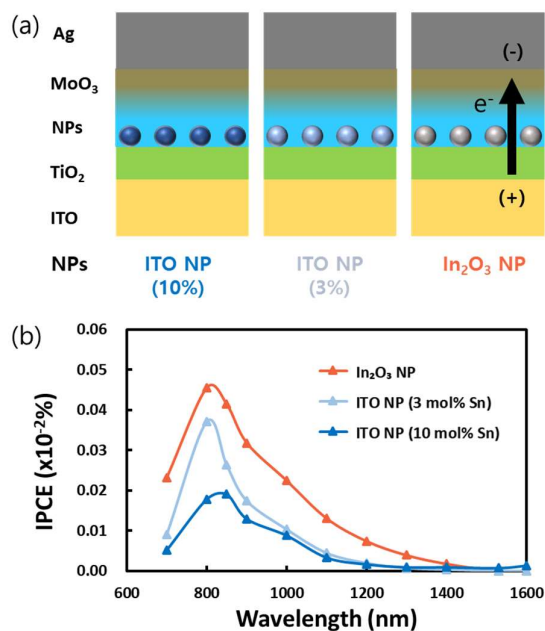
Figure 3.5 (a) Illustration of the cell structures and (b) IPCE action spectra of ITO|TiO_2|nanotemplate|MoO_3|Ag cells, where nanotemplate consists of ITO (10 or 3 mol% Sn) or In_2O_3 NPs.

To compare with the cell with an In_2O_3 nanotemplate, the cell without the nanotemplate ($ITO|TiO_2|MoO_3|Ag$) and the cell without TiO_2 ($ITO|NP|MoO_3|Ag$) were also prepared (Figure 3.6a) and subjected to measurements of photocurrent action spectra. The IPCE action spectra of those cells were measured under 500−1400 nm light irradiation. As can be seen in Figure 3.6b, although the cell without the nanotemplate also showed the positive photoresponse in the NIR range, the currents were ~5-fold lower than those of the cell with the In_2O_3 nanotemplate. The small photocurrents of the cell without the nanotemplate are explained in terms of the low absorption at the ~850 nm peak (Figure 3.4 green curve), which is due to small roughness scale of the bare TiO_2 surface (a few nanometers at most) in comparison with that at the nanotemplate surface (~10 nm). Under visible light (500−600 nm), the cell with the In_2O_3 nanotemplate exhibited negative photocurrents, and the cell without the nanotemplate showed larger negative photocurrents. The cell without the TiO_2 layer exhibited negligible photocurrent responses in the whole wavelength range examined. On the basis of these results, it was concluded that the TiO_2/MoO_3 interface is the most important for the photoresponses among the interfaces involved in the cell. In particular, the TiO_2/MoO_{3-x} interface with the NPs must be important for the positive photocurrents.
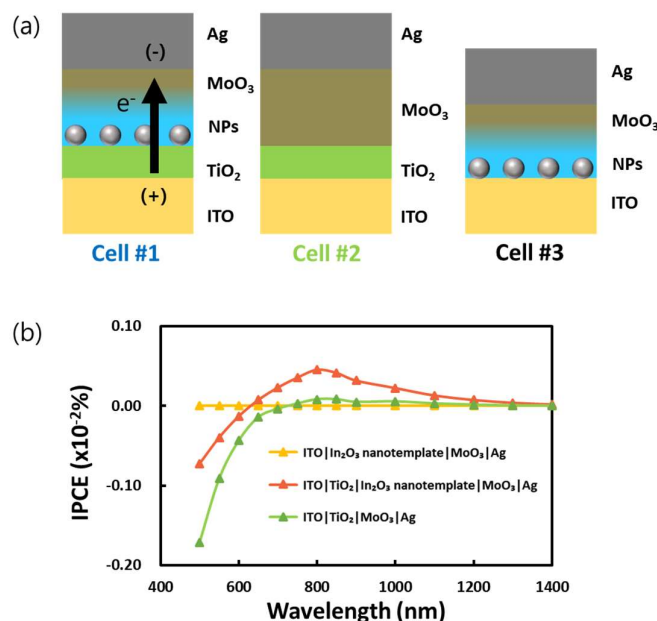
Figure 3.6 (a) Illustration of the prepared cell with different structures and (b) IPCE action sepctra of ITO|TiO$_2$|ITO nanotemplate|MoO$_3$|Ag cell, ITO|TiO$_2$|MoO$_3$|Ag cell, and ITO|In$_2$O$_3$ nanotemplate|MoO$_3$|Ag cell.

3.3.3 Mechanism of photovoltaic responses

As discussed above, the cell with the nanostructured MoO$_{3-x}$ (*i.e.*, the cell with a nanotemplate, ITO|TiO$_2$|nanotemplate|MoO$_3$|Ag cell) on a TiO$_2$ exhibit photocurrent and photovoltage responses under NIR irradiation (650-1400 nm). The current densities were inversely related to the conductivity of NPs. The peak shape and position of the IPCE action spectrum coincided with those of the LSPR absorption of the nanostructured MoO$_{3-x}$. On the basis of these results, it is reasonable to conclude that the charge separation under NIR light occurs at the TiO$_2$/MoO$_{3-x}$ interface. Since the photocurrent flows from the Ag to ITO electrode within the cell, the MoO$_{3-x}$ nanostructure should inject holes but not electrons to TiO$_2$.

As discussed in chapter 2.3.3, nanostructured MoO$_{3-x}$ on the nanotemplate has oxygen-deficient states. Since the XPS peak area of Mo^{6+} and that of Mo^{5+} are ~75% and 25%, respectively. This indicates that oxygen deficiency value *x* is 0.25. The band

structures of MoO_3 and MoO_{3-x} are illustrated in Figure 3.7. MoO_{3-x} is reported to have an intermediate defect band (Figure 3.7b), which causes the electroconductivity and LSPR. According to literature,[11,12] an oxygen deficiency of 0.2 or higher causes a negative Fermi level shift by ~0.5 eV (just below the conduction band). In addition, thermal excitation of electrons from the intermediate defect band to the conduction band of MoO_{3-x} generates holes and electrons in the defect band and conduction band, respectively.
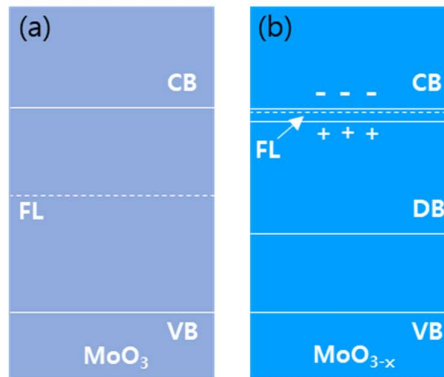
Figure 3.7 Illustration of proposed band structures of (a) MoO_3 and (b) MoO_{3-x}. CB, VB, DB, and FL are the conduction band, valence band, defect band, and Fermi level, respectively.

A band structure of the cell is proposed and schematically drawn in Figure 3.8 on the basis of literature data[13] and results mentioned above. Under NIR light, the holes may be excited as a result of LSPR and injected into the TiO_2 valence band. This excitation might be interfacial electron transition because holes (or electrons) are not mobile in the energy gap.[14-16] The holes injected into the TiO_2 valence band are accumulated in the interfacial region, and finally, spill over and diffuse to the ITO and Ag electrodes. The holes diffusing toward Ag finally recombine with the electrons in the MoO_{3-x} conduction band. The remaining electrons in the MoO_{3-x} conduction band are transported to the Ag electrode and the holes in the TiO_2 valence band diffuse to the ITO electrode and give rise to the photocurrent response. Note that the energy of a hole with a positive charge

increases as it goes down in the band diagram, and that holes are mobile in TiO_2 valence band[17,18] even though it is known as an n-type semiconductor.
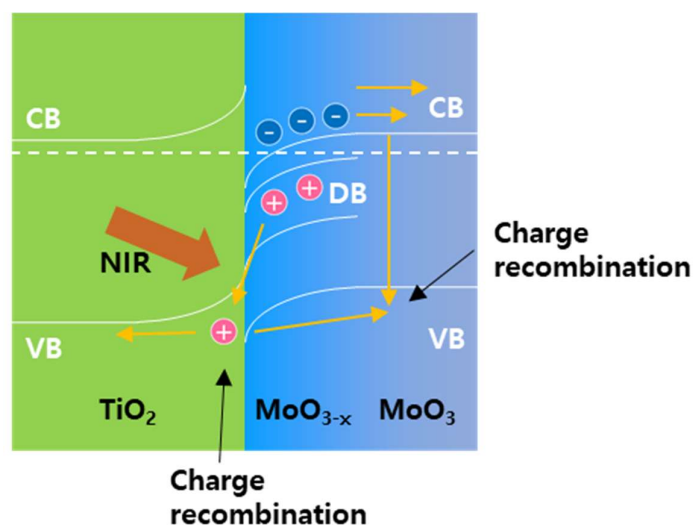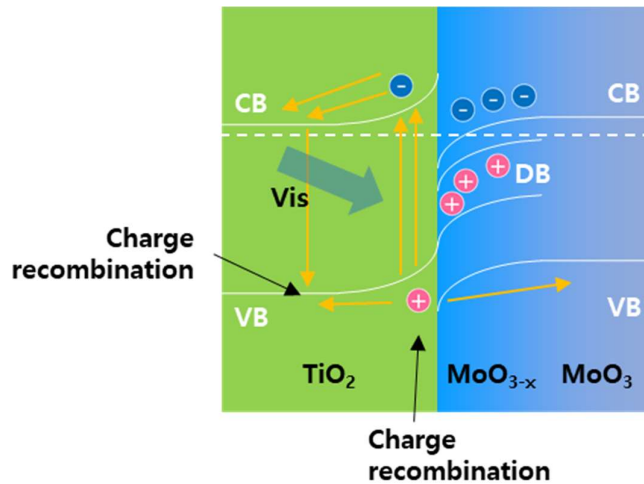

Figure 3.8 Illustration of the band structure at the TiO_2/nanostructured MoO_{3-x} interface under NIR irradiation.

Photocurrents of the $ITO|In_2O_3$ nanotemplate$|MoO_3|Ag$ cell were measured at different temperatures. As Figure 3.9 shows, the photocurrent increases by a factor of 1.4 when the cell temperature increases from 24 to 55 ℃, suggesting that the thermal excitation of electrons in MoO_{3-x} is important for the photoresponses.
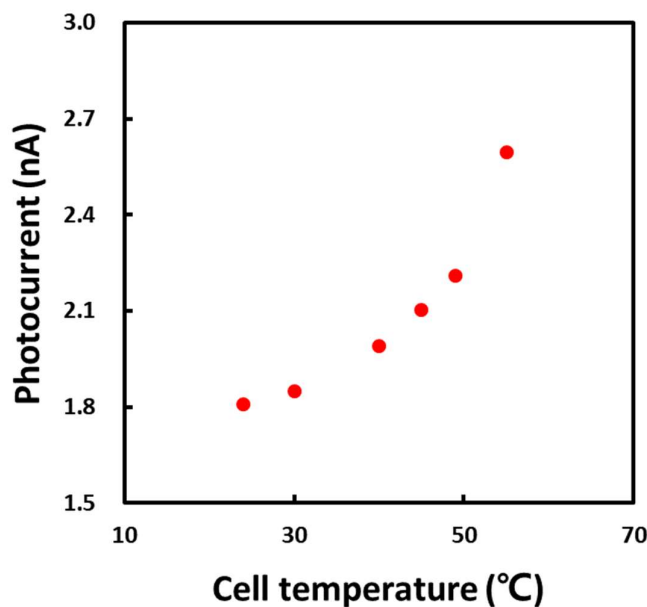
Figure 3.9 Relationship between cell temperature and photocurrent for ITO|In$_2$O$_3$ nanotemplate|MoO$_3$|Ag cell.

The opposite, negative current observed under visible light could be explained in terms of excitation of electrons in the TiO$_2$ valence band to the defect levels (*i.e.*, donor levels) below the TiO$_2$ conduction band, which are thermally excited to the conduction band and transported in turn to the ITO electrode because of the band bending in the space charge layer (Figure 3.10). The holes generated in the TiO$_2$ valence band are accumulated in the interfacial region and diffuse to both of the electrodes. The holes diffusing toward ITO finally recombine with the electrons in the TiO$_2$ conduction band. The electrons remaining in the TiO$_2$ conduction band and holes in the MoO$_3$ valence band contribute to the negative photocurrent. Since this negative current is due to the visible-light excitation of TiO$_2$, it flows both in the cell with and without the nanotemplate.

Figure 3.10 Illustration of the band structure at the TiO_2/nanostructured MoO_{3-x} interface under visible irradiation.

### 3.3.4 Narrower IPCE action spectra

The peak width of the photocurrent action spectra of the $ITO|TiO_2|In_2O_3$ nanotemplate$|MoO_3|Ag$ cells in Figure 3.5b (<300 nm) is much narrower than that of the corresponding absorption spectra (~540 nm, Figure 3.4). Since the photocurrents were proportional to the light intensity (Figure 3.11), the band narrowing was not due to a multiphoton process, which is characterized by superlinear dependence on the light intensity. At shorter wavelengths than the peak (<850 nm), the opposite process shown in Figure 3.10 occurs more frequently and cancels the hole injection from MoO_{3-x} to TiO_2 (Figure 3.8). At wavelengths longer than the peak, energy of photons (~1.4 eV) may not be sufficient for the uphill hole transfer from MoO_{3-x} to TiO_2, since the estimated energy gap between the defect band and valence band of TiO_2 is ~1.5 eV, which corresponds to ~820 nm. Therefore, the efficiency is lowered at around this wavelength. Those different effects may narrow the photocurrent peak.
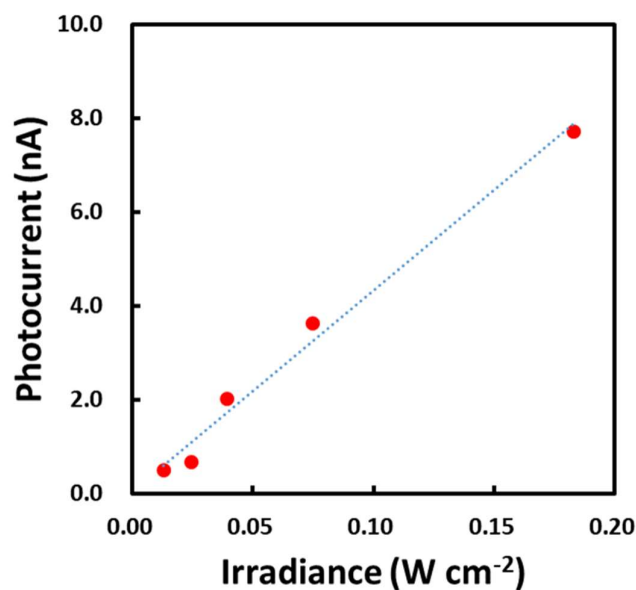
Figure 3.11 Relationship between the irradiance (900-1400 nm) and the photocurrent.

3.3.5 Improvement of photocurrent

In this chapter, the compound PICS was achieved for the first time. However, achieved photoresponse and the IPCE value of the cell is about two orders of magnitude lower than those of typical Au-TiO$_2$ photovoltaic cells. This is probably due to the charge recombination or accumulation of the proposed mechanism. One of the easiest ways to overcome the recombination, for making the responses of a photodetector larger, is applying an appropriate bias voltage, rather than measuring at zero bias (*i.e.*, short-circuit conditions). Therefore, photocurrent responses were measured at different potentials. As can be seen in Figure 3.12, under bias voltage of 0.1 V, photocurrent increased more than 2-fold. However, a better way to improve the efficiency of the PICS may be selecting materials with high carrier densities and mobilities instead of TiO$_2$. Also, combination of semiconductors must be chosen carefully on the basis of the interfacial band structure.
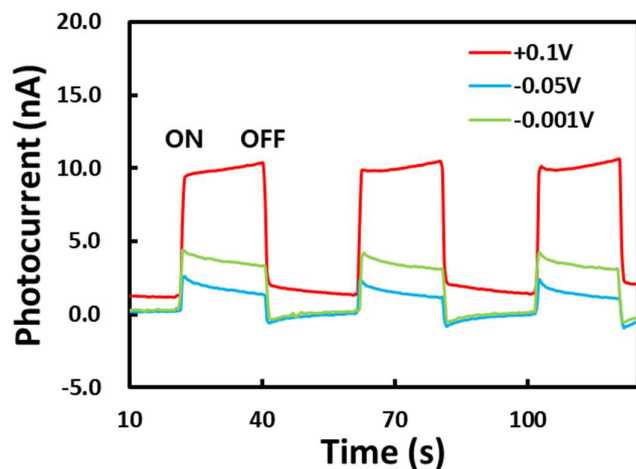
Figure 3.12 Photocurrent responses under application of bias voltage.

3.4 Conclusions

To achieve compound PICS for the first time, nanostructured MoO_{3-x} was used in this chapter, because of their organic free interface and relatively high LSPR energy (~1.4 eV). This plasmonic nanostructured MoO_{3-x} was involved in solid-state photovoltaic cells. The developed photovoltaic cells exhibited photocurrent responses under NIR irradiation (700-1400 nm). On the basis of the results obtained, it is concluded that those responses are based on PICS, and that the charge separation under NIR light occurs at the TiO_2/MoO_{3-x} interface. At the interface, the MoO_{3-x} should inject holes but not electrons to TiO_2. The mechanism of PICS was discussed in a band diagram at the TiO_2-MoO_{3-x} interface. The PICS efficiency can be improved by applying a bias voltage. The efficiency would be improved further by selecting a more appropriate semiconductor with a higher hole transport ability.

3.5 References

1   K. Yu, N. Sakai, and T. Tatsuma, *Electrochemistry*, 2008, **76**, 161–164.

2   P. Reineck, G. P. Lee, D. Brick, M. Karg, P. Mulvaney, and U. Bach, *Adv. Mater.*, 2012, **24**, 4750–4755.

3   F. P. García De Arquer, A. Mihi, D. Kufer, and G. Konstantatos, *ACS Nano*, 2013, **7**, 3581–3588.

4   Y. Takahashi and T. Tatsuma, *Appl. Phys. Lett.*, 2011, **99**, 1–4.

5   S. Mubeen, J. Lee, W. R. Lee, N. Singh, G. D. Stucky, and M. Moskovits, *ACS Nano*, 2014, **8**, 6066–6073.

6   L. Wu, G. M. Kim, H. Nishi, and T. Tatsuma, *Langmuir*, 2017, **33**, 8976–8981.

7   Y. Takahashi and T. Tatsuma, *Nanoscale*, 2010, **2**, 1494.

8   G. Garcia, R. Buonsanti, E. L. Runnerstrom, R. J. Mendelsberg, A. Llordes, A. Anders, T. J. Richardson, and D. J. Milliron, *Nano Lett.*, 2011, **11**, 4415–4420.

9   C. Julien, A. Khelfa, and O. M. Hussain, *J. Cryst. Growth,* 1995, **156**, 235–244.

10   N. W. Pu, W. S. Liu, H. M. Cheng, H. C. Hu, W. T. Hsieh, H. W. Yu, and S. C. Liang, *Materials*, 2015, **8**, 6471–6481.

11   J. W. Rabalais, R. J. Colton, and A. M. Guzman, *Chem. Phys. Lett.*, 1974, **29**, 131–133.

12   M. T. Greiner, L. Chai, M. G. Helander, W. M. Tang, and Z. H. Lu, *Adv. Funct. Mater.*, 2012, **22**, 4557–4568.

13   M. T. Greiner, M. G. Helander, W. M. Tang, Z. Bin Wang, J. Qiu, and Z. H. Lu, *Nat. Mater.*, 2012, **11**, 76–81.

14   C. Creutz, B. S. Brunschwig, and N. Sutin, *J. Phys. Chem. B*, 2006, **110**, 25181–25190.

15   C. Boerigter, U. Aslam, and S. Linic, *ACS Nano*, 2016, **10**, 6108–6115.

16   K. Wu, J. Chen, J. R. McBride, and T. Lian, *Science*, 2015, **349**, 632–635.

17   K. Kawahara, Y. Ohko, T. Tatsuma, and A. Fujishima, *Phys. Chem. Chem. Phys.*, 2003, **5**, 4764.

18   H. Haick and Y. Paz, *ChemPhysChem*, 2003, **4**, 617–620.

Chapter 4

# Infrared PICS based on electron injection from ITO NP

4.1 Introduction

In Chapter 3, compound PICS was achieved for the first time at the interface between TiO_2/MoO_{3-x} under NIR irradiation (700-1400 nm) and continuous hole injection from the nanostructured MoO_{3-x} to the valence band of TiO_2 was observed. After that, temporal PICS of plasmonic CuS NP[1] was reported and it was also based on hole injection from the NP to a semiconductor. To date, compound PICS based on electron injection has not yet been reported. Although contributions of energetic holes have recently attracted attention regarding plasmonic noble metals,[2-7] there are clear reasons to achieve electron injection from plasmonic compound nanomaterials. First, electron injection is expected to realize higher efficiency of PICS, because free electrons in most compound materials are expected to have higher mobility than holes.[8] Second, when combined with a hole injection, the combined systems would give excellent solutions to overcome the low energy limitations of infrared photons.[9]

In order to achieve the electron injection in compound PICS, it is important to select an electron-accepting semiconductor with an appropriate conduction band level and an electron donor with a suitable potential (Figure 4.1).[10] The energy gap between the Fermi level of the NP and the conduction band level of the semiconductor (ΔE_b) should be smaller than the resonance photon energy of the plasmonic NPs used (ΔE_{LSPR}). Conversely, if the gap is too close then the output voltage would be small. So, it is important to find a combination of materials with the appropriate energy level. In addition, the potential of the electron donor (E_d) should be more negative than that of the compound Fermi level (E_{FL}). In the case of plasmonic compound materials, they exhibit LSPR mostly in the NIR region. The corresponding resonance photon energy is too small that selection of the semiconductor and a donor is more tight in comparison with the conventional systems with noble metal NPs, the resonant wavelength of which is mostly in the visible region.
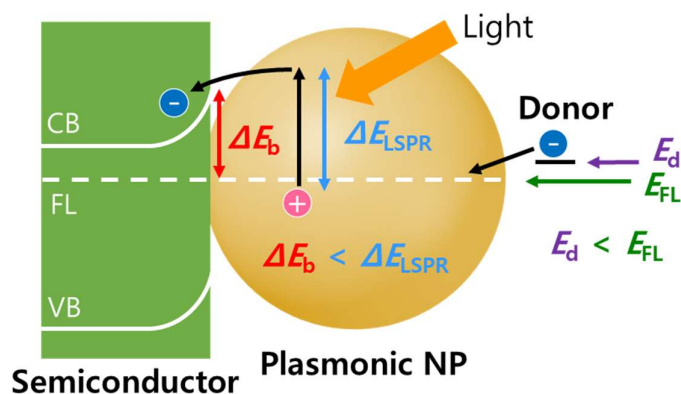
Figure 4.1 Mechanism and key requirements of conventional PICS.

To achieve electron injection of compound PICS, ITO NPs synthesized in 2.3.1 was employed. ITO is well known as one of the compound materials with the highest free charge carrier density ($\sim 10^{21}$ cm^{-3}).[11] In addition, ITO NPs exhibit tunable LSPR in the NIR region (1600−2200 nm)[12] as illustrated in Figure 4.2a. It is assumed that the failure to observe PICS with ITO NPs was due to long ligand protecting layer, which blocks electron injection from the ITO NPs to a semiconductor. As a solution to this issue, ITO NPs with a shorter ligand was synthesized in Chapter 2. As a semiconductor material for the PICS system, TiO$_2$ was coupled with the ITO NPs. It can be expected that the energy gap between them will be >0.6 eV because the work function of ITO is 4.83–5.2 eV[13] and the electron affinity of anatase TiO$_2$ is 3.78–4.21 eV[14,15] (Figure 4.2b). A solid-state cell system which could omit the electron donor[16] was adopted in this chapter for focusing on the electron-accepting semiconductor.
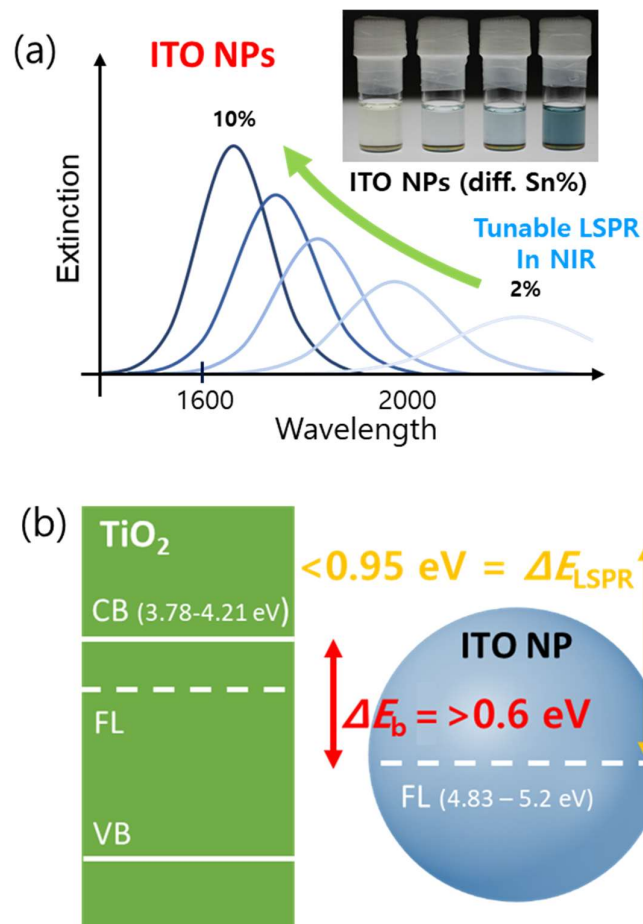
Figure 4.2 (a) Illustration of tunable LSPR of ITO NPs in NIR region and a photograph of the NPs dispersed in toluene (inset). (b) Band structure of anatase TiO$_2$ and ITO NP.

In this chapter, solid-state ITO|TiO$_2$|ITO NP|Ag cells were developed. Those cells exhibited photoresponses in the 1500−2200 nm range, whereas the conventional PICS cells with plasmonic metal NPs have exhibited photoresponses at 1700 nm or shorter wavelengths.[17] Thus, the first PICS based on electron injection form compound NPs to a semiconductor was achieved and the longest wavelength of 2200 nm was attained for PICS.

4.2 Experimental

4.2.1 Fabrication of solid-state cells

An ITO film coated on a glass plate (23 x 23 mm) was patterned into an electrode (6 x 23 mm) by an infrared laser (1064 nm) (Figure 4.1a). The patterned ITO electrode was sonicated in acetone, Milli-Q water, and 2-propanol. The cleaned ITO substrate was coated with a ~60-nm-thick TiO_2 layer (17 x 23 mm) by a spray pyrolysis method[18] through a glass mask (Figure 4.1b). The ITO NPs (10, 9, 5, and 2.5 mol% Sn) was coated on the substrate by spin-coating (2000 rpm for 30 s) from a 0.20-0.85 wt% NP suspension. After that, NPs were removed by ethanol-soaked cotton buds from the edge regions of the substrate (~3 mm) (Figure 4.3c), followed by drying in a vacuum chamber for 12 h. The prepared sample was moved to an evaporation chamber with a patterned mask for the back electrode (Figure 4.3d) and Ag was evaporated (~70 nm thick) at the rate of 0.3 nm s^{-1}. Each prepared substrate has 4 photovoltaic cells with the cell size of ~2 x 2 mm (Figure 4.3e).
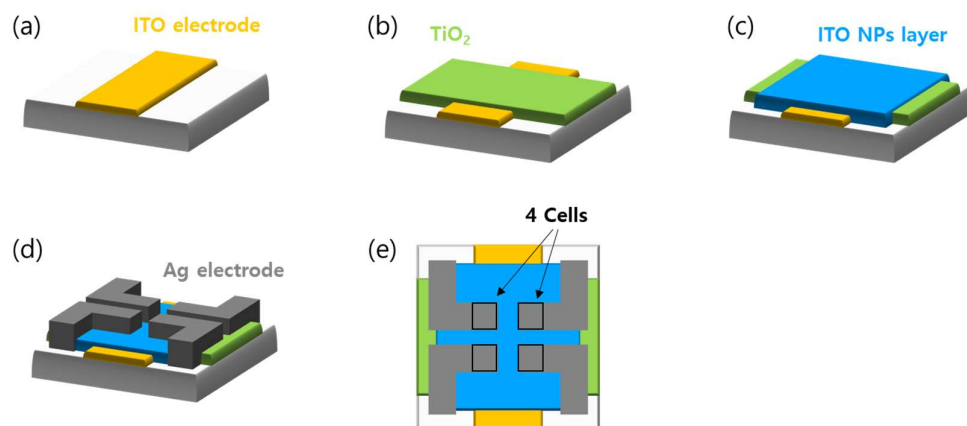
Figure 4.3 (a) Patterned ITO-film coated glass. (b) TiO_2 layer prepared on ITO electrode. (c) NP layer spin-coated on TiO_2 followed by edge removal. (d) Ag evaporated through a patterned mask. (e) 4 solid-sate cells on one substrate.

4.2.2 Characterization

The structure of photovoltaic cells was investigated by scanning electron microscopy (SEM) using a JSM-7500FA (JEOL). Optical spectra were measured using a

Jasco V-670 UV-vis-NIR spectrophotometer. Short-circuit photocurrent measurements were carried out with a potentiostat (SI 1285A, Solartron) under NIR light irradiation (1400–2200 nm, full width at half maximum ~250 nm, 4.0 x 10^{16} photons cm^{-2} s^{-1}) from the ITO electrode side.

4.3 Results & discussion

4.3.1 Preparation of ITO NP layers

To develop ITO|TiO_2|ITO NPs|Ag structure cells, it is necessary to fabricate a compact ITO NP layer on a TiO_2 layer to prevent short-circuiting between TiO_2 and the Ag electrode. To prepare the compact layer, the concentration of ITO NP was increased from 0.20 wt% (used for a nanotemplate in Chapter 3, coverage ~57%) to 0.51 and 0.85 wt%. When the concentration of the suspension increased from 0.20 to 0.51 wt%, it was found that ITO NP covered almost 100% of the substrate surface (Figure 4.4a). Extinction spectra were measured with samples prepared from the suspensions of 0.20, 0.51, and 0.85 wt%. As can be seen in Figure 4.4b, the extinction peak height of the ITO NP layer is roughly proportional to the NP concentration. From those results, it is concluded that the ITO NP suspension with a concentration of 0.51 wt% or higher is sufficient to prevent a short circuit between TiO_2 and the Ag electrode. Without a doubt, a higher photoresponse can be expected from a layer having a high light absorption. Thus, solid-sate photovoltaic cell was prepared using the 0.85 wt% suspension.
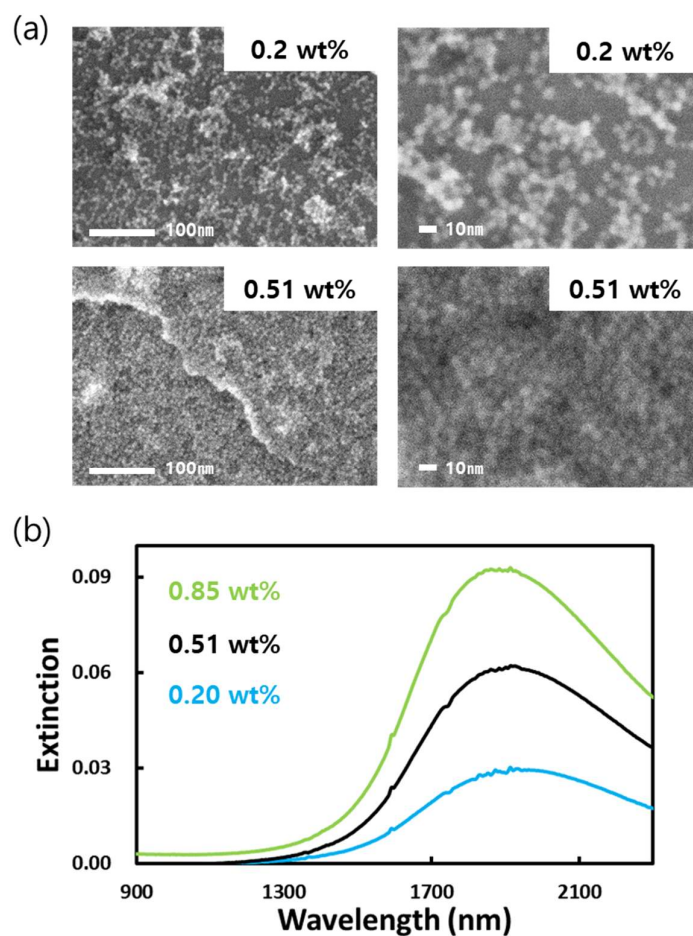
Figure 4.4 (a) SEM images of the prepared ITO NP layers (using 0.20 and 0.51 wt% suspension). (b) Extinction spectra of the ITO NP layers prepared by using different concentrations of ITO NP suspensions.

4.3.2 Photoresponses of the photovoltaic cells

The cell structure of the solid-state ITO|TiO$_2$|ITO NPs|Ag cells is illustrated in Figure 4.5a. Besides those cells, a cell without the ITO NP layer (ITO|TiO$_2$|Ag cell) and that with WO$_3$ instead of TiO$_2$ (ITO|WO$_3$|ITO NPs|Ag cell) were prepared for comparison with the ITO|TiO$_2$|ITO NPs|Ag cells. WO$_3$ (30 nm-thick) was prepared by a vapor deposition method on the ITO electrode.
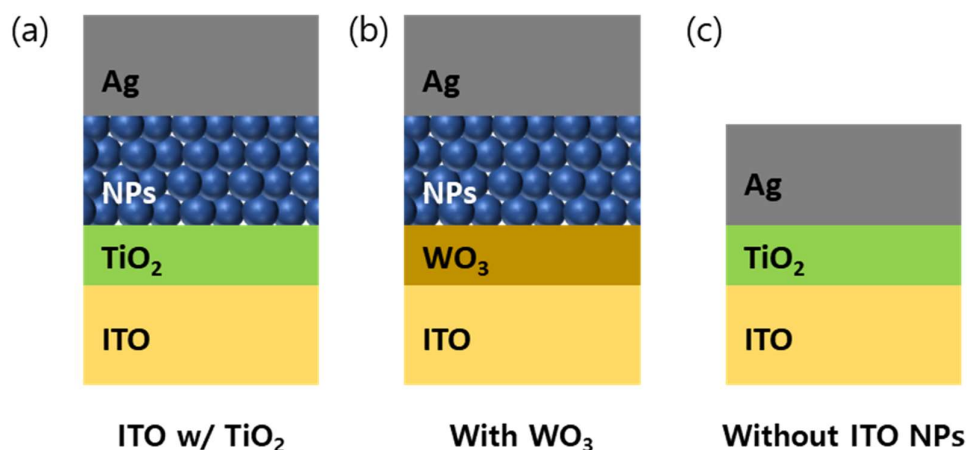
Figure 4.5 Illustration of the structures of the prepared cells including comparison groups; (a) ITO|TiO$_2$|ITO NPs|Ag cell, (b) cell with WO$_3$ in place of TiO$_2$ (*i.e.*, ITO|WO$_3$|ITO NPs|Ag), and cell without ITO NPs (*i.e.* ITO|TiO$_2$|Ag).

All the cells were subjected to open-circuit photovoltage measurements under the irradiation with monochromatic NIR light (1400−2200 nm) from the ITO electrode side. The photovoltage action spectra of the prepared cells are shown in Figure 4.6a. From the two comparison groups (the cell without the ITO NP layer and the cell with WO$_3$), no significant photovoltage responses were observed. In case of the cell without the ITO NP layer, it does not have a light absorption layer so that it cannot show photovoltage response. In case of the cell with WO$_3$, the conduction band level of WO$_3$ is sufficiently positive[14] to form an ohmic contact with ITO (Figure 4.6b) so that charge separation cannot occur. In contrast, much larger photovoltage responses were observed for the cell with TiO$_2$ and ITO NPs. In addition, the photovoltage action spectrum was well matched with the extinction spectrum of the ITO NP layer on the TiO$_2$ film. Those results indicate that the Schottky contact between TiO$_2$ and the ITO NP layer and plasmonic light absorption of ITO NPs are essential for the photovoltage responses.
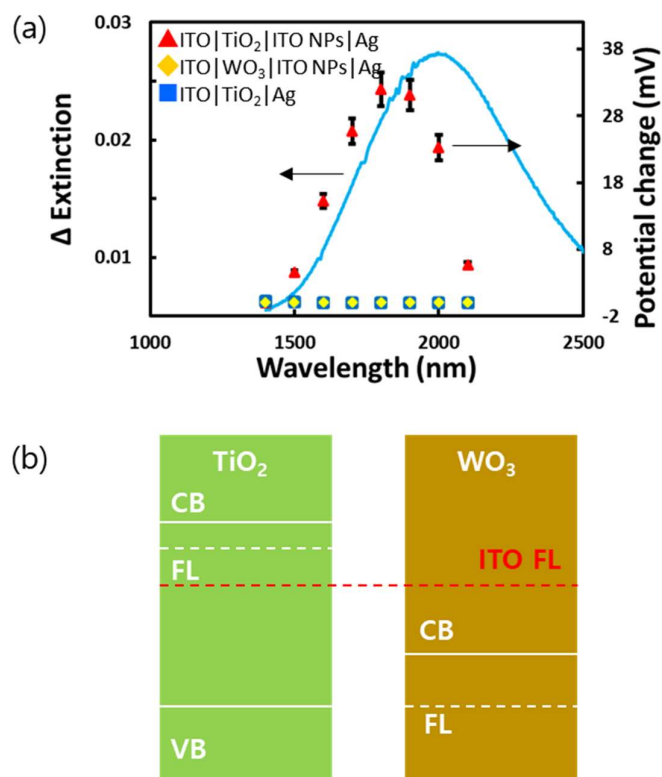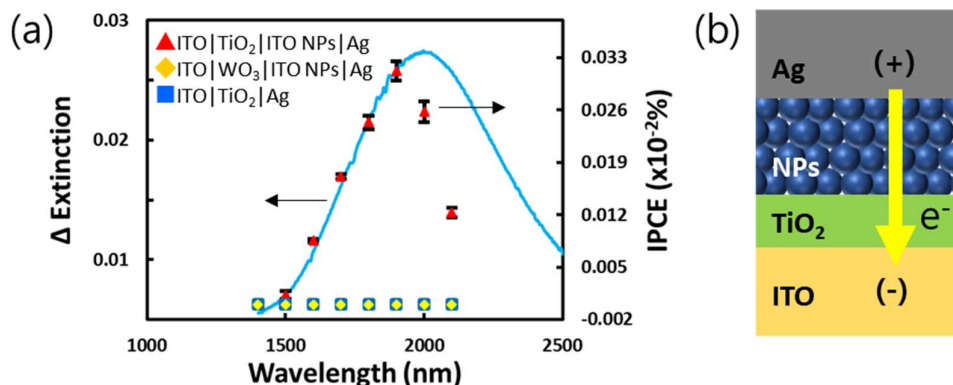
Figure 4.6 (a) Open-circuit photovoltage action spectra of the ITO|TiO$_2$|ITO NPs|Ag cell (red triangle), ITO|TiO$_2$|Ag cell (yellow rhombus), and ITO|WO$_3$|ITO NPs|Ag cell (blue square) together with extinction spectrum of the ITO NP layer (blue curve). (b) Band levels of TiO$_2$ and WO$_3$ and the Fermi level of ITO.

Short-circuit photocurrent responses were also measured under the same irradiation conditions for the 3 different cells. Figure 4.7a shows the IPCE action spectra thus obtained together with the extinction spectrum of the ITO NP layer. Consistent with photovoltage response, the two comparison groups showed no significant photocurrent responses, whereas the cell with TiO$_2$ and ITO NPs showed much larger photocurrents. The direction of photocurrents and the IPCE action spectrum matched well with the extinction spectrum indicated that the electron should be injected from the plasmon-resonant ITO NPs to TiO$_2$ (Figure 4.7b). In both photovoltage and photocurrent action spectra, the ITO|TiO$_2$|ITO NPs|Ag cell showed relatively steeper curve in the longer wavelength region of the peak in comparison with the extinction spectrum. It is highly likely that the energy

of the electrons in the long wavelength region of the peak is not high enough to leap over the Schottky barrier. The solid-state cell has another ITO layer under the TiO_2 as a front electrode. However, since the ITO electrode is not composed of small NPs, the electrons are not localized and LSPR is not observed. Therefore, PICS cannot be expected at the interface between the ITO electrode and TiO_2. From the results above, it is concluded that PICS was achieved at the TiO_2-ITO NP interface on the basis of electron injection from ITO NP to TiO_2 under NIR irradiation.

Figure 4.7 (a) Short-circuit photocurrent (as IPCE) action spectra of the ITO|TiO_2|ITO NPs|Ag cell (red triangle), ITO|TiO_2|A cell (yellow rhombus), and ITO|WO_3|ITO NPs|Ag cell (blue square) together with extinction spectrum of the ITO NP layer (blue curve). (b) Electron flow direction within the ITO|TiO_2|ITO NPs|Ag cell under NIR irradiation.

4.3.3 Optimization of the photovoltaic cell

The compound PICS based on the electron injection was achieved by using ITO|TiO_2|ITO NPs|Ag cell. Although it can use low energy photons in the long wavelength region, the cell shows only $0.3 \times 10^{-3}\%$ IPCE at 1900 nm. To improve and optimize the IPCE value of the cell, correlation between the thickness of the ITO NP layer and the peak IPCE value was examined. PICS cells were prepared by using different concentrations of the ITO NP suspensions as shown in Figure 4.8.
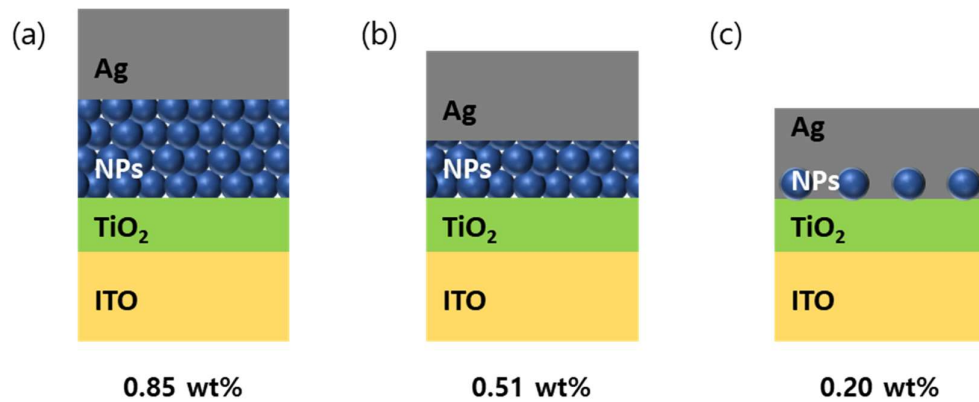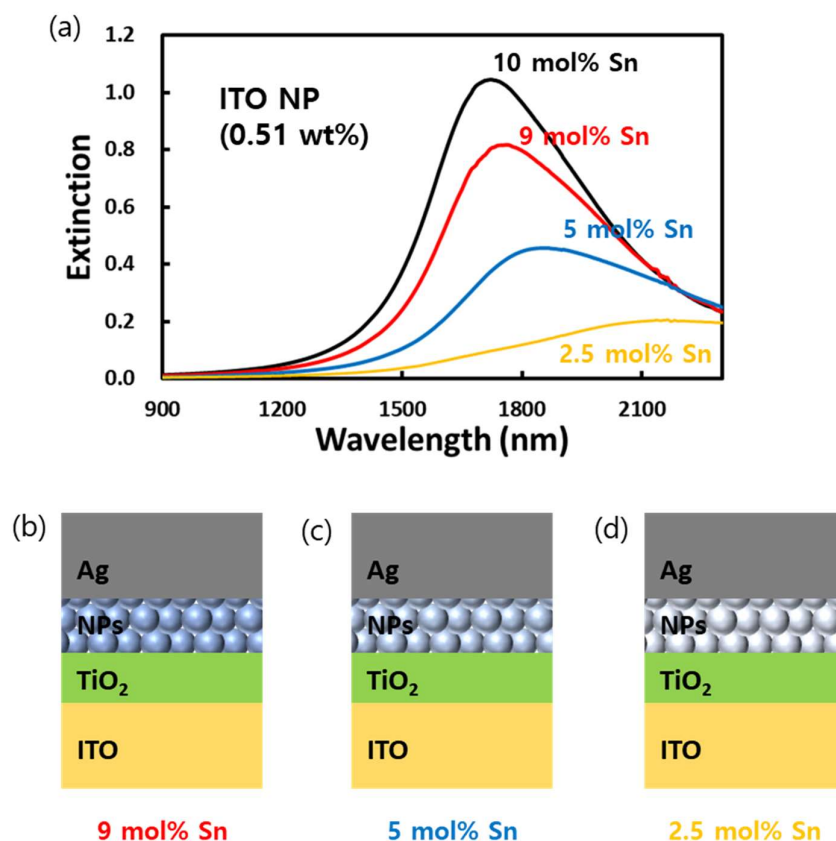
Figure 4.8 Illustration of the cells with a different thickness of ITO NP layer prepared form 0.20-0.85 wt% ITO NP suspensions.

When decreasing the concentration from 0.85 to 0.51 wt%, the peak IPCE value was increased more than threefold (Figure 4.9), despite the fact that the extinction of the layer decreased by about 33%. This might reflect that surplus ITO NPs act as a resistor and/or charge recombination center. Actually, the IPCE value of the cell with the nanostructured MoO_{3-x} described in 3.3.2 also depends on the conductivity of the nanotemplate consisting of ITO NPs. However, if the NP concentration was reduced further to 0.20 wt%, the probability of short-circuiting between the Ag electrode and the TiO_2 layer was increased, likely because the surface coverage drops below 100%.
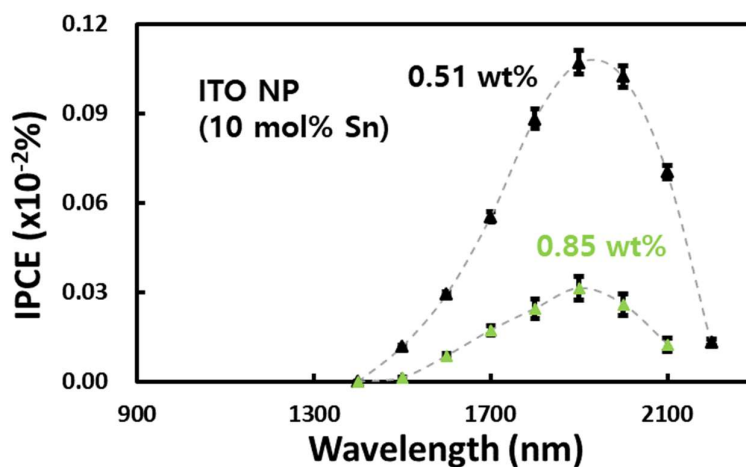
Figure 4.9 IPCE action spectra of ITO|TiO$_2$|ITO NPs|Ag cells with ITO NP layers prepared form 0.51 and 0.85 wt% ITO NP suspensions (10 mol% Sn).

As described in 2.3.1, absorption characteristics of the ITO NP layer also can be controlled by adjusting the Sn doping ratio of the ITO NPs. Using ITO NPs with a fixed size and different Sn doping ratios (9, 5, and 2.5 mol%), ITO|TiO$_2$|ITO NPs|Ag cells were prepared by using 0.51 wt% ITO NP suspension (Figure 4.10b, c, and d). As the doping ratio of ITO NPs was reduced, the LSPR peak was red-shifted and lowered (Figure 4.10a). As discussed in chapter 2.3.1, this is because the free electron density was decreased as the doping ratio was reduced.

Figure 4.10 (a) Extinction spectra of ITO|TiO$_2$|ITO NPs|Ag cells with ITO NPs of different Sn doping ratios. (b), (c), and (d) Illustration of the cells with highly, moderately, and lightly doped ITO NPs, respectively.

Although all the cells were subjected to short-circuit photocurrent measurements, only the cells with 9%- and 10%-doped ITO NPs exhibited significant responses. The peak of IPCE action spectra was red-shifted and lowered with decreasing doping ratio (Figure 4.11) similarly to the extinction peak. It is known that the potential of ITO Fermi level shifts positively as the Sn doping ratio decreases.[19] The shift is about 0.4 eV for the decrease of the ratio from 10% to 0%.[20] In addition, as discussed above, expected energy gap between the conduction band of TiO$_2$ and the Fermi level of ITO is >0.6 eV. On the basis of those values, the Schottky barrier height at the interface between lightly doped ITO NPs and TiO$_2$ could be >1.0 eV. Therefore, the suppressed photocurrents of the cells

with lightly doped (5 or 2.5 mol% Sn) ITO NPs are explained in terms of the raised energy barrier at the TiO_2-ITO interface, which blocks the uphill electron injection from ITO NPs to TiO_2.
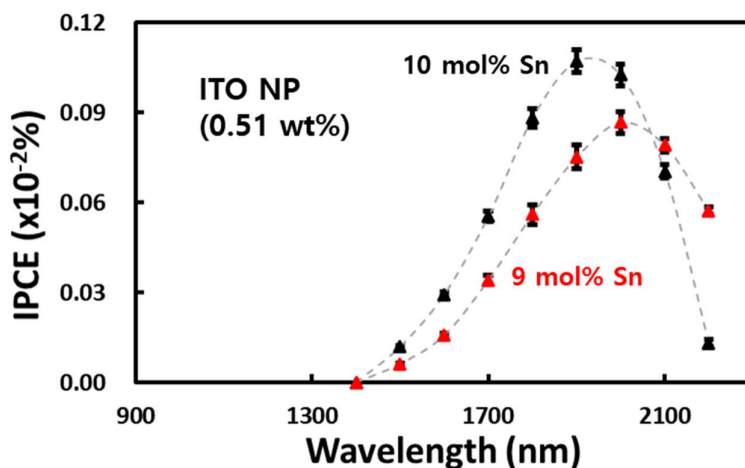
Figure 4.11 IPCE action spectra of ITO|TiO_2|ITO NPs|Ag cells containing ITO NPs with different Sn doping ratios (0.51 wt% NP suspension was used).

As described above, the surplus ITO NPs could have negative effects on the IPCE value, whereas the ITO NP layer prepared from a 0.20 wt% ITO NP suspension results in short-circuiting between the Ag electrode and TiO_2. Therefore, to prevent the cell from short-circuiting, a MoO_3 layer was introduced as a hole transporting layer (HTL)[21] by a thermal vapor deposition method between the ITO NP layer and the Ag electrode (Figure 4.12a). The prepared ITO|TiO_2|ITO NPs|MoO_3|Ag cell was subjected to photocurrent measurements. The introduction of HTL to the cell with the ITO NP layer prepared by using 0.20 wt% suspension resulted in observable photocurrents. The IPCE action spectrum of the cell is shown in Figure 4.12b. The cell shows ~0.146 x 10^{-2}% of IPCE value at 1900 nm even the ITO NP layer has lost ~50% of extinction compared with the ITO NP layer prepared from the 0.51 wt% suspension.
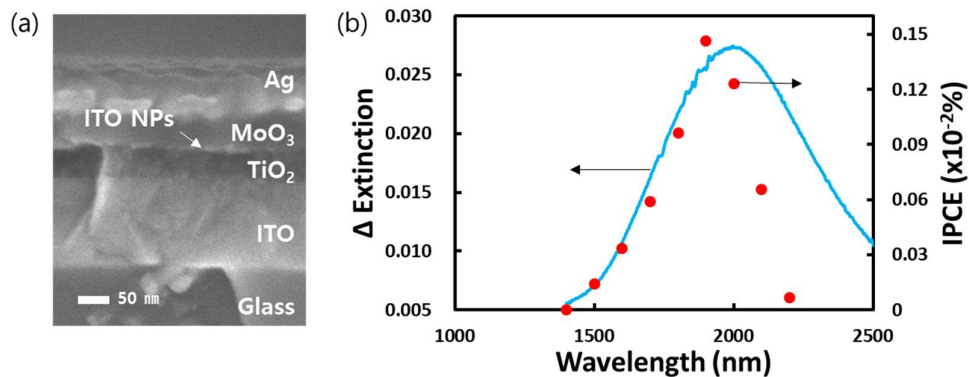
Figure 4.12 (a) Cross-sectional SEM image and (b) IPCE action spectrum of the ITO|TiO$_2$|ITO NPs|MoO$_3$|Ag cell (0.20 wt% ITO NP (10 mol% Sn) suspension).

4.3.4 Mechanism of the photovoltaic behavior

On the basis of the results mentioned above, it can be concluded that the charge separation occurs at the interface between the ITO NPs and TiO$_2$ and that the ITO NPs inject electrons continuously into the conduction band of TiO$_2$. The most plausible mechanism of PICS is illustrated in Figure 4.13, including lightly doped ITO NPs. Under NIR irradiation, the electrons are excited by plasmon resonance of ITO NPs. The excited electrons leap over the Schottky barrier and injected into the conduction band of TiO$_2$. If the doping ratio is decreased, the Fermi level[20] is lowered and the Schottky barrier height is raised. In addition, lightly doped ITO NPs tend to absorb photons of lower energy (*i.e.*, light of longer wavelengths). Therefore, heavily doped ITO NPs are advantageous for PICS based on electron injection.
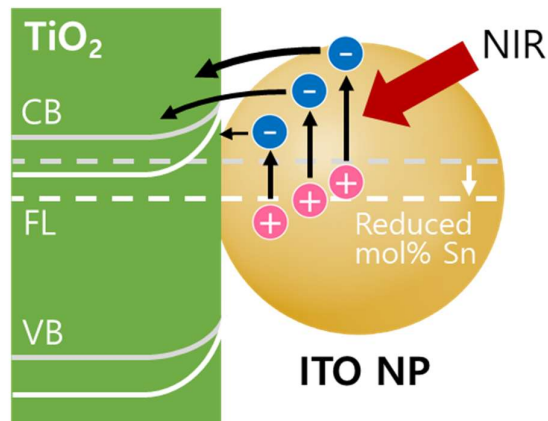
Figure 4.13 Illustration of the possible mechanism of PICS at the interface between TiO_2 and ITO NPs.

4.4 Conclusions

To achieve compound PICS based on electron injection, ITO NPs with a short ligand developed in Chapter 2 were coupled with TiO_2. The prepared ITO|TiO_2|ITO NPs|Ag cells exhibited current and voltage responses to NIR light in the 1500−2200 nm region. Those responses are based on compound PICS that involves the electron injection from the ITO NPs to TiO_2. To improve the IPCE value, the cells were optimized by increasing the Sn doping ratio of the ITO NPs, decreasing the NP layer thickness, and introducing the MoO_3 HTL. As a result of the optimization, the ITO|TiO_2|ITO NPs|MoO_3|Ag cell exhibited 0.146 x 10^{-2}% IPCE at 1900 nm. This device would be applied to PICS-based NIR devices including NIR photodetectors. Through this chapter, compound PICS based on electron injection was achieved for the first time. In addition, the longest wavelength of 2200 nm was attained for PICS.

4.5 References

1   Z. Lian, M. Sakamoto, H. Matsunaga, J. J. M. Vequizo, A. Yamakata, M. Haruta, H. Kurata, W. Ota, T. Sato, and T. Teranishi, *Nat. Commun.*, 2018, **9**, 2314.

2   S. Mubeen, J. Lee, W. R. Lee, N. Singh, G. D. Stucky, and M. Moskovits, *ACS Nano*, 2014, **8**, 6066–6073.

3   G. Liu, P. Li, G. Zhao, X. Wang, J. Kong, H. Liu, H. Zhang, K. Chang, X. Meng, T. Kako, and J. Ye, *J. Am. Chem. Soc.*, 2016, **138**, 9128–9136.

4   K. Saito, I. Tanabe, and T. Tatsuma, *J. Phys. Chem. Lett.*, 2016, **7**, 4363–4368.

5   H. Nishi, M. Sakamoto, and T. Tatsuma, *Chem. Commun.*, 2018, **54**, 11741–11744.

6   G. V. Naik, A. J. Welch, J. A. Briggs, M. L. Solomon, and J. A. Dionne, *Nano Lett.*, 2017, **17**, 4583–4587.

7   K. Saito, and T. Tatsuma, *Nano Lett.*, 2018, **18**, 3209–3212.

8   C. Jacoboni, C. Canali, G. Otiaviani, and A. A. Quaranta, *Solid State Electron.*, 1977, **20**, 77–89

9   Y. Zhang, C. Yam, and G. C. Schatz, *J. Phys. Chem. Lett.*, 2016, **7**, 1852–1858.

10   T. Tatsuma, H. Nishi, and T. Ishida, *Chem. Sci.*, 2017, **8**, 3325–3337.

11   X. Liu and M. T. Swihart, *Chem. Soc. Rev.*, 2014, **43**, 3908–3920.

12   M. Kanehara, H. Koike, T. Yoshinaga, and T. Teranishi, *J. Am. Chem. Soc.*, 2009, **131**, 17736–17737.

13   Y. Gassenbauer, R. Schafranek, A. Klein, S. Zafeiratos, M. Hävecker, A. Knop-Gericke, and R. Schlögl, *Phys. Rev. B*, 2006, **73**, 1–11.

14   Y. Xu and M. A. A. Schoonen, *Am. Mineral.*, 2000, **85**, 543–556.

15   G. Liu, W. Jaegermann, J. He, V. Sundström, and L. Sun, *J. Phys. Chem. B*, 2002, **106**, 5814–5819.

16   Y. Takahashi and T. Tatsuma, *Appl. Phys. Lett.*, 2011, **99**, 1–4.

17   M. W. Knight, H. Sobhani, P. Nordlander, and N. J. Halas, *Science*, 2011, **332**, 702–705.

18   Y. Takahashi and T. Tatsuma, *Nanoscale*, 2010, **2**, 1494.

19   R. L. Z. Hoye, K. P. Musselman, and J. L. MacManus-Driscoll, *APL Mater.*, 2013, **1**, 060701.

20   P. K. Biswas, A. De, L. K. Dua, and L. Chkoda, *Appl. Surf. Sci.*, 2006, **253**, 1953–1959.

21   J. Meyer, S. Hamwi, M. Kröger, W. Kowalsky, T. Riedl, and A. Kahn, *Adv. Mater.*, 2012, **24**, 5408–5427.

Chapter 5

Conclusions

Localized surface plasmon resonance (LSPR) is a collective oscillation in a nanomaterial in resonance with an incident light. The light energy trapped by plasmonic materials such as noble metal nanoparticles (NPs) and electroconductive compound NPs can be converted into a rectified electron flow on the basis of plasmon-induced charge separation (PICS) at the interface between the plasmonic material and a semiconductor. Although plasmonic compounds have advantages such as resonance with near infrared (NIR) light, tunable LSPR, and lower cost than the noble metals, the most of investigations regarding LSPR including PICS have been based on noble metal NPs. Thus, the present work is aimed at achievement of PICS based on both electron injection and hole injection.

In Chapter 1, basics and applications of LSPR for metal NPs, LSPR characteristics of compound NPs, and their synthesis methods are summarized. Several issues in synthesis are pointed out, including thick capping agents covering the NPs and difficulty in control of doping. The principle and mechanisms of PICS with metal NPs are described, and key factors for achieving PICS by using compound NPs are discussed. On the basis of those discussion, the aims of the present work, including addressing those issues in compound NP synthesis and achieving compound PICS, are explained.

In Chapter 2, plasmonic compound nanomaterials were synthesized and tuned in terms of their LSPR properties. MoO_2, MoO_{3-x}, and ITO were chosen as target materials, since those compounds have been known to exhibit LSPR in the visible (MoO_2) to NIR (MoO_{3-x} and ITO) regions. In addition, minimizing the organic capping layer has been considered in designing those nanomaterials. First, plasmonic ITO NPs were synthesized with controlled size, regulated Sn doping ratio, and minimized ligand length by a reverse hot injection method. The synthesized ITO NPs exhibit LSPR at different wavelengths and peak width in 1600-2500 nm range depending on the doping ratio and the ligand combination of precursors used. Next, molybdenum oxide NPs were synthesized with different oxygen compositions in non-aqueous media for the first time. The synthesized MoO_2 and MoO_{3-x} NPs exhibited LSPR peaks at ~500 nm and 600-1000 nm, respectively. Their LSPR properties were tunable with several experimental parameters such as the

chain length of capping molecules and the composition of the non-aqueous medium. It was also confirmed that the MoO_2 NPs were oxidized to non-plasmonic MoO_3 NPs by annealing in an oxidizing atmosphere and that further annealing in vacuum led to reduction of the NPs to plasmonic MoO_{3-x} NPs. In addition, plasmonic nanostructures of MoO_{3-x} were prepared by thermal vapor deposition of MoO_3 onto NP ensembles as templates. The nanostructured MoO_{3-x} has an organic-free interface with the substrate and exhibits LSPR in the NIR range (peak at ~850 nm). The NP ensembles give the deposited layer a large surface area and structural distortion, which lead to dissipation of some oxygen and generation of oxygen defects, resulting in the formation of a plasmonic MoO_{3-x} nanostructure.

In Chapter 3, compound PICS based on hole injection was achieved for the first time. The nanostructured MoO_{3-x} developed in Chapter 2 was employed as a plasmonic material because of its relatively high LSPR energy (~1.4 eV, ~850 nm) and the ligand-free interface with a semiconductor. The MoO_{3-x} nanostructure was prepared on a TiO_2-coated ITO electrode using a NP ensemble as a template, followed by coating of a Ag electrode. The solid-state cells thus obtained were subjected to short-circuit photocurrent measurements under NIR light irradiation. All those cells exhibited photocurrent flows within the cell from the Ag electrode to the ITO electrode and the photocurrent action spectra that match plasmonic extinction spectra. These results indicate that the photocurrent responses originated from plasmonic MoO_{3-x}. The mechanism of the photocurrents was investigated by using the cell without the NP ensemble and that without TiO_2. It was concluded that the charge separation under NIR light occurs at the TiO_2/MoO_{3-x} interface, on the basis of hole injection from MoO_{3-x} to TiO_2.

In Chapter 4, compound PICS based on electron injection was achieved for the first time. In order to achieve electron injection from plasmonic compound NPs, plasmonic ITO NPs with a short ligand, which were synthesized in Chapter 2, were employed. Those NPs were coupled with TiO_2, so that the energy gap of about 0.6 eV (corresponding to 2000 nm wavelength), which is lower than the LSPR energy of most ITO NPs, was expected. Also, a

solid-state cell system without an electron donor (or hole transport layer) was adopted, so that only the electron-accepting semiconductor was focused. The photoresponses of the cells were investigated under NIR light irradiation (1400−2200 nm). A solid-state cell with 10 Sn% ITO NPs exhibited photovoltage and photocurrent responses in 1500−2200 nm range and the shape of the photovoltage and current action spectra well matched the extinction spectrum of the ITO NP layer. Those results and the current direction within the cell from the ITO electrode to the Ag electrode indicate that the observed photoresponses are due to PICS based on electron injection from the ITO NPs to TiO_2. Furthermore, the cell was optimized in terms of the efficiency by controlling the thickness and doping ratio of the ITO NP layer, and introducing a hole transporting layer. The photocurrent edge wavelength of 2200 nm is longer than those of the conventional PICS cells (≤1700 nm).

Compound PICS, which has been achieved in this study, has a potential to be applied to various IR materials and devices. In particular, combination of the electron injection PICS with hole injection PICS would give voltage upconversion, so that it would allow new photocatalysts that drive redox reactions of relatively high voltage by low energy IR light. Photon up-conversion from IR light to visible light might also be a potential application. Since LSPR of some compound NPs can be switched on and off by redox reactions, the compound NPs synthesized in this study would be applied to infrared smart windows for energy saving. Furthermore, compound PICS would be extended to the visible region by using prepared compound NPs such as MoO_2. Therefore, it is expected that compound PICS will realize less expensive plasmonics, effective use of solar light, and new plasmonic applications.

Publications

Papers

1. <u>Seung Hyuk Lee</u>, Hiroyasu Nishi, and Tetsu Tatsuma,

   "Tunable Plasmon Resonance of Molybdenum Oxide Nanoparticles Synthesized in Non-aqueous Media"

   Chemical Communications, 2017, **53**, 12680-12683. (Chapter 2)

2. <u>Seung Hyuk Lee</u>, Hiroyasu Nishi, and Tetsu Tatsuma,

   "Plasmonic Behaviour and Plasmon-Induced Charge Separation of Nanostructured MoO_{3-x} under Near Infrared Irradiation"

   Nanoscale, 2018, **10**, 2841-2847. (Chapter 2, 3)

3. <u>Seung Hyuk Lee</u>, Hiroyasu Nishi, and Tetsu Tatsuma,

   "Plasmon-Induced Charge Separation at the Interface between ITO Nanoparticles and TiO_2 under Near-Infrared Irradiation"

   Submitted. (Chapter 2, 4)

Conferences

1. <u>Seung Hyuk Lee</u>, Hiroyasu Nishi, and Tetsu Tatsuma,

   "Solid-State Infrared PICS Photovoltaic Cells with ITO Nanoparticles"

   The 3rd International Workshop on Advanced Nanoscience and Nanomaterials 2018, Fukuoka, Japan, Oct. 2018.

2. <u>Seung Hyuk Lee</u>, Hiroyasu Nishi, and Tetsu Tatsuma,

   " Plasmon-Induced Charge Separation at the Interface between ITO Nanoparticle and TiO_2 under Near-Infrared Irradiation"

   Fall Meeting of The Electrical Society of Japan 2018, Kanazawa, Japan, Sep. 2018.

3. <u>Seung Hyuk Lee</u>, Hiroyasu Nishi, and Tetsu Tatsuma,

   "Synthesis and infrared applications of plasmonic compound nanoparticles"

   Annual Meeting on Photochemistry 2017, Sendai, Japan, Sep. 2017.

Dec. 2018

Seung Hyuk Lee